





Aus dem Institut für Mathematik  
der Universität zu Lübeck

Direktor:

Prof. Dr. Jürgen Prestin

# Multiple-Material Variational Image Registration

Inauguraldissertation

zur

Erlangung der Doktorwürde

der Universität zu Lübeck

- Aus der Technisch-Naturwissenschaftlichen Fakultät -

Vorgelegt von

Dipl.-Math. Sven Kabus

aus Schleswig

Lübeck im Oktober 2006

Erstberichterstatter: Prof. Dr. Bernd Fischer (Universität zu Lübeck)  
Zweitberichterstatter: Prof. Dr. Heinz Handels  
(Universitätsklinikum Hamburg-Eppendorf)

Tag der mündlichen Prüfung: 26. Januar 2007

*Erst wenn der Bogenschütze schießt ohne an den Erfolg zu denken,  
kann er seine ganze Kunst entfalten.*

Tranxu



---

# Zusammenfassung

---

Die Bildregistrierung stellt eine der Hauptaufgaben innerhalb der Bildverarbeitung dar, die das tägliche Leben in vielerlei Hinsicht beeinflusst. Dies betrifft so unterschiedliche Bereiche wie die Automobilindustrie (z.B. Fahrer-Assistenz-Systeme), die Fertigungskontrolle (z.B. Displays, Dichtungen oder CDs) oder die Medizin.

Innerhalb der medizinischen Bildverarbeitung bezieht sich ein wesentlicher Anteil der Forschung auf Bildregistrierung, wie die in den vergangenen zwei Jahrzehnten stetig zunehmende Anzahl von Veröffentlichungen zeigt (PLUIM & FITZPATRICK, 2003). Gleichzeitig wird die Bedeutung der Bildregistrierung in der Forschung durch ihren Bedarf in klinischen Anwendungen widerspiegelt. Hierunter fallen nicht nur diagnostische Anwendungen sondern auch solche in den Bereichen Bildaquisition sowie Behandlungsplanung, -durchführung und -evaluation (MAINTZ & VIERGEVER, 1998). Eingeschlossen sind hierbei die Bewegungserkennung (gegebenenfalls ergänzt durch Bewegungskorrektur), die Kombination von Bilddaten aus unterschiedlichen Quellen, die zeitliche Verlaufskontrolle von Kontrastmittelgaben sowie der Zeitreihenvergleich von Bildern. Konsequenterweise kann Bildregistrierung als eine notwendige Voraussetzung für eine Vielzahl von Methoden betrachtet werden, die zunehmend wichtiger für den klinischen Alltag werden.

Kurz gefasst besteht das Ziel der Bildregistrierung in der Zusammenführung von Information aus zwei Bildern. Hierzu ist ein Vektorfeld von Verrückungen (ein sogenanntes Verrückungsfeld) gesucht, so dass jede Position in dem einen Bild auf eine zugehörige und sinnvolle Position in dem anderen Bild abgebildet werden kann. Die Bedeutung von „sinnvoll“ wird üblicherweise mit der Forderung übersetzt, dass einerseits die Topologie gewahrt bleibt und andererseits eine bestimmte geometrische oder physikalische Eigenschaft erfüllt ist.

Bei dem gesuchten Verrückungsfeld unterscheidet man starre von nicht-starren Abbildungen. Letztere wiederum lassen sich entweder explizit durch Basisfunktionen oder implizit (z.B. als Lösung einer partiellen Differentialgleichung) darstellen. In dieser Arbeit konzentrieren wir uns auf nicht-starre Ansätze und verweisen für eine weitergehende Klassifikation von Ansätzen auf Übersichtsartikel,

z.B. von BROWN (1992), MAURER & FITZPATRICK (1993) oder MAINTZ & VIERGEVER (1998).

Eine Vielzahl von nicht-starren Ansätzen erlaubt es, ein bestimmtes Verhalten des Verrückungsfelds vorzuschreiben. Dieses kann von „fast starr“ bis „hoch elastisch“ reichen und wird typischerweise in einer Glattheitsforderung an das Verrückungsfeld ausgedrückt. Eine häufig benutzte Bedingung ist durch eine Regularisierung basierend auf dem linearen elastischen Potential der Verrückung gegeben. Gewöhnlich wird die Bedingung *global* angewendet, das heißt unabhängig von der Bildposition. Insbesondere ist die Bedingung unabhängig von lokalen Materialeigenschaften, die beispielsweise das elastische Verhalten von im Bild enthaltenen anatomischen Strukturen wiedergeben können.

Durch eine global konstante Bedingung lassen sich in der Regel zufriedenstellende Ergebnisse erzielen. Dennoch existiert eine Reihe von Fällen, in denen sich anatomische Strukturen unabhängig voneinander verhalten und sich die Erhaltung der Topologie als eine ungeeignete Voraussetzung herausstellt.

Bei Weichteilgewebe und Knochen führt der Gebrauch von einheitlichen elastischen Eigenschaften beispielsweise zu Deformationen, die entweder unnötig restriktiv sind (im Fall, dass eine Knochen-typische Elastizität vorgeschrieben wird) oder physikalisch unrealistisch sind (falls Knochen in derselben Weise wie Weichteilgewebe deformiert wird). Ein weiteres Beispiel für voneinander unabhängiges elastisches Verhalten tritt bei der Therapiekontrolle von Tumoren auf. In diesem Fall hat sich der Erhalt von Form oder Volumen in einem begrenzten Bildbereich (dem des Tumors) als sinnvoll herausgestellt.

Die Erhaltung der Topologie ist nicht mehr gegeben, falls anatomische Strukturen in einem Bild zusammenhängend, im anderen jedoch getrennt dargestellt sind. Dies tritt beispielsweise in der Folge eines ‘brain shifts’ am Übergang von Gehirn und Schädel auf. Für eine genauere Betrachtung benötigen wir zwei Begriffe – den einer *großen Spaltänderung* und den einer *topologischen Änderung*. Eine große Spaltänderung liegt vor, wenn zwei gegebene Strukturen durch einen großen Spalt im ersten Bild, jedoch durch einen kleinen Spalt im zweiten Bild getrennt sind. Wird der kleine Spalt immer weiter verkleinert, ergibt sich eine Situation, die sich topologisch von der vorherigen unterscheidet: Die Strukturen sind nicht länger voneinander getrennt, eine topologische Änderung hat stattgefunden. Auch wenn eine topologische Änderung als die logische Erweiterung einer großen Spaltänderung erscheint, so unterscheiden sie sich aus mathematischer Sicht in einem wichtigen Punkt: Während im Fall einer großen Spaltänderung die Abbildung zwischen den Bildern weiterhin stetig ist, kann im Fall einer topologischen Änderung eine Unstetigkeit im Verrückungsfeld auftreten.

Nach diesen Überlegungen ist es naheliegend, die Bedeutung einer „sinnvollen“ Abbildung neu zu interpretieren: Eine sinnvolle Abbildung im Kontext dieser Arbeit

- ermöglicht eine große Spaltänderung bzw. eine topologische Änderung,
- unterstützt lokale Materialeigenschaften und
- erlaubt lokal den Erhalt von Form oder Volumen.



Für ein medizinisches Beispiel, das sowohl lokal unterschiedliche Materialeigenschaften wie auch eine Änderung der Topologie enthält, greifen wir auf den Fall des ‘brain shift’ zurück. Ein solcher tritt nach der Öffnung des Schädels auf und bewirkt einerseits die Entstehung eines Spalts zwischen Gehirn und Schädel und andererseits ein Zusammensinken des Gehirns. Für die Registrierung eines präoperativ mit einem intraoperativ aufgenommenen Bild ergibt sich die folgende Aufgabe: Gesucht ist eine sinnvolle Abbildung, die einerseits das Gehirn deformiert, gleichzeitig jedoch die Form des Schädels erhält und zudem durch den zurückgeklappten und damit im Bild partiell unsichtbaren Hautlappen nicht beeinträchtigt wird. Für einen Registrierungsansatz, der das Verrückungsfeld einheitlich regularisiert und/oder global konstante Materialeigenschaften annimmt, stellt dies eine schwierige, wenn nicht sogar unlösbare Aufgabe dar.

Diese Arbeit stellt einen neuen Registrierungsansatz vor, der unterschiedliche Materialien berücksichtigt. Der Ansatz basiert auf einer physikalisch motivierten elastischen Regularisierung (BAJCSY & KOVAČIČ, 1989). Eine solche ist in unseren Augen besser an die Problemstellung angepasst als eine fluidal-basierte (CHRISTENSEN ET AL., 1996). Auch wenn die Modellierung eines Fluids topologische Änderungen erlaubt, so sind diese Änderungen nicht auf medizinisch sinnvolle Regionen wie den Gehirn-Schädel Übergang beschränkt sondern können an jedem beliebigen Ort im Bild auftreten. Ein elastischer Regularisierer wiederum ermöglicht die Wahl von Materialeigenschaften wie sie entweder typisch für Knochen oder für Weichteilgewebe sind. Allerdings beruht die physikalische Motivation dieses Ansatzes auf der Annahme von „kleinen“ Deformationen. Die Modellierung von großen Spaltänderungen oder gar von Änderungen in der Topologie sind hiermit nicht möglich und werden auf eine andere Art und Weise eingeführt.

Der Beitrag dieser Arbeit besteht in der Herleitung eines Registrierungsansatzes, der unterschiedliche elastische Eigenschaften in *demselden* Bild unterstützt. Aufbauend auf einem leistungsfähigen Ansatz aus der Literatur wurden variable Regularisierer entwickelt, die lokal unterschiedliche Materialeigenschaften unterstützen und darüberhinaus große Spaltänderungen ermöglichen. Eine nochmalige Erweiterung des Konzepts führt schließlich auf stückweise variable Regularisierer, mit denen auch topologische Änderungen erzielt werden können.

Diese Arbeit gliedert sich wie folgt:

- Kapitel 2 stellt einen theoretischen Rahmen zur Bildregistrierung bereit. Ausgehend von einem kurzen Vergleich von parametrischen und nicht-parametrischen Ansätzen konzentrieren wir uns auf letztere und zeigen ihre Beziehung zu Randwertproblemen. Dieses Kapitel schließt mit dem Gebrauch einer Finite Differenzen Methode zur approximativen Lösung eines Randwertproblems.
- In Kapitel 3 wird ein leistungsfähiger Ansatz aus der Literatur beschrieben. Die Registrierung wird als eine Variationsaufgabe behandelt, was

in den Bereich der partiellen Differentialgleichungen führt. Neben einem elastisch-basierten Ansatz wird ein sogenannter diffusiver Ansatz untersucht. Aufgrund seiner simplen Struktur eignet sich dieser besonders gut für die Untersuchung von Variabilität in Regularisierern. Dieses Kapitel enthält außerdem eine Diskretisierung des resultierenden Systems von partiellen Differentialgleichungen und beschreibt deren numerische Lösung. Zum Schluss wird auf die Wahl des Regularisierungsparameters und der Materialparameter eingegangen.

- Kapitel 4 erweitert den Ansatz aus Kapitel 3 um Variabilität. Dies hat zur Folge, dass weiteres Vorwissen bereitgestellt werden muss, was in Form einer Segmentierung eines Ausgangsbildes erfolgt. Im Vergleich zu den Regularisierern aus dem vorherigen Kapitel zeichnen sich die hier entwickelten *variablen Regularisierer* durch eine höhere Komplexität – sowohl in theoretischer als auch in numerischer Hinsicht – aus. Ihre Fähigkeit, lokal unterschiedliche Materialeigenschaften sowie große Spaltänderungen zu unterstützen, wird abschließend demonstriert.
- Die Einbeziehung von topologischen Änderungen ist Inhalt von Kapitel 5. Das Verrückungsfeld kann hier nicht mehr als stetig angenommen werden, was die Herleitung von sogenannten *stückweise variablen Regularisierern* erfordert. Der fundamentale Unterschied zu den variablen Regularisierern besteht darin, dass nun bestimmte Bildbereiche entstehen oder verschwinden können. Allerdings erfordern die stückweise variablen Regularisierer eine aufwendige Segmentierung beider Bilder.
- Kapitel 6 stellt Ergebnisse der in dieser Arbeit entwickelten Methoden sowohl für synthetische als auch für medizinische Bilder vor.
- Kapitel 7 fasst die Resultate dieser Arbeit zusammen und schließt mit einem Ausblick auf weiterführende Fragestellungen.

---

# Abstract

---

This thesis is concerned with non-parametric non-rigid image registration. Here, a vector field of displacements is searched such that each position in one image is mapped onto a corresponding position in the other image.

Motivated by medical examples where after registration anatomical structures are deformed in a non-physical way, the overall aim lies in the incorporation of spatially varying material parameters to let each anatomical structure deform in a physically meaningful manner.

In addition, it is observed that preservation of topology, as usually assumed in registration, may be an unsuitable property for certain applications like, e.g., brain shift. To this end, the notions of a ‘large gap change’ (that is, if two structures are separated by a large gap in one image but by a small gap in the other image) and a ‘topological change’ (here, the gap totally vanishes in one image) are introduced. The challenge is now to derive a regularisation of the resulting displacement field which is spatially varying and allows for settings including a large gap change or a topological change.

Finally, locally a preservation of shape or volume may be reasonable, for instance in the treatment evaluation of tumors. Such a property, again, corresponds to a spatially adapted regularisation of the displacement field.

The main contribution of this thesis is the development of a framework for multiple-material registration. By extending a state-of-the-art approach for non-parametric image registration, variable regularisers are derived allowing for prescribing individual material properties and, moreover, supporting large gap changes. By further extending the concept towards piecewise variable regularisers, even topological changes can be achieved.



---

# Acknowledgements

---

I have been fortunate in having not just one supervisor but two:

Prof. Dr. Bernd Fischer on the university side and Dr. Astrid Franz on the Philips side guided me through three years of research. I am deeply grateful for their help and their encouragement, especially during the last stage. Also, I am thankful for this exciting and enjoyable time with an amount of freedom I probably won't have again.

A special thanks goes to Bernd who introduced me to the beautiful field of image processing. Moreover, I will always remember how you usually said that the best time for solving a newly arised problem was 'this afternoon'. In case of a hard problem you would probably schedule it for 'tomorrow', and the unsolvable ones were reserved for 'next week'; your way of not taking things too seriously I appreciated a lot.

Astrid, you have been a very pleasant office-mate. Thank you for all our discussions.

My next words are for two large groups of colleagues, one located at the Institute of Mathematics (University of Lübeck), here, in particular at the SAFIR research group, the other located at the Digital Imaging department (Philips Research Europe, Hamburg).

To name just a few, a hearty thanks goes to:

Dipl.-Ing. Thomas Blidung, Dr. Ingwer C. Carlsen, Dipl.-Math. Matthias Conrad, Dr. Martin Ludwig, PD Dr. Jan Modersitzki, Ursula Muuss, Dr. Thomas Netsch, Dr. Vladimir Pekar, Dr. Steffen Renisch, Birgit Schneider, Dipl.-Inf. Maike Wolf, and Stewart Young, Ph.D. All of you have made the time enjoyable, each of you in an individual way!

Die letzten Worte gehören Euch: meinen Eltern, Sabine und Lars.

Lars, Du bist mehr als nur ein Freund und ich danke Dir für die vergangenen fünf Jahre. Euch, meinen Eltern, danke ich für Eure Liebe – Ihr habt einen großen Anteil an meinem bisherigen Weg! Und schließlich Dir, Sabine, danke ich für überabzählbar vieles, während der letzten Wochen besonders für Deine Aufmunterung und das Ertragen auch all meiner schlechten Seiten.



---

# Contents

---

<b>Zusammenfassung</b>	<b>i</b>
<b>Abstract</b>	<b>v</b>
<b>Acknowledgements</b>	<b>vii</b>
<b>1 Introduction</b>	<b>3</b>
<b>2 Image Registration</b>	<b>9</b>
2.1 Images . . . . .	9
2.2 The Registration Problem . . . . .	10
2.3 Approaches for the Registration Problem . . . . .	12
2.3.1 Parametric Approaches . . . . .	13
2.3.2 Non-parametric Approaches . . . . .	15
2.4 Boundary Value Problems . . . . .	16
2.5 Finite Differences . . . . .	19
2.5.1 Domain Discretisation . . . . .	19
2.5.2 Difference Quotients . . . . .	21
2.5.3 Stencil Notation . . . . .	27
2.5.4 Assembling . . . . .	29
<b>3 Variational Approach</b>	<b>35</b>
3.1 Introduction into Calculus of Variations . . . . .	36
3.2 Boundary Conditions . . . . .	40
3.3 Image Registration as Variational Problem . . . . .	42
3.3.1 Similarity Measures . . . . .	42
3.3.2 Regularisation . . . . .	43
3.3.3 Link to Boundary Value Problems . . . . .	46
3.4 Discretisation . . . . .	47
3.5 Numerical Solution . . . . .	50
3.6 Choice of Parameters . . . . .	53
3.6.1 Regularisation Parameter . . . . .	53
3.6.2 Lamé Parameters . . . . .	56

<b>4</b>	<b>Variable Regularisation</b>	<b>61</b>
4.1	Motivation . . . . .	61
4.2	Variable Influence of Regularisation . . . . .	64
4.2.1	Choice of the Weighting Function . . . . .	64
4.2.2	Segmentation . . . . .	67
4.3	Variable Regularisation . . . . .	69
4.3.1	Variable Diffusive Regularisation . . . . .	70
4.3.2	Variable Elastic Regularisation . . . . .	72
4.3.3	Link to Boundary Value Problems . . . . .	73
4.3.4	Variable Stencil Notation . . . . .	75
4.4	Discretisation . . . . .	77
4.5	Numerical Solution . . . . .	83
4.6	Choice of Parameters . . . . .	85
4.6.1	Regularisation Parameter . . . . .	85
4.6.2	Lamé Parameters . . . . .	87
<b>5</b>	<b>Piecewise Variable Regularisation</b>	<b>89</b>
5.1	Calculus of Variations Revisited . . . . .	92
5.2	Discontinuities in Image Registration . . . . .	95
5.3	Discretisation . . . . .	98
5.4	Numerical Solution . . . . .	99
<b>6</b>	<b>Results</b>	<b>103</b>
6.1	Synthetic Images . . . . .	103
6.1.1	1D Case . . . . .	103
6.1.2	2D Case . . . . .	108
6.2	Medical Images . . . . .	112
6.2.1	Kinematic Imaging . . . . .	112
6.2.2	Radiotherapy Planning . . . . .	114
6.2.3	Brain Shift . . . . .	116
<b>7</b>	<b>Conclusions and Future Work</b>	<b>123</b>
	<b>Notation</b>	<b>125</b>
	<b>Bibliography</b>	<b>127</b>
	<b>Index</b>	<b>131</b>
	<b>Erklärung</b>	<b>133</b>
	<b>Lebenslauf</b>	<b>135</b>



---

# 1 Introduction

---

Image registration is one of the major topics in the field of image processing. It influences daily life with examples ranging from the automobile industry (e.g. driver assistance systems) over quality inspection (e.g. seals, displays or compact discs) to various medical applications.

In medical image processing, a substantial part of the research is devoted to image registration. PLUIM & FITZPATRICK (2003) observed an increasing number of journal publications in this field over the past two decades. The relevance of image registration in the research community is reflected by its demand for clinical applications. Such applications occur not only within diagnostic settings, but also in the areas of acquisition, planning, treatment, and evaluation (MAINTZ & VIERGEVER, 1998). They include motion detection (possibly followed by motion compensation), the fusion of data from different sources, treatment verification, the monitoring of agent injections evolving in time, and the study of temporal series of images (also called follow-up studies). Consequently, image registration can be seen as an application enabler with increasing impact on the daily clinical practise.

In general, the purpose of image registration is to relate the information contained in one image to information given in another image. To this end, a vector field of displacements is searched such that each position in the one image is mapped onto a corresponding and meaningful position in the other image. By the notion ‘meaningful’ often a type of constraint is meant which both preserves the topology and prescribes a certain geometrical or physical property in the entire image domain.

The mapping to be determined is of rigid or of non-rigid type. In the latter case, it can be described either explicitly in terms of basis functions or implicitly, for instance as the solution to a partial differential equation. In the following, we focus on non-rigid approaches and refer for further classification and commentaries to surveys carried out by, e.g., BROWN (1992), MAURER & FITZPATRICK (1993), and MAINTZ & VIERGEVER (1998).

Many non-rigid approaches allow for prescribing a certain ‘behaviour’ of the resulting displacement field ranging from ‘almost rigid’ to ‘fully elastic’. Typ-

ically, the displacement is computed subject to a smoothness constraint. A widely chosen constraint is realised by a regularisation based on the linear elastic potential of the displacement, see, e.g., (BAJCSY & KOVAČIČ, 1989; MODERSITZKI, 2004; CLARENZ ET AL., 2006) and references therein. Frequently, the constraint is applied globally with one global regularisation parameter and with elastic properties independent of the image position and, therefore, independent of the elastic behaviour of the corresponding anatomical structure.

Often, a globally uniform constraint provides satisfactory results due to the underlying physical model. Nevertheless, there exist several cases where anatomical structures behave different from each other and/or where preservation of topology is unsuitable.

Soft tissue, for instance, is of different elasticity compared to bone structures. Therefore, the prescription of a uniform elastic behaviour may lead to deformations which are either unnecessarily restricted (when choosing elastic properties typical of bone structures) or physically unrealistic (if bone structures get deformed as soft tissue). Another demand for non-uniform behaviour occurs within the treatment evaluation of tumors. Here, preservation of shape or volume may be a reasonable property in a certain image region, i.e. the tumor region, but not in the entire image domain.

A change in topology happens if anatomical structures are connected in one image but disconnected in the other image, like the brain-skull interface subject to a brain shift. To explain this issue in more detail, we consider a setting called a *large gap change*, that is, if two structures are separated by a large gap in one image but separated by a small gap in the other image. By shrinking the small gap even more, a setting can be achieved which is topologically different from the original one: The structures are no longer separated and a *topological change* has occurred. Although a topological change simply turns out to be the logical extension of a large gap change, from a theoretical point of view there is an important distinction when considering the mapping from the one image onto the other: In case of a large gap change the mapping remains continuous but in case of a topological change a discontinuity in the displacement field may show up. Also, we note that a discontinuous displacement field is reasonable if adjacent structures move relative to each other, like the liver or a joint and their surrounding tissues.

Before illustrating these issues with a medical example, the considerations drawn above are summarised into a reinterpretation of the notion ‘meaningful’: In this thesis a meaningful mapping

1. enables large gap changes (or even changes in topology),
2. supports local material properties, and,
3. allows locally for shape or volume preservation.

An example which involves both anatomical structures of different elasticity and a topological change is depicted in Figure 1.1. Here, slices from three-dimensional data sets are displayed. On the left, the head of a patient is shown pre-operatively, on the right in an intra-operative state. For a tumor resection,

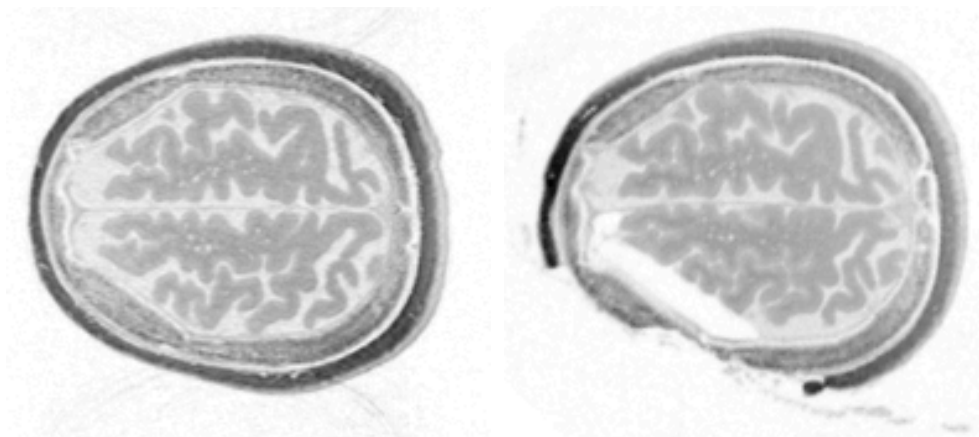


Figure 1.1: Example for a registration problem involving both anatomical structures of different elasticity and a topological change. The change in topology is caused by a brain shift while transition from the pre-operatively generated image (left) onto the intra-operatively generated one (right). Image courtesy of Dr. Hastreiter, Department of Neurosurgery, Friedrich Alexander University of Erlangen-Nuremberg.

the skin (darkest structure) has been partially removed and the skull (depicted in medium gray) has been opened (the opening itself is not visible in the depicted slice) causing a brain shift. The brain shift can be detected on one hand by an arising gap (consisting of air and liquor) between skull and brain tissue, on the other hand by a shrinkage of the brain.

The challenge is now to determine a meaningful mapping which deforms the brain while preserving the shape of the skull, and which is not misled by the partially missing skin. Certainly, a registration of this image pair is a hard or even unsolvable task for any approach which regularises the displacement field uniformly and/or assumes globally constant material properties.

In the literature one can find several attempts dealing with non-rigid image registration in conjunction with spatially varying regularisation or material parameters. They can be classified as either parametric or non-parametric. The latter can be distinguished further into surface- and volume-based approaches.

Parametric approaches based on, for instance, damped spring models (ŠKRINJAR ET AL., 2002; EDWARDS ET AL., 1998), radial basis functions (ROHDE ET AL., 2003; DUAY ET AL., 2004) or B-splines with subsequent filtering (STARING ET AL., 2005) have been shown to allow for a locally varying deformability of the resulting displacement field. In addition, with the damped spring models, anatomical structures can behave independently from each other including the possibility of topological changes. Here, a network of springs is modelled to constrain deformation of tissue structures; bone structures, in contrast, are kept rigid while fluid regions, such as the cerebral spinal fluid, may deform freely. By either utilising a contact algorithm (ŠKRINJAR ET AL., 2002), adding an energy term (EDWARDS ET AL., 1998) or constraining the parameters (ROHDE ET AL., 2003), folding of structures can be avoided.

Although incorporating a kind of tissue constraint, these approaches tend to

result in a displacement field interpolating smoothly across soft tissues, rather than to model the physics of tissues accurately. In particular, the elastic properties of tissue, such as its (in)compressibility or Young's modulus, cannot be controlled.

Often, non-parametric approaches incorporating physical properties of tissue have been proposed as part of a biomechanical model for brain applications. Here, based on a segmentation into (at least) bone and tissue structures, an initial estimate of the displacement field is computed. However, this estimate is restricted to the surfaces of the segmented regions. To model the displacement field in the entire domain, in a second step either the Navier-Lamé equations or the Navier-Stokes equations is employed. For the discretisation of the differential equations numerous schemes are used, e.g. a finite difference method (DAVATZIKOS, 1996; WANG & STAIB, 2000), a finite element method (FERRANT ET AL., 2001; ŠKRINJAR ET AL., 2002) or a boundary element method (ECABERT ET AL., 2003). All these approaches have been reported to be accurate close to the segmented surfaces. However, since no volumetric information is exploited, the estimated displacement field may be less accurate far away from the surfaces.

The drawback of a possibly reduced accuracy can be overcome by including volumetric information as, for instance, in works by LESTER ET AL. (1999), HAGEMANN (2001), REXILIUS ET AL. (2002), and EHRHARDT ET AL. (2003). These methods either support spatially varying material properties or employ a coupled model (for instance, consisting of regions modelled as rigid, elastic, or viscous fluid). Like the surface-based approaches, these methods do not allow for topological changes.

In this thesis we present a new approach for multiple-material image registration which overcomes the shortcomings mentioned before. We investigate a physically motivated constraint for elastic regularisation which is based on the linear elastic potential of the displacement (BAJCSY & KOVAČIČ, 1989).

In our view, an elasticity-based approach is better adapted to our problem than a fluid-based one (CHRISTENSEN ET AL., 1996): Although the modelling of a viscous fluid allows for topological changes, such changes are not restricted to the desired regions (like the brain-skull interface) and may thus occur everywhere in the image, which is not our intent. Moreover, we refrain from the use of coupled models since these require coupling conditions at the interfaces which adds significant complexity to the structure of the equation system to be solved numerically.

Within an elasticity-based approach, an individual choice of material parameters allows us to cope with bone structures as well as with soft tissue. However, by the linear elastic potential only small deformations can be described and, therefore, the modelling of large gap changes or topological changes is not supported and have to be introduced in a different way.

The main contribution of this thesis is the development of a framework for multiple-material registration. By extending a state-of-the-art approach for non-parametric image registration, variable regularisers are derived allowing

for prescribing individual material properties and, moreover, supporting large gap changes. By further extending the concept towards piecewise variable regularisers, even topological changes can be achieved.

This thesis is organised as follows.

Chapter 2 provides a general framework for image registration. Based on a short comparison of parametric and non-parametric approaches, we focus on the latter and show their relation to boundary value problems. Finally, this chapter demonstrates the use of a finite difference method to approximately solve a boundary value problem.

In Chapter 3, a state-of-the-art approach for image registration is described. The registration problem is treated as a variational problem which involves the solution of a system of partial differential equations. Apart from an elasticity-based regulariser, a so-called diffusive regulariser is investigated. Its simple structure makes it an optimal candidate for studying variable registration approaches in the following chapters. Furthermore, this chapter presents a discretisation of the derived system of equations and comments on its numerical solution. Finally, the choice of regularisation and material parameters is discussed.

Chapter 4 incorporates variability into the approach from Chapter 3. As a consequence, further a priori knowledge has to be added and is given by a segmentation. Compared to the state-of-the-art regularisers, the variable regularisers are more complex in terms of theoretical derivation and numerical solution. However, they allow for locally varying material properties and support large gap changes as demonstrated at the end of this chapter.

The incorporation of topological changes is subject of Chapter 5: The displacement field is no longer necessarily continuous and, consequently, the derivation of so-called piecewise variable regularisers requires more care. A registration based on these regularisers allows certain image regions to appear or vanish which is a fundamental difference to the previous chapter. However, it will turn out that these regularisers are possibly less suited for clinical applications since they require the costly segmentation of both images to be registered.

Chapter 6 presents results for multiple-material registration problems. Starting with synthetic examples we investigate the properties of the newly developed registration scheme. Finally, medical applications are investigated.

Chapter 7 summarises this thesis, points out possible extensions, and concludes with suggestions for future work.



---

## 2 Image Registration

---

This chapter gives an introduction into image registration. Clearly, images play the key role in registration and we start the introduction by defining an image in a mathematical sense. Based on this setting, the task of image registration can be stated resulting in a mathematical model. Finally, a numerical method is required to approximate a solution of the mathematical model. We will describe this issue in the last section of this chapter.

### 2.1 Images

An image can be interpreted as an exposure of a scene from the real-world. Typically, the scene is assumed to be three-dimensional whereas the exposure displays an extraction of the scene. The extraction may vary from a one-dimensional line extraction over the two-dimensional extraction of a slice to the original three-dimensional scene. We start by an exploration of the properties of such an exposure and denote its dimensionality by  $d \in \mathbb{N}$ .

Regarding the area of an exposure we observe its connected nature and its finite size, i.e., it does not decompose in separated subareas and the exposure is bounded. For mathematical reasons we do not include the boundary in the area.

**Definition 2.1** (Domain). *A domain  $\Omega \subset \mathbb{R}^d$  is given by a bounded, open and connected subset. The boundary of  $\Omega$  is denoted by  $\partial\Omega$  and its closure by  $\bar{\Omega} = \Omega \cup \partial\Omega$ .*

Although the boundedness usually does not belong to the properties of a domain, cf., e.g. (KÖNIGSBERGER, 2004), in image registration it is obvious to assume this property due to the boundedness of an exposure.

Thus, an exposure of a scene can be seen as a mapping from the domain of the exposure onto some quantity represented by one or more channels of intensity-values. In this thesis only grey-scale images are considered, thus one channel of information is sufficient. We will use the terms ‘intensity-value’ and ‘grey-value’ interchangeably.

We assume that the intensity-values of an exposure can be described by a ‘smooth’ function. Here, a function is called smooth if, depending on the context, it has sufficiently many continuous derivatives.

**Definition 2.2** (Image). *Given a  $d$ -dimensional domain  $\Omega$ , a  $d$ -dimensional image  $I$  is defined as a smooth mapping  $I : \bar{\Omega} \rightarrow [0, 1]$ . In addition, let  $\text{Img}(\Omega)$  define the set of images on the domain  $\Omega$ .*

Note that the exact degree of differentiability required for  $I$  depends on the mathematical model, see Section 3.3.

In medical applications one is faced with images which are not differentiable, the so-called *digital images* (or discrete images). In the first instance, a digital image seems to be unsuitable for a mathematical model which is based on differentiable functions. However, an image according to Definition 2.2 can be linked to a digital image such that the differentiability requirement is fulfilled. Before establishing this link, we give a short overview on the origin of a digital image.

Digital images are produced by an image acquisition sensor measuring some quantity, e.g. the attenuation of x-rays in *computer tomography* (CT), electromagnetic energy in *magnetic resonance tomography* (MR), photon emissions in *positron emission tomography* (PET) or *single photon emission computed tomography* (SPECT). The measurement entails some sampling and quantisation method which depends on the acquisition device. In principle, the human body (i.e. the scene) is treated as a regular grid. A digital number is assigned to each element of the grid. Such an element is named *lixel* (line element, in one space dimension), *pixel* (picture element, in two dimensions) or *voxel* (volume element, in any dimension  $d \in \mathbb{N}$ ). Its value describes an intensity level corresponding to some physical process, e.g. a rate of radioactive decay in nuclear imaging.

**Definition 2.3** (Digital Image). *Given a  $d$ -dimensional domain  $\Omega$ , numbers  $N_1, N_2, \dots, N_d \in \mathbb{N}$ , and an array  $X \in \mathbb{R}^{N_1 \times N_2 \times \dots \times N_d}$  consisting of points  $x \in \bar{\Omega}$ , a  $d$ -dimensional digital image  $I$  is defined as a mapping  $I : X \rightarrow [0, 1]$ .*

However, for the mathematical model described in the following section, the digital image has to be transformed into a (smooth) image according to Definition 2.2. This can be done, for instance, by solving an interpolation problem with appropriately chosen basis functions. In turn, a digital image can be interpreted as a sampled version of a smooth image.

## 2.2 The Registration Problem

Having ensured that images are differentiable, we can start to develop a mathematical model in order to formulate the image registration problem. Generally spoken, the problem of image registration describes the task of

*finding a geometric transformation between two given images.*



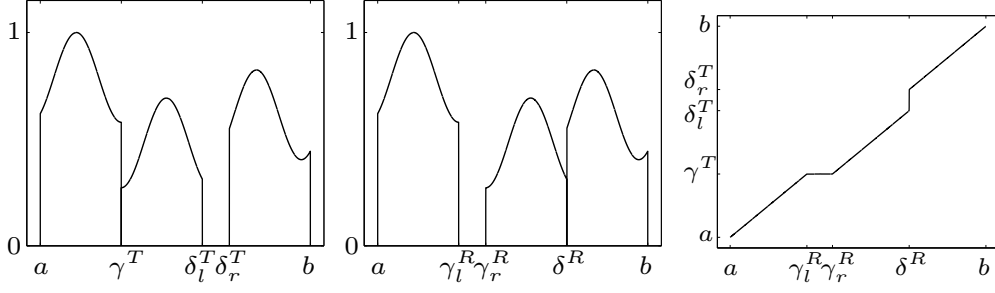


Figure 2.1: Artificial one-dimensional image  $T$  (left) which can be transformed into  $R$  (centre) using a mapping  $\varphi$  (right).

Typically, one of the images is viewed as a reference image  $R \in \text{Img}(\Omega_R)$  defined on a domain  $\Omega_R$ , the other one as a deformable template image  $T \in \text{Img}(\Omega_T)$  defined on a domain  $\Omega_T$ . The domains are linked by the geometric transformation which maps the domain of the reference image onto the one of the template image,  $\varphi : \Omega_R \rightarrow \Omega_T$ . For an example we refer to Figure 2.1 where both domains are given by the interval  $[a, b]$  and the one-dimensional images are linked by the transformation  $\varphi$ , i.e.  $T \circ \varphi = R$ .

Note that the application of  $\varphi$  is understood in a *backward Lagrangian* sense. That is, for a position  $x \in \Omega_R$  a grey-value at position  $\varphi(x) \in \Omega_T$  is taken from the template image and allocated to a new image (defined on  $\Omega_R$ ) at position  $x$ . In contrast,  $T \circ \varphi$  understood in a *forward Lagrangian* sense allocates a grey-value  $T(x)$  with  $x \in \Omega_T$  to those positions in a new image (defined on  $\Omega_R$ ) which are mapped onto  $x$  by  $\varphi$ . However, in the remaining part of the thesis we will choose the backward Lagrangian framework since this setting is well adapted to the numerical treatment of the registration problem.

In general, a transformation  $\varphi$  such that  $T \circ \varphi = R$  may not exist. Instead,  $\varphi$  is searched in such a way that the transformed template image  $T \circ \varphi$  is ‘similar’ to the reference image  $R$ . For a mathematical treatment, ‘similarity’ needs to be measured in some way. To this end, a similarity (or distance) measure is required that assigns a scalar (distance) value to a given pair of images.

Note that  $\varphi$  can be split up into the identity mapping as the trivial part and a displacement<sup>1</sup> part  $u$ , i.e.  $\varphi(x) = x + u(x)$ .

**Problem 2.4** (Registration Problem). *For given domains  $\Omega_T$  and  $\Omega_R$ , images  $T \in \text{Img}(\Omega_T)$ ,  $R \in \text{Img}(\Omega_R)$ , and  $\mathcal{D} : \text{Img}(\Omega_T) \times \text{Img}(\Omega_R) \times \mathcal{C}^p(\bar{\Omega}_R, \mathbb{R}^d) \rightarrow \mathbb{R}_0^+$  as a similarity measure, the registration problem is to find a mapping*

$$\varphi \in \mathcal{C}^p(\bar{\Omega}_R, \bar{\Omega}_T), \quad \varphi(x) := x + u(x),$$

<sup>1</sup>In the literature a displacement is often called a transformation or a deformation. Here, we differentiate between the *transformation*  $\varphi$  and the *displacement*  $u$  (as the non-trivial part of the transformation). A *deformation*, however, is understood in a physical sense, e.g. the deformation of an elastic body. Consequently, a deformation is also a displacement but a displacement is only a deformation if the underlying transformation is non-rigid (otherwise the body does not get deformed but only translated or rotated).

such that for some functional  $F$

$$\mathcal{D}_{T,R}[u] := \int_{\Omega_R} F[T \circ \varphi, R] dx \xrightarrow{u} \min .$$

Thus, the task of image registration can be formulated as the minimisation of  $\mathcal{D}$  resulting in a displacement  $u$  such that the similarity of  $T \circ \varphi = T \circ (\text{id} + u)$  and  $R$  is maximised<sup>2</sup>. A minimum requirement for  $p$  as the degree of differentiability of  $\varphi$  (or  $u$ ) is pointed out in the following example.

**Example 2.5.** Let a similarity measure be given by

$$\mathcal{D}_{T,R}[u] := \int_{\Omega_R} [(T \circ \varphi)(x) - R(x)]^2 dx$$

and consider two chessboards as images  $T$  and  $R$ . Then, any black square in  $T$  can be mapped to any black square in  $R$ . In all cases the similarity measure will indicate a minimum but in most cases the mapping  $\varphi$  is not continuous. Restricting, however, the set of admissible mappings to  $\mathcal{C}(\Omega_R)$ , i.e. the set of continuous mappings defined on  $\Omega_R$ , it both reduces the set of admissible mappings and leads to a result being more satisfactory from an application point of view.

Summarising, the registration problem takes two images and searches for a smooth mapping such that this mapping applied to the first image results in a (new) image similar to the second one. The mapping can be described by either a geometric transformation  $\varphi$  or a displacement (field)  $u$ .

For a more convenient notation we omit the differentiation between  $\Omega_T$  and  $\Omega_R$  and define a single domain  $\Omega := \Omega_T \cup \Omega_R$  instead.

## 2.3 Approaches for the Registration Problem

In this section the displacement field  $u$  as a solution to the Registration Problem 2.4 will be further investigated. We start by considering the requirements formulated in Chapter 1, namely

- to support different material properties and
- to allow for large gap changes

in the registration problem. While different material properties may be incorporated in  $\mathcal{D}$  in some way, the incorporation of a large gap change is a complex task as can be seen from Figure 2.1. When shrinking a gap region of width  $w$ , e.g. the interval  $[\delta_l^T, \delta_r^T]$ , to a gap of small size, two positions  $\delta_l^R, \delta_r^R$  with small distance are required to be mapped onto positions  $\delta_l^T = \varphi(\delta_l^R), \delta_r^T = \varphi(\delta_r^R)$  with  $|\delta_l^T - \delta_r^T| = w$ . This requires in the gap region a large gradient of  $\varphi$  (and thus of  $u$ ) or – in the limit case – even a discontinuity in  $\varphi$ .

---

<sup>2</sup>A maximised similarity of two images is equivalent to a minimised distance between these images. Since the term ‘distance’ reminds of a geometric distance (which applies only for special cases, cf. Section 3.3.1), we prefer the use of the term ‘similarity’.

Another observation about the Registration Problem 2.4 is included in the following example.

**Example 2.6.** Consider a similarity measure and images showing chessboards as in Example 2.5 but now with a translated second chessboard  $R$  such that the center of each square in  $T$  is located on an edge of a square from  $R$ . Now, each black square in  $R$  is moved a bit. Depending on the movement, an optimisation routine<sup>3</sup> determines a solution  $\varphi$  to the Registration Problem 2.4 where  $\varphi$  transforms each black square in  $R$  to the nearest black square from  $T$ . However, the choice of the nearest black square from  $T$  depends on the initial movement and small changes in the image data lead to large changes in the resulting transformation.

The effect of small changes in the input data leading to large changes in the output data, causes – beside the non-existence and the non-uniqueness of a solution – a problem to be *ill-posed*. In the literature several methods are known to circumvent the ill-posedness of a registration problem, e.g. (MODERSITZKI, 2004; CLARENZ ET AL., 2006). So-called parametric approaches restrict the search space of all differentiable functions to a finite-dimensional subspace and describe the searched transformation in terms of a finite number of basis functions. In contrast, the transformation in non-parametric approaches is no longer restricted to a parametrisable set. Instead, the search space is infinite-dimensional and the well-posedness is ensured by adding a regularising term to the similarity measure. In the following, examples for different search spaces are given and discussed with respect to their ability to allow for topological changes and for different material properties.

### 2.3.1 Parametric Approaches

Typical examples for parametric approaches are given below.

- **Rigid and affine linear displacements**

Let  $E_d$  denote the identity matrix of size  $d \times d$ . A displacement given by a mapping

$$u(x) = Ax + b, \text{ where } A \in \mathbb{R}^{d \times d} \text{ with } \det(E_d + A) > 0 \text{ and } b \in \mathbb{R}^d,$$

allows for an affine linear transformation including shearing and scaling. If, in addition,  $E_d + A$  is orthogonal with  $\det(E_d + A) = 1$ , only translation and rotation are allowed and the transformation is called rigid. In Figure 2.2, left, as an example, a two-dimensional Cartesian grid function is transformed by the affine-linear displacement  $u$  with

$$A = \begin{pmatrix} 0.10 & 0.22 \\ 0.22 & -0.12 \end{pmatrix} \quad \text{and} \quad b = \begin{pmatrix} -0.13 \\ -0.05 \end{pmatrix}.$$

---

<sup>3</sup>The choice of a specific optimisation scheme is not the key point here; as an example, the reader may think of a steepest gradient approach.

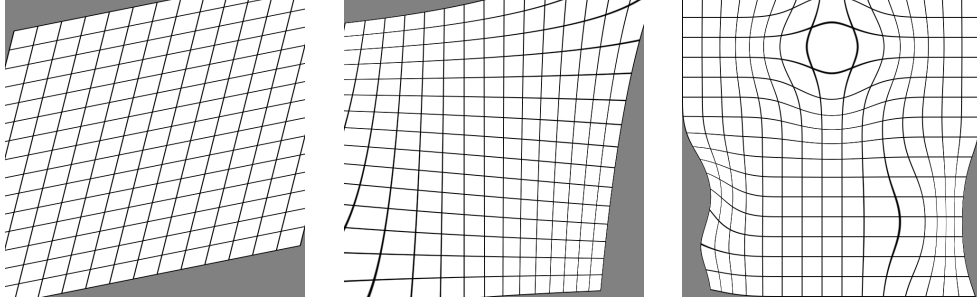


Figure 2.2: Examples for displacements based on affine, polynomial and B-spline functions (from left to right).

- **Polynomial displacements**

Here,  $u$  is given as a polynomial function defined on  $\mathbb{R}^d$ . As an example, in Figure 2.2, centre, the mapping

$$u(x) = \begin{pmatrix} (x_1 - 0.3)(x_1 - 0.9)(x_2 - 0.5) \\ (x_2 - 0.4)(x_2 - 0.5)(x_1 - 0.1) \end{pmatrix}$$

is applied to a Cartesian grid in  $\mathbb{R}^2$ .

- **B-spline displacements**

Taking a linear combination with coefficients  $\beta$  and B-splines  $B_i(x)$  as basis functions, a displacement given by a mapping

$$u(x) = \sum_{n_1} \cdots \sum_{n_d} \beta_{n_1, \dots, n_d} \prod_{i=1}^{n_d} B_i(x)$$

with  $n_i$ ,  $i = 1, \dots, d$ , depending on the spline degree, is called a B-spline displacement (cf. Figure 2.2, right, for an application to a two-dimensional Cartesian grid). A typical property of this type of displacement is the local influence of the coefficients  $\beta_{n_i}$ . Their region of influence depends on the spline degree and the number of basis functions. Usually, B-splines are defined on a regular grid but, basically, non-regular grids can be used as well. Such grids allow for an adaptive placement of basis functions but require a costly computation of the displacement, cf. (PECKAR, 1998).

A classification of these approaches with respect to their ability to allow for large gap changes or for different material properties is displayed in Table 2.1. Note that the last row of the table concerning a non-parametric approach is discussed in the following section.

Clearly, affine linear transformations cannot be used for either of these tasks. The same result applies to a polynomial transformation where a material dependency cannot be included and where, with reasonable effort, an approximated discontinuity as in Figure 2.1 cannot be achieved satisfactorily. For a B-spline displacement a local material property may be incorporated via the coefficients  $\beta_{n_i}$ . To illustrate a large gap change we consider a simple example showing two objects with a small gap between them (cf. Figure 2.3, left). Then, various

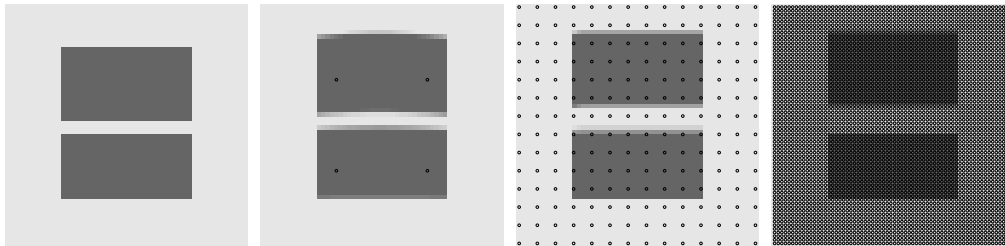


Figure 2.3: Synthetic example showing a gap to be enlarged (left). Various B-spline displacements with basis functions of grid spacing  $1/3$ ,  $1/15$ , and  $1/75$  of the image width are employed (centre left to right). The position of the B-splines is marked by circles.

Table 2.1: Classification of approaches with respect to their ability to allow for large gap changes (second column) or for different material properties (last column). See Sections 2.3.1 and 2.3.2 for further comments.

	gap changes	material properties
rigid/affine linear	—	—
polynomial	—	—
B-splines	(+)	+
non-parametric	+	+

displacements based on grids of varying density of basis functions (distributed equidistantly on a grid with spacings of  $1/3$ ,  $1/15$ , and  $1/75$  of the image width) are used in order to enlarge the gap without affecting the adjacent objects. From Figure 2.3, centre left to right, we observe that a simultaneous enlargement of the gap and shape preservation of the objects is possible but requires a grid spacing of smaller than voxel size. A small grid spacing, however, gives rise to a large computational effort and, therefore, we classify a B-spline displacement to be of limited ability for large gap changes, cf. Table 2.1. The classification remains the same if non-regular grids as described in, e.g., (PECKAR, 1998) are used. Their costly computation is not compensated by requiring a small grid spacing in the gap region only.

### 2.3.2 Non-parametric Approaches

In a non-parametric approach the search space is infinite-dimensional and given by, for instance, the class of differentiable functions equipped with some boundary conditions. While in a parametric approach we were looking for optimal parameters of some expansion of the transformation, here, no parameters are involved in the representation of the transformation. To avoid the ill-posedness of the registration problem an often used method is to add a regularising (or smoothing) term. Usually, the regulariser has to be chosen application-dependent, see (MODERSITZKI, 2004; CLARENZ ET AL., 2006) and references therein. Breathing movements in the thorax, for instance, result in a globally smooth displacement field, whereas heart beat or joint movements are cases

where a more sophisticated choice of the regularising term<sup>4</sup> is essential. Independent of specific applications, the Registration Problem 2.4 is rewritten by adding a regularisation term.

**Problem 2.7** (Regularised Registration Problem). *Given a domain  $\Omega$ , images  $T, R \in \text{Img}(\Omega)$ , a similarity measure  $\mathcal{D} : \text{Img}(\Omega) \times \text{Img}(\Omega) \times \mathcal{C}^p(\bar{\Omega}, \mathbb{R}^d) \rightarrow \mathbb{R}_0^+$ , a regularising term  $\mathcal{S} : \mathcal{C}^p(\mathbb{R}^d, \mathbb{R}^d) \rightarrow \mathbb{R}_0^+$  and a positive weight  $\alpha \in \mathbb{R}^+$ , the regularised registration problem is to find a mapping  $u \in \mathcal{C}^p(\bar{\Omega}, \mathbb{R}^d)$  such that*

$$\mathcal{D}_{T,R}[u] + \alpha \mathcal{S}[u] \xrightarrow{u} \min . \quad (2.1)$$

Note that  $p$  will be specified in Section 3.3.

In contrast to a parametric approach, here, an example for the mapping  $u$  cannot be given in an explicit form. Implicitly,  $u$  is described by the minimisation problem in (2.1), where the regularising term can be chosen as, e.g., the linear elastic potential. A spatially varying choice of elastic properties can then be used to model a dedicated elastic behaviour in a specific image region. Furthermore, by allowing the regularisation weight  $\alpha$  to be spatially dependent, the regularisation influence can be weighted variably. Decreasing  $\alpha$ , for instance, in a gap region may lead to a mapping  $u$  which is locally less smooth, and, therefore, allows for a large gradient as required to approximate the transformation in Figure 2.2. Consequently, in Table 2.1 the non-parametric approach is classified as being able to achieve both goals.

Returning to the Registration Problem 2.7 we note that, in general, it does not possess an analytical solution in explicit form. However, a numerical solution can be obtained, for instance by determining its Gâteaux derivative. In broad outline we note that the Gâteaux derivative of (2.1) yields a system of continuous equations and of boundary conditions. The equations are of differential type and can be, together with the boundary conditions, described by a boundary value problem. For a comprehensive description of how to achieve this problem in the context of image registration, we refer to the following chapter. Here, we turn our attention towards the numerical treatment of boundary value problems.

## 2.4 Boundary Value Problems

*Boundary value problems* belong to the most important problems in mathematical physics. Here, one seeks a function satisfying both a system of partial differential equations on a domain  $\Omega$  and specified conditions on the boundary of the domain. While for the Registration Problem 2.7 the differential equations arise from the definition of the similarity measure  $\mathcal{D}$  and the regularisation term  $\mathcal{S}$ , the boundary conditions may depend on  $\mathcal{D}$  and  $\mathcal{S}$ , too. Alternatively, they may be explicitly incorporated in the definition of the space of admissible functions. Two types of boundary conditions shall be investigated in this thesis,

---

<sup>4</sup>For a closer interpretation and examples of regularising terms we refer to Section 3.3.

- a (homogeneous) *Dirichlet* boundary condition,

$$u(x) = 0, \quad x \in \partial\Omega, \quad (2.2)$$

- and a (homogeneous) *Neumann* boundary condition,

$$\frac{\partial u(x)}{\partial \mathbf{n}} = 0, \quad x \in \partial\Omega, \quad (2.3)$$

with  $\mathbf{n}$  the outward pointing unit normal vector. Note that, here and in the following, one-sided derivatives are considered on  $\partial\Omega$ .

Alternatively, (2.2) and (2.3) can be combined to

$$Bu(x) = 0, \quad x \in \partial\Omega, \quad (2.4)$$

with a boundary operator  $B = \text{id}$  in the first case and  $B = \partial/\partial\mathbf{n}$  in the latter case. A boundary value problem arising in this thesis is now of the following form.

**Definition 2.8** (Boundary Value Problem). *Given a domain  $\Omega$ , a linear differential operator  $L$ , the boundary operator  $B$  from (2.4), and a continuous mapping  $f : \mathbb{R}^d \rightarrow \mathbb{R}^d$ , the boundary value problem is to find a smooth mapping  $u : \bar{\Omega} \rightarrow \mathbb{R}^d$  satisfying*

$$\begin{aligned} Lu(x) &= f(u(x)), & x \in \Omega, \\ Bu(x) &= 0, & x \in \partial\Omega. \end{aligned} \quad (2.5)$$

Here,  $f$  is typically a non-linear function and will be given explicitly, just as  $L$ , based on the registration problem in Chapter 3.

Without doubt, existence and uniqueness of a solution are important properties of a boundary value problem. For a one-dimensional problem these properties can be easily verified. However, in more than one dimension it is a challenging task to establish these properties and further assumptions on  $L$  and  $f$  are required. We do not investigate this issue further and refer to the literature where existence and uniqueness have been shown for special problems from image registration (CLARENZ ET AL., 2002). In the remaining part of this thesis, we shall keep in mind that the term ‘solution’ not necessarily implies uniqueness.

Due to the occurrence of  $u$  on the right-hand side of the differential equation in (2.5), the equation is non-linear in  $u$ . A popular approach to resolve the non-linearity is the so-called *fixed-point type iteration scheme*. Starting with an initial guess  $u^{(0)}$  fulfilling the boundary condition in (2.5), the differential equation in (2.5) is replaced by

$$Lu^{(l+1)}(x) = f(u^{(l)}(x)), \quad x \in \Omega, \quad l \in \mathbb{N}_0. \quad (2.6)$$

For appropriate  $L$  and  $f$ , Banach’s fixed point theorem ensures convergence and the limit function  $\lim_{l \rightarrow \infty} u^{(l)}$  solves (2.5). However, MODERSITZKI (2004)

reported instabilities while solving (2.6) for an image registration problem and suggested for an improved stability the following slight modification,<sup>5</sup>

$$kLu^{(l+1)}(x) + u^{(l+1)}(x) = kf(u^{(l)}(x)) + u^{(l)}(x), \quad x \in \Omega, l \in \mathbb{N}_0, \quad (2.7)$$

with  $k \in \mathbb{R}^+$ . Then, (2.7) is equal to

$$\frac{u^{(l+1)}(x) - u^{(l)}(x)}{k} = -[Lu^{(l+1)}(x) - f(u^{(l)}(x))], \quad x \in \Omega, l \in \mathbb{N}_0, \quad (2.8)$$

which is sometimes referred to as a semi-implicit *time-marching approach*. Furthermore, it may be interpreted as the temporal discretisation of an *initial boundary value problem* with  $k$  as the step size of an artificial time.

**Definition 2.9** (Initial Boundary Value Problem). *Given a domain  $\Omega$ , a linear differential operator  $L$ , the boundary operator  $B$  from (2.4), a continuous mapping  $f : \mathbb{R}^d \rightarrow \mathbb{R}^d$ , and a smooth initial mapping  $u^{(0)} : \bar{\Omega} \rightarrow \mathbb{R}^d$ , the initial boundary value problem is to find a smooth mapping  $u : \bar{\Omega} \times \mathbb{R}_0^+ \rightarrow \mathbb{R}^d$  satisfying*

$$\begin{aligned} \frac{\partial u(x, t)}{\partial t} &= -[Lu(x, t) - f(u(x, t))], & x \in \Omega, t \in \mathbb{R}^+, \\ u(x, 0) &= u^{(0)}(x), & x \in \bar{\Omega}, \\ Bu(x, t) &= 0, & x \in \partial\Omega, t \in \mathbb{R}^+. \end{aligned} \quad (2.9)$$

Now, instead of a spatial problem, a spatial-temporal problem is to be solved. As a matter of fact, the solution to the boundary value problem, (2.5), is closely connected with the one to the initial boundary value problem, (2.9): Inserting a solution of (2.5) into (2.9) yields  $\partial u / \partial t = 0$  indicating a steady state of the initial boundary value problem. Vice versa, a steady state solution of (2.9) solves (2.5), too.

**Example 2.10** (Reaction-Diffusion Equation). As an example for an initial boundary value problem we take the differential operator as the negative Laplacian operator  $L := -\Delta$  and choose a Dirichlet type boundary condition. The resulting problem is known as a reaction-diffusion system<sup>6</sup>

$$\begin{aligned} \frac{\partial u(x, t)}{\partial t} &= \Delta u(x, t) + f(u(x, t)), & x \in \Omega, t \in \mathbb{R}^+, \\ u(x, 0) &= 0, & x \in \bar{\Omega}, \\ u(x, t) &= 0, & x \in \partial\Omega, t \in \mathbb{R}^+. \end{aligned} \quad (2.10)$$

For a steady state the initial boundary value problem simplifies to a boundary value problem which is the nonlinear Poisson equation,

$$\begin{aligned} \Delta u(x) &= -f(u(x)), & x \in \Omega, \\ u(x) &= 0, & x \in \partial\Omega. \end{aligned}$$

We will continue this example in the following section.

<sup>5</sup>This modification can be interpreted as the addition of the identity function which is – when considered in a discrete setting – equal to a shift of the eigenvalues.

<sup>6</sup>For the interested reader we note that the system has a unique solution (in a weak sense) provided that  $f$  is Lipschitz continuous and  $\partial\Omega$  is smooth (EVANS, 1998).



To solve a differential equation as arising in a boundary value problem numerically, numerous methods are known, for instance the *finite difference method* (FDM), the *finite element method* (FEM), the *boundary element method* (BEM), and the *finite volume method* (FVM).

The FDM and the FEM are the most popular methods, sometimes used together as a hybrid. The FDM dominated the early development of numerical analysis of partial differential equations, cf. (LARSSON & THOMÉE, 2003), and is still often used if the problem is defined on a simple (e.g. rectangular or cylindrical) geometry. A substitution of derivatives by difference quotients reduces the differential equation problem to a finite linear system of algebraic equations. Assembled in matrix-vector form, the resulting matrix is typically sparse and highly structured. However, the FDM shows disadvantages for complex geometries. In such cases, the FEM is preferred since here the domain discretisation is more flexible. The range of application of the BEM includes problems with partially unbounded domains. It is based on a reformulation of the differential equation as an integral equation over the boundary of the domain. This equation can be used for the numerical approximation which typically yields a system of equations which is small but neither sparse nor symmetric. In general, the BEM is more restricted compared to FDM and FEM. Finally, the FVM is used if the differential equation is based on a conservation law. Its application range lies mainly in the field of computational fluid dynamics.

In the context of image registration we are concerned with a simple geometry as domain, namely a  $d$ -dimensional cuboid. Since, moreover, a digital image consists of voxels which are all of identical size, a FDM turns out to be the natural choice to solve the differential equation arising in this thesis numerically.

## 2.5 Finite Differences

As sketched in Section 2.3, the non-parametric registration approach is given by a minimisation problem which can be solved numerically by determining its Gâteaux derivative. In addition, in the previous section it has been shown that the resulting system of (partial) differential equations can be embedded into an initial boundary value problem.

For a numerical solution of an initial boundary value problem we employ the finite difference method and start with a discretisation of the domain and the time axis. By replacing the differential operator by difference quotients we arrive at a discretised initial boundary value problem consisting of a discrete equation with respect to each point of the discretised domain.

For clarity we restrict the notation to the case of the unit square  $\Omega = (0, 1)^2$  with the origin in the upper left corner. The first coordinate,  $x_1$  is assumed in vertical direction, the second one,  $x_2$ , in horizontal direction.

### 2.5.1 Domain Discretisation

For the discretisation of  $\bar{\Omega}$  by an equispaced grid consisting of  $r \times s$  grid points, let  $h := (h_1, h_2) := ((r - 1)^{-1}, (s - 1)^{-1})$  collect the grid spacings in each

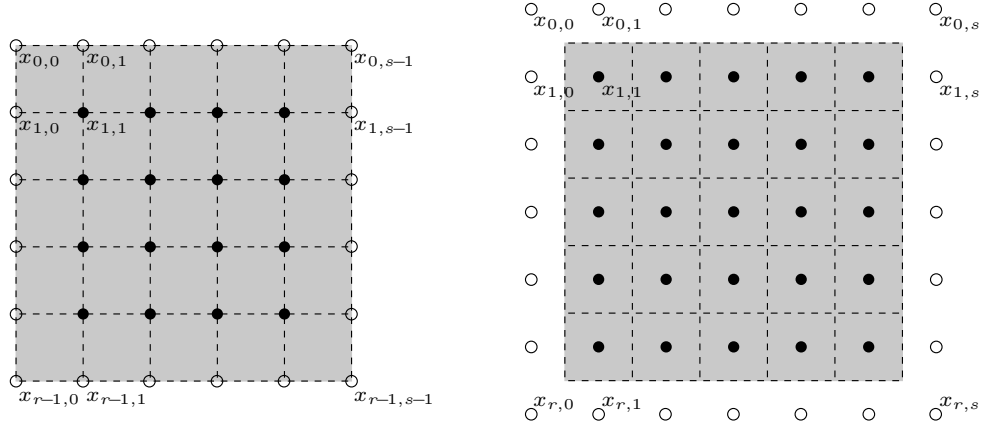


Figure 2.4: Schematic visualisation of an edge-point (left) and a mid-point discretisation (right). Filled circles indicate grid points within the domain  $\Omega$ , empty circles represent grid points on  $\partial\Omega$  in the edge-point case and so-called ghost points outside  $\bar{\Omega}$  in the mid-point case.

coordinate.<sup>7</sup> Then, a so-called *edge-point* discretisation arises,

$$\begin{aligned}\Omega_h^{\text{edge}} &:= \{x_{i,j} = (ih_1, jh_2) \mid i = 1, \dots, r-2, j = 1, \dots, s-2\}, \\ \partial\Omega_h^{\text{edge}} &:= \{x_{i,j} = (ih_1, jh_2) \mid i = 0, \dots, r-1, j = 0, \dots, s-1\} \setminus \Omega_h^{\text{edge}}.\end{aligned}\tag{2.11}$$

Note that all points of  $\partial\Omega_h^{\text{edge}}$  are included in  $\partial\Omega$ .

Alternatively, a so-called *mid-point* discretisation is given by

$$\begin{aligned}\Omega_h^{\text{mid}} &:= \{x_{i,j} = ((i - \frac{1}{2})h_1, (j - \frac{1}{2})h_2) \mid i = 1, \dots, r-1, j = 1, \dots, s-1\}, \\ \partial\Omega_h^{\text{mid}} &:= \{x_{i,j} = ((i - \frac{1}{2})h_1, (j - \frac{1}{2})h_2) \mid i = 0, \dots, r, j = 0, \dots, s\} \setminus \Omega_h^{\text{mid}}.\end{aligned}\tag{2.12}$$

Note that the grid defined by  $\Omega_h^{\text{mid}}$  contains one additional column/row compared to  $\Omega_h^{\text{edge}}$ . Furthermore, none of the points in  $\partial\Omega_h^{\text{mid}}$  (the so-called ghost points) is included in  $\bar{\Omega}$ .

For an illustration of both types of discretisation we consider an image, say  $I \in \text{Img}(\Omega)$ , and employ a domain discretisation to derive a digital image. As described in Definition 2.3, a digital image is defined on an array of discrete points,  $X$ . Now,  $X$  is given by either  $\Omega_h^{\text{edge}} \cup \partial\Omega_h^{\text{edge}}$  or  $\Omega_h^{\text{mid}} \cup \partial\Omega_h^{\text{mid}}$ . In the case of an edge-point discretisation the grid points are located on the edges of the voxels (cf. Figure 2.4, left) whereas with a mid-point discretisation they are located in the voxel centres of the digital image (right). To express the dependence of a digital image on the grid spacing  $h$ , we attach a subscript and denote it by  $I_h$  in the following.

While the type of grid discretisation is of minor importance for the discretisation of the differential equations occurring in the initial boundary value problem, it

<sup>7</sup>In medical applications such a differentiation is essential at least for three-dimensional data sets. Here, voxels are in general non-isotropic in size.

will turn out to be crucial when discretising its boundary conditions. Nonetheless, we will use the notation  $\Omega_h$  and  $\partial\Omega_h$  instead of  $\Omega_h^{\text{edge}}$ ,  $\Omega_h^{\text{mid}}$ ,  $\partial\Omega_h^{\text{edge}}$ , and  $\partial\Omega_h^{\text{mid}}$  whenever the statement is valid for both types of discretisation.

Likewise, we discretise the time domain similarly to the edge-point discretisation by placing a grid on the temporal axis,  $\{t_l\}_{l \in \mathbb{N}_0}$ , where  $t_l = lk$  and  $k \in \mathbb{R}^+$  denotes the grid spacing.

### 2.5.2 Difference Quotients

Based on the discretisation of  $\Omega$  and the time axis, we will discretise the initial boundary value problem (IBVP) itself. For a moment we denote the IBVP by

$$L^{\text{IBVP}} u = 0 \quad (2.13)$$

and a discretised version of it by

$$L_{h,k}^{\text{IBVP}} U = 0 \quad (2.14)$$

with  $U$  as a pointwise function  $U = (U_1, U_2)^T$  approximating

$$U_n^{i,j,l} \hat{=} u_n(x_{i,j}, t_l), \quad n = 1, 2.$$

Here,  $x_{i,j}$  is chosen accordingly to (2.11) and (2.12) in the edge-point case and in the mid-point case, respectively.

The question arising here is how well the solution  $U$  of the difference equation approximates the solution  $u$  of the boundary value problem. There are various sources for an error  $\|u - U\|$  such as:

- $U$  is computed at certain positions in space yielding a spatial error,
- $U$  is computed at certain positions in time yielding a temporal error, i.e. in general,  $U$  will not solve the corresponding boundary value problem exactly,
- derivatives included in the differential equation are approximated by difference quotients.

By substituting  $u$  into (2.14) and subtracting it from (2.13), the so-called consistency error can be determined,

$$\tau_{h,k} := \max_{i,j,l} |L^{\text{IBVP}} u(x_{i,j}, t_l) - L_{h,k}^{\text{IBVP}} u(x_{i,j}, t_l)|.$$

However, consistency is one piece of information and does not ensure the solution of the difference equation to converge towards the solution of the underlying partial differential equation. The most common method to ensure convergence for difference equations is described by, e.g., THOMAS (1995): The Lax Theorem allows to prove convergence of a difference scheme by showing that the discretisation is consistent with the original problem as well as that the scheme is stable. In this thesis we spend some effort on ensuring consistency as a, roughly spoken, necessary condition for convergence and do not focus on the stability.

**Definition 2.11** (Consistency, Local Order of Accuracy (LOA)). *Given an IBVP and a corresponding discretisation with spatial and temporal grid spacings  $h, k$ , the discretised problem is called consistent with the IBVP if*

$$\tau_{h,k} \rightarrow 0 \quad \text{for } h \rightarrow 0 \quad \text{and } k \rightarrow 0 .$$

*Furthermore, the discretisation has a local order of accuracy<sup>8</sup>  $p$  in space and  $q$  in time, denoted by  $\mathcal{O}(h^p + k^q)$ , if*

$$\tau_{h,k} \leq c_1 h^p + c_2 k^q$$

*with constants  $c_1, c_2$ .*

To replace derivative terms occurring in the IBVP by difference quotients we proceed by approximating derivatives. Note that the overall LOA of a discretised IBVP is the lowest order used in any part of the problem.

For the following considerations we require  $u$  to be four times continuously differentiable in space and twice continuously differentiable in time. Then, an exploitation of Taylor series leads to the following single first order derivatives

$$\begin{aligned} \partial_1^- u_n(x, t) &:= \frac{u_n(x, t) - u_n(x - h_1 e_1, t)}{h_1} \\ &= \partial_{x_1} u_n(x, t) + \mathcal{O}(h_1) , \\ \partial_1^+ u_n(x, t) &:= \frac{u_n(x + h_1 e_1, t) - u_n(x, t)}{h_1} \\ &= \partial_{x_1} u_n(x, t) + \mathcal{O}(h_1) , \\ \partial_1^\pm u_n(x, t) &:= \frac{u_n(x + \frac{h_1}{2} e_1, t) - u_n(x - \frac{h_1}{2} e_1, t)}{h_1} \\ &= \partial_{x_1} u_n(x, t) + \mathcal{O}(h_1^2) , \end{aligned}$$

called backward, forward and central difference quotients, respectively. The difference quotients with respect to the variables  $x_2$  and  $t$  are defined analogously. For second order and mixed derivatives we have for instance

$$\begin{aligned} \partial_{11}^\pm u_n(x, t) &:= \frac{u_n(x - h_1 e_1, t) - 2u_n(x, t) + u_n(x + h_1 e_1, t)}{h_1^2} \\ &= \partial_{x_1 x_1} u_n(x, t) + \mathcal{O}(h_1^2) , \\ \partial_{12}^\pm u_n(x, t) &:= \frac{u_n(x + \frac{h_1}{2} e_1 + \frac{h_2}{2} e_2, t) - u_n(x + \frac{h_1}{2} e_1 - \frac{h_2}{2} e_2, t)}{h_1 h_2} \\ &\quad - \frac{u_n(x - \frac{h_1}{2} e_1 + \frac{h_2}{2} e_2, t) - u_n(x - \frac{h_1}{2} e_1 - \frac{h_2}{2} e_2, t)}{h_1 h_2} \\ &= \partial_{x_1 x_2} u_n(x, t) + \mathcal{O}(h_1^2 + h_2^2) , \end{aligned}$$

---

<sup>8</sup>Note that the order depends on the chosen norm which is the  $l^\infty$ -norm. For simplicity, we assumed an isotropic grid spacing, i.e.  $h_1 = h_2 =: h$

which are both defined using central differences. In addition we define an averaging quotient, here for instance with respect to  $x_1$ ,

$$\begin{aligned}\partial_1^a u_n(x, t) &:= \frac{u_n(x - \frac{h_1}{2} e_1, t) + u_n(x + \frac{h_1}{2} e_1, t)}{2} \\ &= u_n(x, t) + \mathcal{O}(h_1^2),\end{aligned}$$

where the equality follows again by Taylor's Theorem.

These quotients will now be applied to the approximation  $U$ . According to the discretisation scheme we choose  $(x, t) = (x_{i,j}, t_l) \in \Omega_h$  and obtain

$$\begin{aligned}\partial_1^- U_n^{i,j,l} &= \frac{U_n^{i,j,l} - U_n^{i-1,j,l}}{h_1}, \\ \partial_1^+ U_n^{i,j,l} &= \frac{U_n^{i+1,j,l} - U_n^{i,j,l}}{h_1}, \\ \partial_1^\pm U_n^{i,j,l} &= \frac{U_n^{i+\frac{1}{2},j,l} - U_n^{i-\frac{1}{2},j,l}}{h_1}, \\ \partial_{11}^\pm U_n^{i,j,l} &= \frac{U_n^{i-1,j,l} - 2U_n^{i,j,l} + U_n^{i+1,j,l}}{h_1^2}, \\ \partial_{12}^\pm U_n^{i,j,l} &= \frac{U_n^{i+\frac{1}{2},j+\frac{1}{2},l} - U_n^{i+\frac{1}{2},j-\frac{1}{2},l} - U_n^{i-\frac{1}{2},j+\frac{1}{2},l} + U_n^{i-\frac{1}{2},j-\frac{1}{2},l}}{h_1 h_2}, \\ \partial_1^a U_n^{i,j,l} &= \frac{U_n^{i-\frac{1}{2},j,l} + U_n^{i+\frac{1}{2},j,l}}{2}.\end{aligned}\tag{2.15}$$

for all  $l \in \mathbb{N}_0$  and  $n \in \{1, 2\}$ .

Now, the differential equations included in the IBVP can be discretised. For each grid point a discrete equation in terms of  $U$  can be formulated,

$$\begin{pmatrix} \partial_t^- U_1^{i,j,l+1} \\ \partial_t^- U_2^{i,j,l+1} \end{pmatrix} = -L_h \begin{pmatrix} U_1^{i,j,l+1} \\ U_2^{i,j,l+1} \end{pmatrix} + f_h \begin{pmatrix} U_1^{i,j,l+1} \\ U_2^{i,j,l+1} \end{pmatrix}, \quad \begin{matrix} (i,j) \in \Omega_h \\ l \in \mathbb{N}_0 \end{matrix}.$$

Here,  $L_h$  and  $f_h$  denote  $2 \times 2$ -matrices of difference quotients which result from the derivative operators included in  $L$  and  $f$ , respectively.

With  $U^{i,j,l} := (U_1^{i,j,l}, U_2^{i,j,l})^\top$  a reformulation yields

$$(\text{id}_h + kL_h)U^{i,j,l+1} = U^{i,j,l} + kf_h U^{i,j,l+1}, \quad (i,j) \in \Omega_h, \quad l \in \mathbb{N}_0. \tag{2.16}$$

Care has to be taken when  $x_{i,j}$  has a neighbouring grid point which belongs to the boundary  $\partial\Omega_h$ . In such a case a difference quotient for  $U_n^{i,j,l}$  typically includes function values on the boundary and (2.16) provides  $\#\Omega_h$  equations for  $\#(\Omega_h \cup \partial\Omega_h)$  unknowns. Further equations will result from the discretisation of the boundary conditions included in the IBVP. Here, we consider the two types of boundary conditions defined in (2.4) and consider, without loss of generality, the edge  $\partial\Omega|_{x_2=0}$  only.

- Let  $B = \text{id}$ , i.e. the boundary condition reads  $u(x) = 0$  on  $\partial\Omega$ .
  - If an edge-point discretisation is employed, the boundary condition can be directly transformed into a condition for  $U$ , i.e.

$$U_n^{i,0,l} = 0, \quad i = 0, \dots, r-1, \quad l \in \mathbb{N}_0, \quad n = 1, 2.$$

- If, in contrast, a mid-point discretisation is employed,  $\partial\Omega_h^{\text{mid}}$  is not a subset of  $\partial\Omega$  and we identify  $x_{i,\frac{1}{2}}$  as a point on  $\partial\Omega$ . Here, an averaging yields

$$\partial_2^a U_n^{i,\frac{1}{2},l} = 0 \quad \Leftrightarrow \quad U_n^{i,0,l} = -U_n^{i,1,l}$$

for  $i = 0, \dots, r, \quad l \in \mathbb{N}_0$ , and  $n = 1, 2$ .

Therefore, this kind of boundary condition can be exactly described by an edge-point discretisation and approximated with second-order accuracy by a mid-point discretisation. Choosing the former we define

$$B_h := \begin{pmatrix} 1 & 0 \\ 0 & 1 \end{pmatrix} \quad (2.17)$$

yielding

$$B_h(U_1^{i,j,l}, U_2^{i,j,l})^\top = 0 \quad \Leftrightarrow \quad U_n^{i,j,l} = 0, \quad (i, j) \in \partial\Omega_h^{\text{edge}}, \quad n = 1, 2. \quad (2.18)$$

- Let  $B = \frac{\partial}{\partial \mathbf{n}}$ , i.e. the boundary condition reads  $\frac{\partial u}{\partial \mathbf{n}} = 0$  on  $\partial\Omega$ , or, with respect to the considered edge,  $\frac{\partial u}{\partial y} = 0$  on  $\partial\Omega|_{x_2=0}$ .

- Here, an edge-point discretisation leads to the one-sided approximation

$$\partial_2^+ U_n^{i,0,l} = \frac{U_n^{i,1,l} - U_n^{i,0,l}}{h_2} = 0 \quad \Rightarrow \quad U_n^{i,0,l} = U_n^{i,1,l}$$

for  $i = 0, \dots, r-1, \quad l \in \mathbb{N}_0$ , and  $n = 1, 2$ . Note that by employing a central difference quotient a representation of  $U_n^{i,0,l}$  cannot be achieved.

- In contrast, a mid-point discretisation allows for an approximation by central differences. Again, we consider a point  $x_{i,\frac{1}{2}}$  and derive

$$\partial_2^\pm U_n^{i,\frac{1}{2},l} = \frac{U_n^{i,1,l} - U_n^{i,0,l}}{h_2} = 0 \quad \Rightarrow \quad U_n^{i,0,l} = U_n^{i,1,l}$$

for  $i = 0, \dots, r, \quad l \in \mathbb{N}_0$ , and  $n = 1, 2$ .

Although at first sight, the representations of  $U_n^{i,0,l}$  look the same for both types of discretisation, they differ due to the different position of  $U_n^{i,0,l}$  (located on the boundary in the edge-point case but with a distance of  $h_2/2$  outside of the boundary in the mid-point case, cf. Figure 2.4).

Consequently, this kind of boundary condition can be approximated with first-order accuracy by an edge-point discretisation and with second-order accuracy by a mid-point discretisation. Choosing the latter we define

$$B_h := \begin{pmatrix} \partial^* & 0 \\ 0 & \partial^* \end{pmatrix} \quad (2.19)$$

with  $\partial^*$  a difference quotient such that

$$B_h(U_1^{i,j,l}, U_2^{i,j,l})^\top = 0 \quad \Leftrightarrow \quad U_n^{i,j,l} = U_n^{\hat{i},\hat{j},l}, \quad (i,j) \in \partial\Omega_h^{\text{mid}}, \quad n = 1, 2, \quad (2.20)$$

where  $(\hat{i}, \hat{j})$  denotes the, with regard to  $\partial\Omega$ , mirrored position to  $(i, j)$ .

Finally, the initial condition of the IBVP shall be discretised. This task is trivial and consists of a pointwise evaluation of  $u^{(0)}$  with respect to the chosen type of discretisation, i.e.

$$U_n^{i,j,0} = u_n^{(0)}(x_i, y_j), \quad (i, j) \in \bar{\Omega}_h, \quad n = 1, 2. \quad (2.21)$$

The discretisation of the IBVP (2.9) is completed now. In summary, it consists of

- the discretised differential equation (2.16),
- the discretised initial condition (2.21),
- and the discretised boundary condition (2.18) or (2.20).

By choosing appropriate difference quotients from (2.15) an overall LOA of  $\mathcal{O}(h^2 + k)$  can be achieved. With regard to the discretised differential equation (2.16) we observe the time level of its last term  $f_h U^{i,j,l+1}$  to differ from the one in the time-marching approach<sup>9</sup> (2.8),  $f(u^{(l)}(x))$ . However, replacing  $f_h U^{i,j,l+1}$  by  $f_h U^{i,j,l}$  in (2.16) does not change the temporal LOA of the discretisation of the IBVP as shown by the following lemma.

**Lemma 2.12.** *Given the IBVP as in (2.9) and a discretised version*

$$\begin{aligned} (\text{id}_h + kL_h)U^{i,j,l+1} &= U^{i,j,l} + kf_h U^{i,j,l}, & (i,j) \in \Omega_h, \quad l \in \mathbb{N}_0, \\ U^{i,j,0} &= u^{(0)}(x_i, y_j), & (i,j) \in \bar{\Omega}_h, \\ B_h U^{i,j,l+1} &= 0, & (i,j) \in \partial\Omega_h, \quad l \in \mathbb{N}_0, \end{aligned} \quad (2.22)$$

with  $L_h$ ,  $f_h$ , and  $B_h$  as (at least) second-order approximations to  $L$ ,  $f$ , and  $B$ , respectively, the discretised problem has a LOA of  $\mathcal{O}(h^2 + k)$ .

*Proof.* We start with the differential equation of the IBVP. By employing a forward difference in time with respect to the  $l$ -th time level and a backward

---

<sup>9</sup>Recall that the time-marching approach served as the motivation for the investigation of an IBVP instead of a BVP.

one with respect to the  $l + 1$ -th time level we are faced with approximations which are both of first order in time,

$$\begin{aligned}\partial_t^- U^{i,j,l+1} &= -[L_h U^{i,j,l+1} - f_h U^{i,j,l+1}] , \\ \partial_t^+ U^{i,j,l} &= -[L_h U^{i,j,l} - f_h U^{i,j,l}] .\end{aligned}$$

Summing up we have, by Taylor's Theorem,

$$\begin{aligned}\frac{U^{i,j,l+1} - U^{i,j,l}}{k} &= -L_h \frac{U^{i,j,l+1} + U^{i,j,l}}{2} + f_h \frac{U^{i,j,l} + U^{i,j,l+1}}{2} \\ &= -L_h [U^{i,j,l+1} + \mathcal{O}(k)] + f_h [U^{i,j,l} + \mathcal{O}(k)] ,\end{aligned}$$

which is equivalent to the assumption. Furthermore, since the discretised boundary conditions (2.17) and (2.19) are of, at least, second-order accuracy, the overall LOA of the discretised IBVP is  $\mathcal{O}(h^2 + k)$ . ■

As an example for a discretised IBVP we revisit Example 2.10 and consider it in two dimensions.

**Example 2.13** (Reaction-Diffusion Equation Revisited). For a discretisation of (2.10) we choose the type of discretisation first. Since the boundary condition is of Dirichlet type, an edge-point discretisation is used for the spatial domain. We assume the grid spacing  $h$  to be isotropic, i.e.  $h_1 = h_2 =: h$ . Replacing the derivative terms in (2.10) by difference quotients from (2.15) and (2.18), and applying Lemma 2.12 we end up with a discretisation of the reaction-diffusion system

$$\begin{aligned}(\text{id}_h + kL_h)U^{i,j,l+1} &= U^{i,j,l} + kf_h U^{i,j,l} , & (i,j) \in \Omega_h , \ l \in \mathbb{N}_0 , \\ U^{i,j,0} &= 0 , & (i,j) \in \bar{\Omega}_h , \\ B_h U^{i,j,l+1} &= 0 , & (i,j) \in \partial\Omega_h , \ l \in \mathbb{N}_0 ,\end{aligned}\tag{2.23}$$

with

$$L_h := -\frac{1}{h^2} \begin{pmatrix} \partial_{11}^\pm + \partial_{22}^\pm & 0 \\ 0 & \partial_{11}^\pm + \partial_{22}^\pm \end{pmatrix} \tag{2.24}$$

being of second-order accuracy in space and first-order in time.

Having determined the discretisation of an IBVP, usually the next steps are

1. to assemble for each time step  $l$  the set of difference equations into a system of matrix-vector type,
2. to incorporate the discretised boundary conditions, and,
3. by starting with the discretised initial condition, to iteratively solve the assembled system for the discrete function  $U$ .

To investigate the properties of the assembled system, the distribution of eigenvalues and in particular the symmetry of the system matrix are of great interest.



However, to establish the matrix symmetry is a rather technical task. Moreover, the size of the matrix prevents its specification in a readable full form and, last but not least, an element-wise depiction is little descriptive. As an alternative, we will employ the stencil notation (as described by TROTTENBERG ET AL. (2001) for instance) and link it to the discretised operator as well as to the system matrix as visualised by the scheme

$$\text{discretised operator } \text{id}_h + kL_h \Rightarrow \text{stencil notation} \Rightarrow \text{system matrix} .$$

Then, with regard to the steps formulated above, the scope of the remaining chapter comprises:

- the formulation of discrete equations as in (2.22) but in stencil notation from which a linear system of equations can be assembled,
- the incorporation of discretised boundary conditions,
- the proof of symmetry of the assembled system matrix provided the underlying stencil is symmetric (which is easy to establish),
- and the solution of the assembled system.

### 2.5.3 Stencil Notation

In order to introduce the stencil notation in two dimensions we start by defining a  $3 \times 3$ -matrix of discrete values around a centre  $U_n^{i,j,l}$ ,

$$G(U_n^{i,j,l}) := (g_n^{i,j,l})_{-1 \leq i,j \leq 1} := \begin{bmatrix} U_n^{i-1,j-1,l} & U_n^{i-1,j,l} & U_n^{i-1,j+1,l} \\ U_n^{i,j-1,l} & U_n^{i,j,l} & U_n^{i,j+1,l} \\ U_n^{i+1,j-1,l} & U_n^{i+1,j,l} & U_n^{i+1,j+1,l} \end{bmatrix} .$$

Now, each of the spatial difference quotients from (2.15) can be described alternatively by convolving  $G(U_n^{i,j,l})$  with an appropriate matrix of coefficients, called the stencil.

**Definition 2.14** (Stencil). *A stencil (of size 1) is given by a matrix  $S$  with entries  $s^{\kappa_1, \kappa_2}$ ,  $\kappa_1, \kappa_2 \in \{-1, 0, 1\}$ , such that*

$$S := \begin{bmatrix} s^{-1,-1} & s^{-1,0} & s^{-1,1} \\ s^{0,-1} & s^{0,0} & s^{0,1} \\ s^{1,-1} & s^{1,0} & s^{1,1} \end{bmatrix} .$$

Then the convolution of  $G(U_n^{i,j,l})$  with a stencil is given by

$$S * G(U_n^{i,j,l}) = \sum_{\kappa_1, \kappa_2 = -1}^1 s^{\kappa_1, \kappa_2} g_n^{\kappa_1, \kappa_2, l} , \quad (2.25)$$

where  $*$  is interpreted as a discrete convolution operator, see, e.g., (TROTTENBERG ET AL., 2001).

**Example 2.15.** As an example we consider the mixed-derivatives operator in (2.15) and assume an isotropic grid spacing, i.e.  $h_1 = h_2 =: h$ ,

$$\partial_1^a \partial_2^a \partial_{12}^\pm U_n^{i,j,l} = S * G(U_n^{i,j,l}) \quad \text{with} \quad S := \frac{1}{4h^2} \begin{bmatrix} 1 & 0 & -1 \\ 0 & 0 & 0 \\ -1 & 0 & 1 \end{bmatrix}.$$

Note that without applying the averaging quotients  $\partial_1^a \partial_2^a$  to  $\partial_{12}^\pm$  we would have ended up with inter-grid positions.

For the case of a matrix of difference quotients as, for instance, in (2.24), we define a block stencil.

**Definition 2.16** (Block Stencil). *A block stencil  $\mathbb{S}$  (of size 2) is given by a  $2 \times 2$  matrix of stencils  $S_{\omega_1, \omega_2}$  with  $\omega_1, \omega_2 \in \{1, 2\}$ .*

The convolution for a block stencil is then defined by a componentwise convolution,

$$\begin{pmatrix} S_{1,1} & S_{1,2} \\ S_{2,1} & S_{2,2} \end{pmatrix} * \begin{pmatrix} G(U_1^{i,j,l}) & G(U_2^{i,j,l}) \\ G(U_1^{i,j,l}) & G(U_2^{i,j,l}) \end{pmatrix} := \begin{pmatrix} S_{1,1} * G(U_1^{i,j,l}) & S_{1,2} * G(U_2^{i,j,l}) \\ S_{2,1} * G(U_1^{i,j,l}) & S_{2,2} * G(U_2^{i,j,l}) \end{pmatrix}$$

An important property of great utility later on concerns the symmetry of a (block) stencil. This requires the definition of the transpose of a stencil.

**Definition 2.17** (Transpose of a Stencil). *Given stencils  $S_1$  and  $S_2$  with entries  $s_1^{\kappa_1, \kappa_2}$  and  $s_2^{\kappa_1, \kappa_2}$ ,  $\kappa_1, \kappa_2 \in \{-1, 0, 1\}$ ,  $S_2$  is transposed to  $S_1$  if*

$$s_1^{\kappa_1, \kappa_2} = s_2^{-\kappa_1, -\kappa_2}, \quad \kappa_1, \kappa_2 \in \{-1, 0, 1\}. \quad (2.26)$$

We denote the transpose of a stencil by  $\mathsf{T}$ , i.e.  $S_1 = S_2^\mathsf{T} = (S_2^\mathsf{T})^\mathsf{T}$ .

**Definition 2.18** (Symmetric Stencil, Block-Symmetric Block Stencil). *Given a stencil  $S$  with entries  $s^{\kappa_1, \kappa_2}$ ,  $\kappa_1, \kappa_2 \in \{-1, 0, 1\}$ ,  $S$  is called symmetric if it is equal to its transpose, i.e., if  $S = S^\mathsf{T}$ .*

*Furthermore, a block stencil  $\mathbb{S} = (S_{\omega_1, \omega_2})_{\omega_1, \omega_2}$  is called block-symmetric if*

- each stencil  $S_{\omega_1, \omega_1} \in \mathbb{S}$  is symmetric, and
- each stencil  $S_{\omega_1, \omega_2} \in \mathbb{S}$ ,  $\omega_1 \neq \omega_2$ , is equal to  $S_{\omega_2, \omega_1}^\mathsf{T}$ .

Note that the conditions for block-symmetry are equivalent to the single condition

$$S_{\omega_1, \omega_2} = S_{\omega_2, \omega_1}^\mathsf{T}$$

to hold for all  $\omega_1, \omega_2 \in \{1, 2\}$ .

**Example 2.19** (Reaction-Diffusion Equation Revisited). The discretised operator  $\text{id}_h + kL_h$  in (2.23),

$$\begin{pmatrix} 1 & 0 \\ 0 & 1 \end{pmatrix} - \frac{k}{h^2} \begin{pmatrix} \partial_{11}^\pm + \partial_{22}^\pm & 0 \\ 0 & \partial_{11}^\pm + \partial_{22}^\pm \end{pmatrix}$$

can be described by the block stencil

$$\mathbb{S} = \left( \begin{array}{c} \begin{bmatrix} 0 & 0 & 0 \\ 0 & 1 & 0 \\ 0 & 0 & 0 \end{bmatrix} \\ \begin{bmatrix} 0 & 0 & 0 \\ 0 & 1 & 0 \\ 0 & 0 & 0 \end{bmatrix} \end{array} \right) - \frac{k}{h^2} \left( \begin{array}{c} \begin{bmatrix} 0 & 1 & 0 \\ 1 & -4 & 1 \\ 0 & 1 & 0 \end{bmatrix} \\ \begin{bmatrix} 0 & 1 & 0 \\ 1 & -4 & 1 \\ 0 & 1 & 0 \end{bmatrix} \end{array} \right).$$

It is easy to verify that  $\mathbb{S}$  is block-symmetric.

For the stencil notation introduced so far, boundary conditions have been disregarded. However, if the convolution in (2.25) is applied to a grid point for which a neighbouring grid point belongs to  $\partial\Omega_h$ , boundary conditions apply.

We recall the equivalences (2.18) and (2.20) for a Dirichlet and a Neumann boundary condition, respectively, and consider without loss of generality a grid point  $(i, j)$  with a neighbouring grid point belonging to  $\partial\Omega|_{x_2=0}$  and with no neighbouring grid point belonging to  $\partial\Omega|_{x_1=0}$  (i.e. a left edge of  $\Omega$ ). Then the specific stencil for the grid point  $(i, j)$  changes to so-called *boundary stencils*

$$\begin{bmatrix} s^{-1,0} & s^{-1,1} \\ s^{0,0} & s^{0,1} \\ s^{1,0} & s^{1,1} \end{bmatrix} \quad \text{and} \quad \begin{bmatrix} s^{-1,0} & s^{-1,1} \\ s^{0,0} + \sum_{i=-1}^1 s^{i,-1} & s^{0,1} \\ s^{1,0} & s^{1,1} \end{bmatrix} \quad (2.27)$$

in the case of a Dirichlet condition and a Neumann condition, respectively.

The stencil symmetry in both cases is not affected by the changes, since the condition (2.26) is only applied for those  $(\kappa_1, \kappa_2)$  for which a stencil entry at the position  $(-\kappa_1, -\kappa_2)$  exists and since the central entry in the Neumann case is symmetric to itself. Moreover, the block-symmetry condition is not affected since a boundary condition acts on all stencils of a block stencil simultaneously.

#### 2.5.4 Assembling

By use of the stencil notation a system of discrete equations as in (2.22) can be reformulated with a block stencil. The next step will be to assemble a linear system of equations of matrix-vector type,

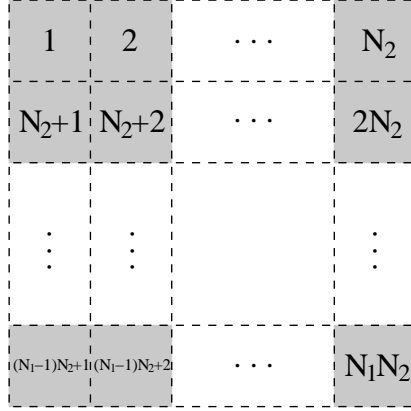
$$\mathbf{A}\mathbf{U}^{(l+1)} = \mathbf{U}^{(l)} + k\mathbf{F}^{(l)}, \quad l \in \mathbb{N}^0,$$

and to include the discretised boundary conditions from (2.22). Finally, this system will be solved for  $\mathbf{U}^{(l+1)}$ . Assuming  $\Omega_h$  consists of  $N_1 \times N_2$  grid points, the system is of size  $2N_1N_2$ . We make use of the abbreviation

$$\mathbb{N}_{\leq c} := \{i \in \mathbb{N} : i \leq c\}$$

and denote a block matrix

$$\mathbf{A} = \begin{pmatrix} \mathbf{A}_{1,1} & \mathbf{A}_{1,2} \\ \mathbf{A}_{2,1} & \mathbf{A}_{2,2} \end{pmatrix} \quad \text{with each matrix } \mathbf{A}_{\omega_1, \omega_2} = (\mathbf{a}_{\omega_1, \omega_2}^{i,j})_{i,j \in \mathbb{N}_{\leq N_1 N_2}}$$

Figure 2.5: Visualisation of the grid point mapping  $\xi$ .

taking – following an order to be specified – the coefficients from the block stencil and thus from the discrete operator  $\text{id}_h + kL_h$ . Furthermore,  $\mathbf{U}^{(l)}$  and  $\mathbf{F}^{(l)}$  denote vectors which include, following the same order, all values  $U^{i,j,l}$  and  $f_h U^{i,j,l}$ , respectively.

With the assembly of the system in mind we specify the order by the component-specific mapping

$$\xi : \mathbb{N}_{\leq N_1} \times \mathbb{N}_{\leq N_2} \rightarrow \mathbb{N}_{\leq N_1 N_2}, \quad \xi(i, j) = (i - 1)N_2 + j \quad (2.28)$$

returning to each grid point  $(i, j)$  a number less or equal than  $N_1 N_2$  (see Figure 2.5 for a visualisation of the arrangement). Then,  $\mathbf{U}^{(l)}$  and  $\mathbf{F}^{(l)}$  are given by

$$\begin{aligned} \mathbf{U}^{(l)} &:= (U_1^{1,1,l}, \dots, U_1^{1,N_2,l}, \dots, U_1^{N_1,1,l}, \dots, U_1^{N_1,N_2,l}, \\ &\quad U_2^{1,1,l}, \dots, U_2^{1,N_2,l}, \dots, U_2^{N_1,1,l}, \dots, U_2^{N_1,N_2,l})^\top, \\ \mathbf{F}^{(l)} &:= ((f_h U^{1,1,l})_1, \dots, (f_h U^{1,N_2,l})_1, \dots, (f_h U^{N_1,1,l})_1, \dots, (f_h U^{N_1,N_2,l})_1, \\ &\quad (f_h U^{1,1,l})_2, \dots, (f_h U^{1,N_2,l})_2, \dots, (f_h U^{N_1,1,l})_2, \dots, (f_h U^{N_1,N_2,l})_2)^\top, \end{aligned}$$

and for each stencil  $S_{\omega_1, \omega_2} \in \mathbb{S}$  the corresponding matrix  $\mathbf{A}_{\omega_1, \omega_2}$  can be constructed. To this end let  $i \in \mathbb{N}_{\leq N_1}$ ,  $j \in \mathbb{N}_{\leq N_2}$ . By choosing  $\kappa_1, \kappa_2 \in \{-1, 0, 1\}$  provided that  $i + \kappa_1 \in \mathbb{N}_{\leq N_1}$  and  $j + \kappa_2 \in \mathbb{N}_{\leq N_2}$  we ensure that  $(i + \kappa_1, j + \kappa_2)$  do not refer to values outside  $\Omega_h$ . Each non-zero entry of  $\mathbf{A}_{\omega_1, \omega_2}$  is then defined by

$$\mathbf{a}_{\omega_1, \omega_2}^{\xi(i,j), \xi(i+\kappa_1, j+\kappa_2)} := s_{\omega_1, \omega_2}^{\kappa_1, \kappa_2}. \quad (2.29)$$

Note that all entries belonging to the boundary  $\partial\Omega_h$  are zero. Thus, a boundary stencil with an incorporated Dirichlet condition as in (2.27, left) is automatically included<sup>10</sup>. In contrast, the incorporation of a boundary stencil for a Neumann type condition as in (2.27, right) requires an update of those diagonal elements for which  $i \in \{1, N_1\}$  or  $j \in \{1, N_2\}$ . Dependent on  $i$  and  $j$ , eight cases can be distinguished:

<sup>10</sup>Since both boundary conditions used in this thesis are zero-conditions,  $\mathbf{F}^{(l)}$  does not need to be updated.

1. upper left corner, i.e.  $i = 1, j = 1$ ,

$$\mathbf{a}_{\omega_1, \omega_2}^{\xi(1,1), \xi(1,1)} := s_{\omega_1, \omega_2}^{0,0} + s_{\omega_1, \omega_2}^{1,-1} + s_{\omega_1, \omega_2}^{0,-1} + s_{\omega_1, \omega_2}^{-1,-1} + s_{\omega_1, \omega_2}^{-1,0} + s_{\omega_1, \omega_2}^{-1,1} ,$$

2. upper edge, i.e.  $i = 1, j \notin \{1, N_2\}$ ,

$$\mathbf{a}_{\omega_1, \omega_2}^{\xi(1,j), \xi(1,j)} := s_{\omega_1, \omega_2}^{0,0} + s_{\omega_1, \omega_2}^{-1,-1} + s_{\omega_1, \omega_2}^{-1,0} + s_{\omega_1, \omega_2}^{-1,1} ,$$

3. upper right corner, i.e.  $i = 1, j = N_2$ ,

$$\mathbf{a}_{\omega_1, \omega_2}^{\xi(1,N_2), \xi(1,N_2)} := s_{\omega_1, \omega_2}^{0,0} + s_{\omega_1, \omega_2}^{-1,-1} + s_{\omega_1, \omega_2}^{-1,0} + s_{\omega_1, \omega_2}^{-1,1} + s_{\omega_1, \omega_2}^{0,1} + s_{\omega_1, \omega_2}^{1,1} ,$$

4. right edge, i.e.  $i \notin \{1, N_1\}, j = N_2$ ,

$$\mathbf{a}_{\omega_1, \omega_2}^{\xi(i,N_2), \xi(i,N_2)} := s_{\omega_1, \omega_2}^{0,0} + s_{\omega_1, \omega_2}^{-1,1} + s_{\omega_1, \omega_2}^{0,1} + s_{\omega_1, \omega_2}^{1,1} ,$$

5. lower right corner, i.e.  $i = N_1, j = N_2$ ,

$$\mathbf{a}_{\omega_1, \omega_2}^{\xi(N_1,N_2), \xi(N_1,N_2)} := s_{\omega_1, \omega_2}^{0,0} + s_{\omega_1, \omega_2}^{-1,1} + s_{\omega_1, \omega_2}^{0,1} + s_{\omega_1, \omega_2}^{1,1} + s_{\omega_1, \omega_2}^{1,0} + s_{\omega_1, \omega_2}^{1,-1} ,$$

6. lower edge, i.e.  $i = N_1, j \notin \{1, N_2\}$ ,

$$\mathbf{a}_{\omega_1, \omega_2}^{\xi(N_1,j), \xi(N_1,j)} := s_{\omega_1, \omega_2}^{0,0} + s_{\omega_1, \omega_2}^{1,1} + s_{\omega_1, \omega_2}^{1,0} + s_{\omega_1, \omega_2}^{1,-1} ,$$

7. lower left corner, i.e.  $i = N_1, j = 1$ ,

$$\mathbf{a}_{\omega_1, \omega_2}^{\xi(N_1,1), \xi(N_1,1)} := s_{\omega_1, \omega_2}^{0,0} + s_{\omega_1, \omega_2}^{1,1} + s_{\omega_1, \omega_2}^{1,0} + s_{\omega_1, \omega_2}^{1,-1} + s_{\omega_1, \omega_2}^{0,-1} + s_{\omega_1, \omega_2}^{-1,-1} ,$$

8. left edge, i.e.  $i \notin \{1, N_1\}, j = 1$ ,

$$\mathbf{a}_{\omega_1, \omega_2}^{\xi(i,1), \xi(i,1)} := s_{\omega_1, \omega_2}^{0,0} + s_{\omega_1, \omega_2}^{1,-1} + s_{\omega_1, \omega_2}^{0,-1} + s_{\omega_1, \omega_2}^{-1,-1} .$$

Due to the symmetry of the stencil  $S_{\omega_1, \omega_2}$  the cases (1) and (5), (2) and (6), (3) and (7) as well as (4) and (8) coincide and we are left with

$$\mathbf{a}_{\omega_1, \omega_2}^{\xi(i,j), \xi(i,j)} := \begin{cases} \sum_{\kappa_1 + \kappa_2 \leq 0} s_{\omega_1, \omega_2}^{\kappa_1, \kappa_2} & , (i, j) \in \{(1, 1), (N_1, N_2)\} \\ \sum_{\kappa_2 = -1}^1 s_{\omega_1, \omega_2}^{1, \kappa_2} + s_{\omega_1, \omega_2}^{0,0} & , i \in \{1, N_1\}, j \notin \{1, N_2\} \\ \sum_{\kappa_2 \geq \kappa_1} s_{\omega_1, \omega_2}^{\kappa_1, \kappa_2} & , (i, j) \in \{(1, N_2), (N_1, 1)\} \\ \sum_{\kappa_1 = -1}^1 s_{\omega_1, \omega_2}^{\kappa_1, 1} + s_{\omega_1, \omega_2}^{0,0} & , i \notin \{1, N_1\}, j \in \{1, N_2\} \end{cases} . \quad (2.30)$$

Summarising, by (2.29) and – in the case of Neumann type conditions – in addition by (2.30), a linear system of equations in matrix-vector form is assembled,

$$\mathbf{A}\mathbf{U}^{(l+1)} = \mathbf{U}^{(l)} + k\mathbf{F}^{(l)} , \quad l \in \mathbb{N}^0 , \quad (2.31)$$

which, together with the discretised initial condition

$$\mathbf{U}^{(0)} = 0 , \quad (2.32)$$

represents the discretised IBVP.

**Remark.** By (2.29) and (2.30) we observe that each row of the matrix  $\mathbf{A}_{\omega_1, \omega_2}$  has at most as many non-zero entries as the corresponding stencil has non-zero entries. Disregarding the updated matrix entries in the Neumann-case, the entries on each diagonal are the same since the stencil does not depend on the grid position.

As mentioned before, for solving the system (2.31), it may be particularly useful to be familiar with its properties. One possible way to ensure the symmetry of the block matrix  $\mathbf{A}$  is to ensure the block-symmetry of the corresponding block stencil as pointed out in the following lemma. To our best knowledge, its proof is not published in the literature yet.

**Lemma 2.20** (Symmetry of the System Matrix  $\mathbf{A}$ ). *Let  $\mathbb{S} = (S_{\omega_1, \omega_2})_{\omega_1, \omega_2}$  denote a block stencil of size 2, let  $\mathbf{A}$  denote a block matrix with matrices  $\mathbf{A}_{\omega_1, \omega_2}$ ,  $\omega_1, \omega_2 \in \{1, 2\}$ , defined via (2.29) in the case of Dirichlet boundary conditions and additionally via (2.30) in the case of Neumann boundary conditions. Then  $\mathbf{A}$  is symmetric if  $\mathbb{S}$  is block-symmetric.*

*Proof.* Let  $\mathbb{S}$  be block-symmetric. Then, following Definition 2.18, the stencils  $S_{1,1}$ ,  $S_{2,2}$  are symmetric and we have  $S_{1,2} = (S_{2,1})^\top$ . We start by showing the symmetry of  $\mathbf{A}_{1,1}$  and  $\mathbf{A}_{2,2}$  and disregard, in the first instance, the boundary stencils.

Let  $i \in \mathbb{N}_{\leq N_1}$ ,  $j \in \mathbb{N}_{\leq N_2}$ . In addition, let  $\kappa_1, \kappa_2 \in \{-1, 0, 1\}$  provided that  $i + \kappa_1 \in \mathbb{N}_{\leq N_1}$  and  $j + \kappa_2 \in \mathbb{N}_{\leq N_2}$ . Then we can express any non-zero entry of  $\mathbf{A}_{1,1}$  by

$$\mathbf{a}_{1,1}^{\xi(i,j), \xi(i+\kappa_1, j+\kappa_2)} = s_{1,1}^{\kappa_1, \kappa_2}$$

which is equal to  $s_{1,1}^{-\kappa_1, -\kappa_2}$  due to the symmetry of the stencil. We choose  $\hat{i}, \hat{j}$  such that  $\hat{i}, \hat{i} - \kappa_1 \in \mathbb{N}_{\leq N_1}$  and  $\hat{j}, \hat{j} - \kappa_2 \in \mathbb{N}_{\leq N_2}$ . Then the entry  $\mathbf{a}_{1,1}^{\xi(\hat{i}, \hat{j}), \xi(\hat{i} - \kappa_1, \hat{j} - \kappa_2)}$  exists and is, moreover, given by  $s_{1,1}^{-\kappa_1, -\kappa_2}$ . Finally we choose a coordinate transformation

$$\hat{i} = i + \kappa_1, \quad \hat{j} = j + \kappa_2$$

and end up with the equality

$$\mathbf{a}_{1,1}^{\xi(i,j), \xi(i+\kappa_1, j+\kappa_2)} = s_{1,1}^{\kappa_1, \kappa_2} = s_{1,1}^{-\kappa_1, -\kappa_2} = \mathbf{a}_{1,1}^{\xi(\hat{i}, \hat{j}), \xi(\hat{i} - \kappa_1, \hat{j} - \kappa_2)} = \mathbf{a}_{1,1}^{\xi(i+\kappa_1, j+\kappa_2), \xi(i,j)}$$

showing the symmetry of  $\mathbf{A}_{1,1}$ .

Coming back to the boundary stencils, their incorporation does not change the conclusion: In the Dirichlet case the argumentation above fits as well, in the Neumann case only diagonal elements of  $\mathbf{A}_{1,1}$  are updated by (2.30), which does not affect the symmetry of  $\mathbf{A}_{1,1}$ . The symmetry of  $\mathbf{A}_{2,2}$  can be proven analogously.

We are left with the equivalence of any non-zero entry in  $\mathbf{A}_{1,2}$  and the corresponding entry in  $\mathbf{A}_{2,1}$ . Let  $i, j, \kappa_1, \kappa_2$  be as above. It remains to show that

$$\mathbf{a}_{1,2}^{\xi(i,j), \xi(i+\kappa_1, j+\kappa_2)} \stackrel{!}{=} \mathbf{a}_{2,1}^{\xi(i+\kappa_1, j+\kappa_2), \xi(i,j)}.$$

Here, the argumentation from the case  $\mathbf{A}_{1,1}$  can be reused and we obtain, disregarding any boundary stencils for a moment, in a similar manner

$$\mathbf{a}_{1,2}^{\xi(i,j),\xi(i+\kappa_1,j+\kappa_2)} = s_{1,2}^{\kappa_1,\kappa_2} \stackrel{*}{=} s_{2,1}^{-\kappa_1,-\kappa_2} = \mathbf{a}_{2,1}^{\xi(\hat{i},\hat{j}),\xi(\hat{i}-\kappa_1,\hat{j}-\kappa_2)} = \mathbf{a}_{2,1}^{\xi(i+\kappa_1,j+\kappa_2),\xi(i,j)},$$

where in  $*$  the block-symmetry of  $\mathbb{S}$  has been employed. Again, boundary stencils from a Dirichlet condition do not change the conclusion. In the Neumann case only entries with  $\kappa_1 = \kappa_2 = 0$  are updated. Thus we have  $(i, j) = (\hat{i}, \hat{j})$  and it is easy to verify that  $\mathbf{a}_{1,2}^{\xi(i,j),\xi(i,j)} = \mathbf{a}_{2,1}^{\xi(\hat{i},\hat{j}),\xi(\hat{i},\hat{j})}$  holds, due to  $S_{1,2} = (S_{2,1})^\top$ , for all four cases from (2.30).

Thus,  $\mathbf{A}$  is symmetric. ■

If  $\mathbf{A}$  is symmetric, its eigenvalues are real. Under this condition, the Theorem of Gershgorin can be used to estimate the distribution of eigenvalues. Note that then the positiveness of all eigenvalues is equal to  $\mathbf{A}$  being positive definite.

**Theorem 2.21** (Gershgorin). *Suppose  $\mathbf{A} \in \mathbb{R}^{N \times N}$  is symmetric. If  $\mathbf{A}$  is split up in a diagonal matrix  $\mathbf{D} = (d_i)_i$  and a rest  $\mathbf{F} = (f_{ij})_{ij}$  with zero diagonal, i.e.  $\mathbf{A} = \mathbf{D} + \mathbf{F}$ , then*

$$EV(\mathbf{A}) \subset \bigcup_{i=1}^N [d_i - r_i, d_i + r_i]$$

where  $r_i = \sum_{j=1}^N |f_{ij}|$  for  $i = 1, \dots, N$ .

*Proof.* Can be found in (GOLUB & VAN LOAN, 1996).

Eventually, we recall the reaction-diffusion example one last time.

**Example 2.22** (Reaction-Diffusion Equation Revisited). An assembling of the system matrix from Example 2.13 yields a block matrix

$$\mathbf{A} = \begin{pmatrix} \mathbf{A}_{11} & 0 \\ 0 & \mathbf{A}_{22} \end{pmatrix} \in \mathbb{R}^{2N \times 2N},$$

where  $N := \#\Omega_h$ , with matrices

$$\mathbf{A}_{11} = \mathbf{A}_{22} = (\mathbf{a}_{i,j})_{1 \leq i,j \leq N} \quad \text{where} \quad \mathbf{a}_{i,j} = \begin{cases} -k/h^2, & |i-j| = N_1 \\ -k/h^2, & |i-j| = 1 \\ 1 + 4k/h^2, & i-j = 0 \\ 0, & \text{else} \end{cases}.$$

Then, by Theorem 2.21 the eigenvalues of the system matrix are included in the interval  $[1, 1 + 8k/h^2]$ . Since each eigenvalue is positive,  $\mathbf{A}$  is positive definite.

For the solution of the linear system we refer to literature: A general overview is given, for instance, by GOLUB & VAN LOAN (1996). Fast numerical schemes with complexities of  $\mathcal{O}(N \log N)$  or  $\mathcal{O}(N)$  especially adapted for image registration problems can be found in (FISCHER & MODERSITZKI, 1999, 2002, 2004). Last but not least, multi-grid techniques are advisable, cf., e.g., (TROTTEMBERG ET AL., 2001).





---

## 3 Variational Approach

---

This chapter introduces the variational approach for the image registration problem. Here, given a domain  $\Omega$ , images  $T, R \in \text{Img}(\Omega)$ , and some set of differentiable functions<sup>1</sup>,  $\mathcal{U} : \bar{\Omega} \rightarrow \mathbb{R}^d$ , the regularised Registration Problem 2.7 searches for a minimising function  $u \in \mathcal{U}$  such that

$$\mathcal{D}_{T,R}[u] + \alpha \mathcal{S}[u] \xrightarrow{u} \min \quad \text{on } \bar{\Omega} .$$

Rewriting the problem in a more general context, we consider the minimisation of a general functional  $\mathcal{J} : \mathcal{U} \rightarrow \mathbb{R}$ ,

$$\mathcal{J}[u] \xrightarrow{u} \min \quad \text{on } \bar{\Omega} . \quad (3.1)$$

To solve this general minimisation problem, a necessary condition for a minimum of  $\mathcal{J}[u]$  can be determined which typically yields the formulation of a boundary value problem. Such a condition must be fulfilled by a candidate solution and can be derived following a method by Lagrange. Here, the idea is to assume the existence of a solution  $u^*$  to (3.1) and to embed this solution into a set of candidate functions,

$$\{u_\tau : \bar{\Omega} \rightarrow \mathbb{R}^d \mid u_\tau(x) = u^*(x) + \tau v(x)\}$$

with  $\tau \in \mathbb{R}$  and  $v$  a test function, see Section 3.1. Then, this candidate set describes a one-dimensional subspace of  $\mathcal{U}$  and, assuming appropriate differentiability and boundary properties (detailed requisites will be given in Section 3.1), the function  $J : \mathbb{R} \rightarrow \mathbb{R}$ ,

$$J(\tau) := \mathcal{J}[u_\tau(x)] = \mathcal{J}[u^*(x) + \tau v(x)] ,$$

possesses a global minimum for  $\tau = 0$ , since  $u^*$  is a minimiser of  $\mathcal{J}$ .  $J$  is an ordinary function of the real variable  $\tau$  and thus the necessary condition for a minimum of  $J$  is given by the vanishing of the so-called first variation of  $\mathcal{J}$  in the direction of  $v$ ,

$$J'(0) = \left. \frac{d\mathcal{J}[u^* + \tau v]}{d\tau} \right|_{\tau=0} = 0 .$$

---

<sup>1</sup>On the boundary  $\partial\Omega$  the differentiability is to be understood in a one-sided meaning. Alternatively, the domain of  $\mathcal{U}$  could be defined as an open superset of  $\bar{\Omega}$ .

Later on we will see that for an image registration problem this condition takes the form of a boundary value problem for  $u^*$ . The link between, on the one hand, the task of solving a boundary value problem and, on the other hand, the task of finding a function that minimises a functional, is part of the calculus of variation. In this context, (3.1) is called the *variational formulation* of a boundary value problem for  $u^*$ .

The outline of this chapter is as follows. We start by introducing the calculus of variations as the core method of this chapter and consider the general minimisation problem in more detail. The boundary conditions of the resulting boundary value problem are discussed in Section 3.2. Afterwards, the general problem will be animated – a similarity measure and a regularising term are included as the two key aspects in non-parametric registration. By linking the registration problem to an initial boundary value problem, it can be discretised (Section 3.4) and solved numerically (Section 3.5). In the final section of this chapter the choice of parameters will be discussed.

### 3.1 Introduction into Calculus of Variations

We return to Lagrange’s method described above and present the underlying definition and analysis. Here, we follow the introductions given by OBERLE (1998), KÖNIGSBERGER (2004), and AXELSSON & BARKER (1984).

For a proper description of the general minimisation problem (3.1),  $\mathcal{U}$  denotes a *solution space* consisting of admissible functions with boundary conditions of ‘suitable’ type,

$$\mathcal{U} := \{u \mid u \in C^2(\bar{\Omega}, \mathbb{R}^d), u \text{ fulfills given boundary conditions}\}. \quad (3.2)$$

For a detailed comparison of different boundary conditions we refer to Section 3.2. By  $\mathcal{V}$  we denote a *test space* consisting of all functions which can be written as the difference between any two admissible functions,

$$\mathcal{V} := \{v \mid v = u - \hat{u}, u, \hat{u} \in \mathcal{U}\}. \quad (3.3)$$

Here, the boundary conditions follow from those chosen in  $\mathcal{U}$ . Note that  $\mathcal{V}$  is a linear space by construction.

We proceed by considering a particular subset of  $\mathcal{U}$ .

**Definition 3.1** (Neighbourhood). *Given a solution space  $\mathcal{U}$ , a function  $\hat{u} \in \mathcal{U}$  and  $\varepsilon > 0$ , then  $\mathcal{B}_\varepsilon(\hat{u})$  denotes the neighbourhood of  $\hat{u}$  as*

$$\mathcal{B}_\varepsilon(\hat{u}) := \{u \mid u \in \mathcal{U}, \|u - \hat{u}\|_{\mathcal{L}^2(\bar{\Omega})} < \varepsilon\}.$$

To keep notation simple, by a neighbourhood we also refer to a subset of a domain, i.e.  $\mathcal{B}_\varepsilon(\hat{x}) := \{x \mid x \in \Omega, \|x - \hat{x}\|_2 < \varepsilon\}$ . If a neighbourhood with respect to either a function space or a domain is meant, will be clear from the context.

With the general functional from (3.1) in mind, a local minimiser can be defined.

**Definition 3.2** (Local Minimiser). *Given a solution space  $\mathcal{U}$  and a functional  $\mathcal{J} : \mathcal{U} \rightarrow \mathbb{R}$ ,  $\hat{u} \in \mathcal{U}$  is said to be a local minimiser of  $\mathcal{J}$  if a number  $\varepsilon > 0$  exists such that*

$$\mathcal{J}[\hat{u}] \leq \mathcal{J}[u] \quad \text{for all } u \in \mathcal{B}_\varepsilon(\hat{u}).$$

To define the necessary condition for a local minimum of  $\mathcal{J}$ , the existence of a directional derivative is required.

**Definition 3.3** (Gâteaux Derivative). *Given a solution space  $\mathcal{U}$ , a test space  $\mathcal{V}$ , and a functional  $\mathcal{J} : \mathcal{U} \rightarrow \mathbb{R}$ ,  $\mathcal{J}$  is Gâteaux-differentiable for  $u \in \mathcal{U}$  in the direction of  $v \in \mathcal{V}$  if*

1. *a number  $\hat{\tau} > 0$  exists such that  $u_\tau := u + \tau v \in \mathcal{U}$  for all  $|\tau| \leq \hat{\tau}$ , and*
2. *the function  $J(\tau) := \mathcal{J}[u_\tau]$  is differentiable in  $\tau = 0$ .*

*The first order Gâteaux derivative (or directional derivative or first variation) of  $\mathcal{J}$  for  $u$  in the direction of  $v$  is defined by*

$$\delta \mathcal{J}[u; v] := J'(0) = \left. \frac{d\mathcal{J}[u + \tau v]}{d\tau} \right|_{\tau=0}.$$

Now, a stationary point can be defined.

**Definition 3.4** (Stationary Point). *Let a solution space  $\mathcal{U}$ , a test space  $\mathcal{V}$ , and a functional  $\mathcal{J} : \mathcal{U} \rightarrow \mathbb{R}$  be given. Suppose that for some  $\hat{u} \in \mathcal{U}$ ,  $\mathcal{J}$  is Gâteaux-differentiable for all test functions  $v \in \mathcal{V}$ . Then  $\hat{u}$  is said to be a stationary point of  $\mathcal{J}$  if*

$$\delta \mathcal{J}[\hat{u}; v] = 0 \quad \text{for all } v \in \mathcal{V}. \quad (3.4)$$

A necessary condition for a minimiser can be formulated by linking a stationary point to a local minimiser.

**Theorem 3.5** (Necessary Condition for a Local Minimiser). *Let a solution space  $\mathcal{U}$  with an admissible function  $\hat{u} \in \mathcal{U}$ , and a test space  $\mathcal{V}$  be given. In addition, let  $\mathcal{J} : \mathcal{U} \rightarrow \mathbb{R}$  denote a functional which is Gâteaux-differentiable for  $\hat{u}$  and all directions  $v \in \mathcal{V}$ .*

*If  $\hat{u}$  is a local minimiser of  $\mathcal{J}$ , then  $\hat{u}$  is a stationary point of  $\mathcal{J}$ .*

*Proof.* Can be found in, for instance, (AXELSSON & BARKER, 1984). ■

With this theorem in mind we investigate the condition for a stationary point in more detail. To this end we specify the general functional  $\mathcal{J}$  as

$$\mathcal{J}[u] := \int_{\Omega} F[x, u(x), \nabla u(x)] dx \quad (3.5)$$

with  $F : \bar{\Omega} \times \mathbb{R}^d \times \mathbb{R}^{d \times d} \rightarrow \mathbb{R}$  denoting a functional depending on  $x$ ,  $u(x)$ , and  $\nabla u(x)$ . Here and in the following, we assume  $\mathcal{J}$  to be Gâteaux-differentiable in

all directions of the respective test space, thus  $F$  is assumed to have continuous partial derivatives with respect to each of its arguments.<sup>2</sup>

Before investigating the condition for a stationary point, (3.4), some notation is introduced.

To distinguish the usual gradient<sup>3</sup>  $\nabla F = (\partial F/\partial x_1, \dots, \partial F/\partial x_d)^\top$  from the gradient of  $F$  with respect to  $u$ , i.e. with respect to its second argument,

$$\nabla_u F = \begin{pmatrix} \partial F/\partial u_1 \\ \vdots \\ \partial F/\partial u_d \end{pmatrix} \in \mathbb{R}^d, \quad (3.6)$$

we emphasise the dependence of the gradient by adding an index ‘ $u$ ’ to the operator. In a similar way, the gradient of  $F$  with respect to  $\nabla u$ , i.e. its third argument, is given by

$$\nabla_{\nabla u} F = \begin{pmatrix} \partial F/\partial u_{1,1} & \dots & \partial F/\partial u_{1,d} \\ \vdots & & \vdots \\ \partial F/\partial u_{d,1} & \dots & \partial F/\partial u_{d,d} \end{pmatrix} \in \mathbb{R}^{d \times d}, \quad (3.7)$$

again indexed by the dependent variable. Note that  $u_{i,j}$  is an abbreviation for  $\partial u_i/\partial x_j$ .

The condition for a stationary point of  $\mathcal{J}$  is given by the following lemma. For this moment we will restrict the solution space  $\mathcal{U}$  by prescribing a specific boundary condition, i.e.

$$\tilde{\mathcal{U}} := \{u \mid u \in \mathcal{C}^2(\bar{\Omega}, \mathbb{R}^d), u = c \text{ on } \partial\Omega\}.$$

Then, the corresponding test space is given by

$$\tilde{\mathcal{V}} := \{v \mid v \in \mathcal{C}^2(\bar{\Omega}, \mathbb{R}^d), v = 0 \text{ on } \partial\Omega\}.$$

However, in Section 3.2 the following result will be extended to the spaces  $\mathcal{U}$  and  $\mathcal{V}$ . Note, that we will use  $(\cdot, \cdot)$  and  $\nabla \cdot$  to denote the Euclidian scalar product and the divergence operator, respectively.

**Lemma 3.6** (Stationary Point of  $\mathcal{J}$ ). *A function  $u \in \tilde{\mathcal{U}}$  is a stationary point of the general functional  $\mathcal{J}$  (3.5) if*

$$\int_{\Omega} (\nabla_u F - \nabla \cdot \nabla_{\nabla u} F, v) dx = 0 \quad (3.8)$$

*holds for all test functions  $v \in \tilde{\mathcal{V}}$ .*

---

<sup>2</sup>In fact, for a stationary point of  $\mathcal{J}$  the differentiability of  $F$  with respect to its second and its third argument would be sufficient.

<sup>3</sup>A consistent notation would be  $\nabla_x$  instead of  $\nabla$ . For purpose of readability we remain with the latter version keeping in mind that the gradient operator with no index refers to the usual gradient with respect to the coordinates.

*Proof.* Let  $\tau \in \mathbb{R}$ . Then, by setting the Gâteaux derivative of  $\mathcal{J}$  for  $u$  in the direction of  $v$  to zero, we get

$$\begin{aligned}
0 = \delta \mathcal{J}[u; v] &= \left. \frac{d\mathcal{J}[u + \tau v]}{d\tau} \right|_{\tau=0} \\
&\stackrel{*}{=} \int_{\Omega} \left. \frac{dF[x, u(x) + \tau v(x), \nabla u(x) + \tau \nabla v(x)]}{d\tau} \right|_{\tau=0} dx \\
&= \int_{\Omega} \sum_{n=1}^d \left( \frac{\partial F}{\partial(u_n + \tau v_n)} \frac{\partial(u_n + \tau v_n)}{\partial \tau} \right) \Big|_{\tau=0} \\
&\quad + \sum_{n,m=1}^d \left( \frac{\partial F}{\partial(u_{n,x_m} + \tau v_{n,x_m})} \frac{\partial(u_{n,x_m} + \tau v_{n,x_m})}{\partial \tau} \right) \Big|_{\tau=0} dx \\
&= \int_{\Omega} \sum_{n=1}^d \frac{\partial F}{\partial u_n} v_n + \sum_{n,m=1}^d \frac{\partial F}{\partial u_{n,x_m}} v_{n,x_m} dx \quad \text{for all } v \in \tilde{\mathcal{V}}
\end{aligned} \tag{3.9}$$

where we employed in (\*) an interchange of differentiation and integration<sup>4</sup> followed by application of the chain rule. By using Gauß's Theorem as well as the abbreviations (3.6) and (3.7) we deduce

$$\begin{aligned}
0 &= \int_{\Omega} \sum_{n=1}^d \frac{\partial F}{\partial u_n} v_n dx - \int_{\Omega} \sum_{n,m=1}^d \frac{d}{dx_m} \frac{\partial F}{\partial u_{n,x_m}} v_n dx + \int_{\partial\Omega} \sum_{n=1}^d (\nabla_{\nabla u_n} F, \mathbf{n}) v_n dx \\
&= \int_{\Omega} (\nabla_u F - \nabla \cdot \nabla_{\nabla u} F, v) dx + \int_{\partial\Omega} \sum_{n=1}^d (\nabla_{\nabla u_n} F, \mathbf{n}) v_n dx
\end{aligned} \tag{3.10}$$

holding for all test functions  $v \in \tilde{\mathcal{V}}$ . Since every test function fulfills  $v = 0$  on  $\partial\Omega$ , the boundary integral vanishes and the proof is completed. ■

Clearly, (3.8) can hold for an arbitrary test function only if the first factor of the scalar product,  $\nabla_u F - \nabla \cdot \nabla_{\nabla u} F$ , vanishes identically. This assertion is included in the following well-known theorem. Its proof can be found in, for instance, (AXELSSON & BARKER, 1984). Here, we present a variant for  $d$ -dimensional functions.

**Theorem 3.7** (Fundamental Lemma of Variation). *Let  $\theta : \Omega \rightarrow \mathbb{R}^d$  be a continuous function. Then  $\int_{\Omega} (\theta, v) dx = 0$  holds for all test functions  $v \in \mathcal{V}$  if and only if  $\theta$  is identically zero on  $\Omega$ .*

*Proof.* First, we assume  $\int_{\Omega} (\theta, v) dx = 0$  to hold for all test functions and establish by contradiction that  $\theta \equiv 0$ .

Suppose that  $\theta_n(\hat{x}) \neq 0$  for some  $\hat{x} \in \Omega$  and  $n \in \{1, 2, \dots, d\}$ . Then, since  $\theta_n$  is continuous at  $\hat{x}$ , there exists a neighbourhood  $\mathcal{B}_{\varepsilon}(\hat{x}) \subset \Omega$  with  $\varepsilon > 0$ , such that  $\theta_n(x) > 0$  or  $\theta_n(x) < 0$  everywhere in  $\mathcal{B}_{\varepsilon}(\hat{x})$ . Choosing a  $v \in \mathcal{V}$  such that  $v_n(x)$

---

<sup>4</sup>See, e.g. (FORSTER, 1999).

is positive within  $\mathcal{B}_\varepsilon(\hat{x})$  and zero outside and such that  $v_m(x)$  is identically zero for  $m \neq n$ , we can conclude  $\int_\Omega (\theta, v) dx \neq 0$  for the chosen  $v$ . This is a contradiction to the assumption.

Setting  $\theta \equiv 0$ , it follows immediately that  $\int_\Omega (\theta, v) dx = 0$  for all test functions. ■

In summary,  $u \in \tilde{\mathcal{U}}$  is a stationary point of the Gâteaux-differentiable functional  $\mathcal{J}$  from (3.5) if

$$\nabla_u F - \nabla \cdot \nabla_{\nabla u} F = 0 \quad \text{on } \Omega. \quad (3.11)$$

By applying Theorem 3.5 we end up with (3.11) as a necessary condition for a (local) minimiser of (3.1).<sup>5</sup> Typically,  $d > 1$  and (3.11) constitutes a system of (partial) differential equations, called the *Euler-Lagrange equations*. Together with boundary conditions, e.g. described by  $\tilde{\mathcal{U}}$ , we are faced with a boundary value problem with the minimisation problem in (3.1) called its variational formulation (AXELSSON & BARKER, 1984). Before we investigate the role of boundary conditions in the definition of the solution space, we conclude this section with an example of a two-point boundary value problem.

**Example 3.8.** Let  $d = 1$ ,  $\Omega = (a, b)$ ,  $F = ru + \frac{1}{2}(u')^2$  with  $r \in \mathcal{C}([a, b], \mathbb{R})$  and  $\tilde{\mathcal{U}}$  as in Lemma 3.6. Then, the variational formulation takes the form

$$\int_a^b r(x)u(x) + \frac{1}{2}(u'(x))^2 dx \xrightarrow{u} \min$$

and is, by employing Lemma 3.6 and Theorem 3.7, equivalent to the two-point boundary value problem

$$\begin{aligned} u''(x) &= r(x), & x &\in (a, b), \\ u(x) &= c, & x &\in \{a, b\}. \end{aligned}$$

From the theory of ordinary differential equations it follows that this problem has a unique solution in  $\mathcal{C}^2([a, b])$ , see (AXELSSON & BARKER, 1984).

## 3.2 Boundary Conditions

In the definition of the solution space in (3.2) we have included some ‘suitable’ boundary conditions which are to be met by every admissible function  $u \in \mathcal{U}$ . This implies that in particular every stationary point of the general functional  $\mathcal{J}$  satisfies these conditions.

In this section we recall explicitly given conditions and address the use of essential vs. natural boundary conditions.

Two types of boundary conditions are introduced in Section 2.4, a Dirichlet type condition and a Neumann one. Based on the two types, further conditions such as sliding or bending ones are described in the literature (MODERSITZKI, 2004). These are designed for special applications and not addressed here.

---

<sup>5</sup>In (OBERLE, 1998) a different way is proposed to achieve a necessary condition. Here, requiring  $u$  to be once continuously differentiable is sufficient.

If the boundary conditions are imposed explicitly on a solution space  $\mathcal{U}$ , they are called *essential conditions*. These serve as boundary conditions of the boundary value problem and must be satisfied by an admissible function  $u \in \mathcal{U}$ .

If, in contrast, boundary conditions are not given explicitly in the definition of  $\mathcal{U}$ , we are dealing with *natural conditions*. These conditions are problem-dependent, they depend on the general functional  $\mathcal{J}$  or, to be exact, on its integrand  $F$ . For an illustration we recall (3.10). In its context we discussed the circumstances under which

$$\int_{\partial\Omega} \sum_{n=1}^d (\nabla_{\nabla_{u_n}} F, \mathbf{n}) v_n dx = 0 \quad (3.12)$$

holds when using the restricted spaces  $\tilde{\mathcal{U}}$  and  $\tilde{\mathcal{V}}$ . However, the same equality can be achieved when using the spaces  $\mathcal{U}$  and  $\mathcal{V}$  as defined in (3.2) and (3.3), for instance with a boundary condition on a part of the boundary only or even without any boundary condition. Following AXELSSON & BARKER (1984) we extend Lemma 3.6 and formulate a necessary condition for a minimiser of  $\mathcal{J}$ .

**Lemma 3.9** (Necessary Condition). *Every solution  $u^* \in \mathcal{C}^2(\bar{\Omega}, \mathbb{R}^d)$  of the general minimisation problem (3.1) with a Gâteaux-differentiable functional  $\mathcal{J}$  as in (3.5) is a solution of the boundary value problem consisting of the system of Euler-Lagrange equations*

$$\nabla_u F - \nabla \cdot \nabla_{\nabla u} F = 0 \quad \text{on } \Omega \quad (3.13)$$

and boundary conditions which can be either of essential type (when incorporated in the definition of the solution space  $\mathcal{U}$ ) or of natural type,

$$(\nabla_{\nabla_{u_n}} F, \mathbf{n}) = 0 \quad \text{on } \partial\Omega, \quad n = 1, \dots, d. \quad (3.14)$$

*Proof.* Let solution spaces

$$\mathcal{U} := \{u \mid u \in \mathcal{C}^2(\bar{\Omega}, \mathbb{R}^d)\}, \quad \tilde{\mathcal{U}} := \{u \mid u \in \mathcal{C}^2(\bar{\Omega}, \mathbb{R}^d), u = c \text{ on } \partial\Omega\}$$

and corresponding test spaces

$$\mathcal{V} := \{v \mid v \in \mathcal{C}^2(\bar{\Omega}, \mathbb{R}^d)\}, \quad \tilde{\mathcal{V}} := \{v \mid v \in \mathcal{C}^2(\bar{\Omega}, \mathbb{R}^d), v = 0 \text{ on } \partial\Omega\}$$

be given. Let  $u^* \in \mathcal{U}$  be a solution of (3.1), thus, following Theorem 3.5,  $u^*$  is a stationary point of  $\mathcal{J}$ . Let  $v \in \mathcal{V}$ . Then, from the proof of Lemma 3.6 the condition for a stationary point of  $\mathcal{J}$  is given by

$$\int_{\Omega} (\nabla_u F - \nabla \cdot \nabla_{\nabla u} F, v) dx + \int_{\partial\Omega} \sum_{n=1}^d (\nabla_{\nabla_{u_n}} F, \mathbf{n}) v_n dx = 0, \quad (3.15)$$

now holding for all  $v \in \mathcal{V}$ . In particular, (3.15) holds for a subspace of  $\mathcal{V}$ , e.g. for all  $v \in \tilde{\mathcal{V}}$ . For this subset, however, Theorem 3.7 implies the Euler-Lagrange equations (3.13). Inserting them into (3.15) yields (3.12) to hold for all test functions from  $\mathcal{V}$ . Since  $v \in \mathcal{V}$  can be arbitrarily chosen, (3.14) must be satisfied. ■

The condition (3.14) is called the corresponding natural boundary condition to the minimisation problem<sup>6</sup> in (3.1) with  $\mathcal{J}$  as in (3.5) and must be satisfied by a solution of the resulting boundary value problem.

**Example 3.10.** We consider again Example 3.8, now with modified boundary conditions.

Let the admissible functions fulfil an essential condition only on the left boundary of  $\bar{\Omega} = [a, b]$ , i.e.  $\tilde{\mathcal{U}} := \{u \mid u \in \mathcal{C}^2([a, b], \mathbb{R}^d), u(a) = c\}$ . Then, by construction,  $\tilde{\mathcal{V}} := \{v \mid v \in \mathcal{C}^2([a, b], \mathbb{R}^d), v(a) = 0\}$ .

An inspection of the boundary term (3.12) reveals  $[u'(x)v(x)]_a^b = 0$  to hold for all  $v \in \tilde{\mathcal{V}}$ , which is equivalent to  $u'(b)v(b) = 0, v \in \tilde{\mathcal{V}}$ , since  $u'(a)v(a) = 0$  follows from the essential boundary property of  $\tilde{\mathcal{V}}$  already. Lemma 3.9 gives  $u'(b) = 0$  as the natural condition and the following boundary value problem results

$$\begin{aligned} u''(x) &= r(x), & x &\in (a, b), \\ u(a) &= c, \\ u'(b) &= 0. \end{aligned}$$

### 3.3 Image Registration as Variational Problem

When introducing in Section 2.3.2 the image registration problem in the context of a non-parametric approach, a similarity measure alone yielded an ill-posed formulation. As a consequence, a smoothness constraint (or regulariser) has been added whose choice depends on the application specific physical properties. Then, the minimum configuration is a joint functional consisting of two building blocks,

$$\mathcal{J}[u] = \mathcal{D}_{T,R}[u] + \alpha \mathcal{S}[u] \xrightarrow{u} \min, \quad (3.16)$$

with  $\alpha \in \mathbb{R}^+$  as a positive weighting factor, recall Problem 2.7. The similarity measure as the first building block depends on the images  $T, R$  and the displacement whereas the regulariser as the second block depends on the displacement only. Due to the linearity of the Gâteaux derivative, each building block in (3.16) can be investigated independently. With the integrand  $F$  following from the definition of  $\mathcal{D}$  and  $\mathcal{S}$  (cf. the following sections), Lemma 3.9 can be applied to each building block separately. The Euler-Lagrange equations, resulting from each application, will then be combined and finally linked to an initial boundary value problem.

#### 3.3.1 Similarity Measures

The most popular measure is the so-called *sum of squared differences (SSD)*. It compares images of the same modality pointwise. As the major drawback it cannot be applied to images from different modalities. More powerful measures such as those based on the *normalised gradient* (HABER & MODERSITZKI, 2005), the *(local) cross-correlation* (WEESE ET AL., 1999) or the *mutual information* (COLLIGNON ET AL., 1995; VIOLA & WELLS, 1995) are suitable for

---

<sup>6</sup>The term ‘natural’ indicates that the conditions are naturally satisfied by the problem definition.



images from different modalities. In general,  $\mathcal{D}$  can be chosen as any measure provided its Gâteaux derivative exists. Here, we will employ the SSD measure because we only deal with monomodal images.

By comparing grey-values of the reference and the transformed template image pointwise, a measure of similarity for monomodal images is achieved.

**Definition 3.11** (Sum of Squared Differences (SSD) Measure). *Given two images  $T, R \in \text{Img}(\Omega)$  and a displacement field  $u \in \mathcal{U}$ , the sum of squared differences is defined as*

$$\mathcal{D}_{T,R}^{SSD}[u] := \frac{1}{2} \int_{\Omega} [R(x) - T_u(x)]^2 dx, \quad (3.17)$$

where  $T_u$  is an abbreviation for the transformed image  $T(x + u(x))$ .

From the following lemma it can be concluded that, in the context of Definition 2.2, for the SSD measure the images are required to be once continuously differentiable only.

**Lemma 3.12** (Euler-Lagrange Equation for the SSD Measure). *The system of Euler-Lagrange equations for the SSD measure is given by*

$$-[R(x) - T_u(x)] \nabla T_u(x) = 0, \quad x \in \Omega. \quad (3.18)$$

*Proof.* By straightforward application of Lemma 3.9. ■

Interpreting (3.18) we observe that the left-hand side shows large values whenever the difference between the considered image pair is large and, at the same time, the gradient of the transformed template image is large in its modulus, that is, if the transformed edge image possesses large values. Note that the sign in (3.18) has not been suppressed since we are interested in the Euler-Lagrange equations for the joint functional with (3.18) as just one building block.

### 3.3.2 Regularisation

The regularisation term can be understood as a penaliser of the displacement yielding a displacement field which is, generally speaking, smooth.

We start with the simplest choice, the so-called *diffusive regulariser*, and continue with an approach suitable for different material properties, the so-called *elastic regulariser*. For other regularisers, including fluidal- or curvature-based approaches, we refer to, e.g. (MODERSITZKI, 2004).

Note that the choice of the solution space  $\mathcal{U}$  determines the boundary conditions – either explicitly (when incorporating conditions of essential type) or implicitly (when conditions of natural type arise automatically). In this section, no boundary conditions are included in the solution space, therefore  $\mathcal{U}$  is equivalent to the space  $\mathcal{C}^2(\bar{\Omega}, \mathbb{R}^d)$ .

### Diffusive Regularisation

The diffusive regulariser penalises the gradient of the displacement in order to obtain a displacement field which is smoothed in each coordinate. It was introduced by FISCHER & MODERSITZKI (2002).

**Definition 3.13** (Diffusive Regularisation). *Given a displacement field  $u \in \mathcal{U}$ , the diffusive regulariser is defined as*

$$\mathcal{S}^{diff}[u] := \frac{1}{2} \int_{\Omega} \sum_{n=1}^d \|\nabla u_n(x)\|_2^2 dx . \quad (3.19)$$

**Lemma 3.14** (Euler-Lagrange Equation for the Diffusive Regulariser). *The system of Euler-Lagrange equations for the diffusive regulariser is given by*

$$-\Delta u(x) = 0 , \quad x \in \Omega . \quad (3.20)$$

*Proof.* Let  $F := \frac{1}{2} \sum_{n=1}^d \|\nabla u_n\|_2^2$ . Then we have  $\nabla_u F = 0$  and  $\nabla_{\nabla u} F$  is equal to the Jacobian of  $u$ . An application of Lemma 3.9 completes the proof. ■

The Euler-Lagrange equations (3.20) can be seen as an isotropic smoothing of the displacement field. Assuming for a moment,  $u$  to describe a physical property (like the particle density for instance), we are faced with the stationary case of the physical diffusion equation which motivates the naming of this regulariser.

Since  $\nabla_{\nabla u_n} F = \nabla u_n$ , the natural boundary condition to the diffusive regulariser is given by the zero Neumann condition

$$(\nabla u(x), \mathbf{n}(x)) = 0 , \quad x \in \partial\Omega . \quad (3.21)$$

Clearly, the diffusive regulariser can be also equipped with essential boundary conditions.

### Elastic Regularisation

The elastic regulariser dates back to the early eighties when BROIT (1981) suggested the following definition.

**Definition 3.15** (Elastic Regularisation). *Given a displacement field  $u \in \mathcal{U}$  and non-negative scalars  $\lambda \in \mathbb{R}_0^+$ ,  $\mu \in \mathbb{R}^+$ , the elastic regulariser is defined as*

$$\mathcal{S}_{\lambda, \mu}^{elas}[u] = \int_{\Omega} \frac{\mu}{4} \sum_{i,j=1}^d (\partial_{x_j} u_i(x) + \partial_{x_i} u_j(x))^2 + \frac{\lambda}{2} (\nabla \cdot u(x))^2 dx . \quad (3.22)$$

This formulation is based on the linear elastic potential. It assumes an isotropic behaviour and accounts for material properties by means of the Lamé parameters  $\lambda$  and  $\mu$ . These parameters can be related to the possibly more familiar

Young's modulus  $E \in \mathbb{R}_0^+$  and Poisson's ratio  $\nu \in [0, 1/2[$  by the relations (cf., e.g. (MALVERN, 1969)),

$$\begin{aligned} E &= \frac{\mu(2\mu + 3\lambda)}{\mu + \lambda}, & \nu &= \frac{\lambda}{2(\mu + \lambda)}, \\ \lambda &= \frac{E\nu}{(1 + \nu)(1 - 2\nu)}, & \mu &= \frac{E}{2(1 + \nu)}. \end{aligned} \quad (3.23)$$

The quantity  $1/E$  describes the relative stretch of an object in its longitudinal direction in dependence of applied forces. It is proportional to  $1/\mu$  provided  $\lambda = 0$ . The quantity  $\nu$  relates the relative transversal contraction of an object to its relative longitudinal dilation. A small value of  $\nu$  corresponds to  $\lambda \ll \mu$  and indicates compressibility (i.e. no volume preservation). In contrast, a value near to 0.5 corresponds to volume preservation. In this case an object is incompressible and gets thinner when being stretched. Note that the argumentation is based on Hooke's Law and, thus, is only valid for small displacements. For a reflection on when a displacement can be considered as being small, we refer to (PECKAR, 1998).

A differentiation of (3.22) with respect to  $u$  leads to the widely known Navier-Lamé equations.

**Lemma 3.16** (Euler-Lagrange Equation for the Elastic Regulariser). *The system of Euler-Lagrange equations for the elastic regulariser is given by*

$$-\mu\Delta u(x) - (\lambda + \mu)\nabla \cdot \nabla u(x) = 0, \quad x \in \Omega. \quad (3.24)$$

*Proof.* Let  $F_1 := \frac{\mu}{4} \sum_{i,j=1}^d (\partial_{x_j} u_i + \partial_{x_i} u_j)^2$  and let  $F_2 := \frac{\lambda}{2} (\nabla \cdot u)^2$ . Then  $\nabla_{\nabla u} F_1 / \mu$  is equal to the sum of the Jacobian of  $u$  and its transpose. Thus  $\nabla \cdot \nabla_{\nabla u} F_1 = \mu\Delta u + \mu\nabla \cdot \nabla u$ . Furthermore, we have  $\nabla \cdot \nabla_{\nabla u} F_2 = \lambda\nabla \cdot \nabla u$ . By Lemma 3.9 the proposition follows. ■

Setting, without any physical meaning (and disregarding the assumption in Definition 3.15),  $\lambda = -1$  and  $\mu = 1$ , (3.24) simplifies to the system of Euler-Lagrange equations for the diffusive regulariser, (3.20).

The natural boundary condition is – in contrast to the diffusive regulariser – different from the Neumann condition. A straightforward calculation yields for  $n = 1, \dots, d$

$$\nabla_{\nabla u_n} F_1 = \mu(\nabla u_n + \partial_{x_n} u) \quad \text{and} \quad \nabla_{\nabla u_n} F_2 = \lambda(\nabla \cdot u)e_n,$$

and the natural boundary condition reads

$$(\mu(\nabla u(x) + (\nabla u(x))^T) + \lambda \operatorname{diag}(\nabla \cdot u(x)), \mathbf{n}(x)) = 0, \quad x \in \partial\Omega. \quad (3.25)$$

**Remark.** For a registration problem with  $\Omega = (0, 1)^2$ , (3.25) is equivalent to

$$(\lambda + 2\mu)\partial_{x_1} u_1(x) = -\lambda\partial_{x_2} u_2(x) \quad \text{and} \quad \partial_{x_2} u_1(x) = -\partial_{x_1} u_2(x)$$

in the case of a horizontal boundary (i.e.  $\mathbf{n}_1 = 1, \mathbf{n}_2 = 0$ ) and to

$$(\lambda + 2\mu)\partial_{x_2} u_2(x) = -\lambda\partial_{x_1} u_1(x) \quad \text{and} \quad \partial_{x_2} u_1(x) = -\partial_{x_1} u_2(x)$$

in the case of a vertical boundary (i.e.  $\mathbf{n}_1 = 0, \mathbf{n}_2 = 1$ ).

### 3.3.3 Link to Boundary Value Problems

Having determined the Euler-Lagrange equations for different similarity and regularisation terms, we collect these results and build up a joint (system of) Euler-Lagrange equation(s). For the general functional  $\mathcal{J}$  as in (3.16) we obtain

$$\alpha Lu(x) = f(u(x)) , \quad x \in \Omega , \quad (3.26)$$

with,

1) following from the similarity measure,

$$f(u) := [R - T_u] \nabla T_u , \quad (3.27)$$

and, dependent on the choice of the regulariser,

2a) for the diffusive case

$$L := -\Delta , \quad (3.28)$$

2b) and for the elastic case

$$L := -\mu \Delta - (\lambda + \mu) \nabla \cdot \nabla . \quad (3.29)$$

Note that the Euler-Lagrange equation can be interpreted as an equation describing the balance between inner forces, given by the regularising term on the left-hand side of (3.26), and outer forces, given by the similarity measure on the right-hand side.

Adding a boundary condition

$$Bu(x) = 0 , \quad x \in \partial\Omega , \quad (3.30)$$

such as

$$B := \text{id} \quad (3.31)$$

for a Dirichlet type condition or

$$B := \partial/\partial \mathbf{n} \quad (3.32)$$

for a Neumann type condition, (3.26) and (3.30) together form a boundary value problem. Observing the non-linearity of (3.26) in  $u$ , we recall the argumentation in Section 2.4 and end up with an initial boundary value problem with  $u^{(0)} : \bar{\Omega} \rightarrow \mathbb{R}^d$  as a smooth initial function,

$$\begin{aligned} \frac{\partial u(x, t)}{\partial t} &= -[\alpha Lu(x, t) - f(u(x, t))] , & x \in \Omega , \quad t \in \mathbb{R}_0^+ , \\ u(x, 0) &= u^{(0)}(x) , & x \in \bar{\Omega} , \\ Bu(x, t) &= 0 , & x \in \partial\Omega , \quad t \in \mathbb{R}_0^+ . \end{aligned} \quad (3.33)$$

The following interpretation of the differential equation is obvious when we recall the functional  $\mathcal{J}$ , whose Gâteaux derivative is given by

$$\delta\mathcal{J}[u; v] = (\alpha Lu - f(u), v)_{\mathcal{L}^2(\Omega)}.$$

Then, the differential equation can be interpreted as a gradient descent approach in order to solve the general minimisation problem (3.1).

The discretisation of the initial boundary value problem is subject of the next section.

### 3.4 Discretisation

To keep the issue of interest clear we restrict the discretisation of (3.33) to the two-dimensional case and assume the unit square  $(0, 1)^2$  as domain  $\Omega$ . Nonetheless, the discretisation of the initial boundary value problem for any dimension is straightforward.

For the discretisation we employ the finite difference method. As introduced in Section 2.5, two different types of discretisation, each with grid spacing  $h = (h_1, h_2)$ , are considered: Firstly, an edge-point variant yielding  $\Omega_h^{\text{edge}}$  as the discretised domain and  $\partial\Omega_h^{\text{edge}}$  as its discretised boundary and, secondly, a mid-point variant yielding  $\Omega_h^{\text{mid}}$  and  $\partial\Omega_h^{\text{mid}}$ . Note that the notation  $\Omega_h$  and  $\partial\Omega_h$  is used whenever a statement is valid for both types of discretisation. In addition to the spatial grid points  $x_{i,j}$  the time axis is discretised by grid points  $\{t_l\}_{l \in \mathbb{N}_0}$  with grid spacing  $k$ . Finally, we recall  $U = (U_1, U_2)^\top$  as a pointwise function with  $U^{i,j,l}$  approximating  $u(x_{i,j}, t_l)$ .

In analogy to  $T_u$  we denote the discretised transformed template image by  $T_U$  where an interpolation scheme has been employed. Depending on the type of discretisation, discrete image values  $T_U^{i,j,l} = T_U(x_{i,j}, t_l)$  and  $R^{i,j} = R(x_{i,j})$  can be obtained. Note that the employed backward Lagrangian approach is preferable as pointed out in the following remark.

**Remark.** Following the backward Lagrangian approach involves two advantages. Firstly, the backward approach assigns a unique grey-value to each position in the new image whereas by the forward approach grey-values from different positions from the template image may be mapped onto the same position in the new image or, alternatively, no position from the template image is mapped onto a specific position in the new image. Secondly, the backward approach requires interpolation with respect to the grey-values from the template image. Since the grey-values are distributed on an equidistant grid, the interpolation is a simple task. The forward approach, however, requires interpolation in the new image (where the grey-values are arbitrarily distributed), to obtain a discrete image on an equidistant grid.

To discretise (3.33), we replace its derivatives by difference quotients. Here, we make use of discrete operators  $\text{id}_h$ ,  $L_h$ , and  $B_h$  referring to the identity mapping and the operators  $L$  and  $B$ , respectively. Similarly, by  $f_h U^{i,j,l}$  a discretisation of  $f(u(x_{i,j}, t_l))$  is described.

The resulting system of discrete equations can be assembled into a linear system of equations, see Section 2.5. As a more intuitive alternative to the complex description of the entries of the system matrix we present the stencil of  $L_h$  from which the matrix can be easily deduced. Note that essential properties of this system are its consistency with the initial boundary value problem and – with regard to numerical solving – the symmetry of its matrix.

We start with the description of the discrete equations.

**Lemma 3.17.** *Given the initial boundary value problem in (3.33) with abbreviations (3.27)–(3.29), (3.31), and (3.32), a discretisation with a local order of accuracy of  $\mathcal{O}(h^2 + k)$  is given by*

$$\begin{aligned} (\text{id}_h + k\alpha L_h)U^{i,j,l+1} &= U^{i,j,l} + kf_h U^{i,j,l}, & (i,j) \in \Omega_h, l \in \mathbb{N}_0, \\ U^{i,j,0} &= u^{(0)}(x_i, y_j), & (i,j) \in \bar{\Omega}_h, \\ B_h U^{i,j,l+1} &= 0, & (i,j) \in \partial\Omega_h, l \in \mathbb{N}_0, \end{aligned} \quad (3.34)$$

where

1)  $f_h$  is given by

$$f_h U^{i,j,l} = \begin{pmatrix} (R^{i,j} - T_U^{i,j,l})\partial_1^a \partial_1^\pm T_U^{i,j,l} & 0 \\ 0 & (R^{i,j} - T_U^{i,j,l})\partial_2^a \partial_2^\pm T_U^{i,j,l} \end{pmatrix}, \quad (3.35)$$

2a) for the diffusive case,  $L_h$  refers to the discretised operator

$$L_h = - \begin{pmatrix} \partial_{11}^\pm + \partial_{22}^\pm & 0 \\ 0 & \partial_{11}^\pm + \partial_{22}^\pm \end{pmatrix}, \quad (3.36)$$

2b) for the elastic case,  $L_h$  refers to the discretised operator

$$L_h = - \begin{pmatrix} (\lambda + 2\mu)\partial_{11}^\pm + \mu\partial_{22}^\pm & (\lambda + \mu)\partial_1^a \partial_2^a \partial_{12}^\pm \\ (\lambda + \mu)\partial_1^a \partial_2^a \partial_{12}^\pm & \mu\partial_{11}^\pm + (\lambda + 2\mu)\partial_{22}^\pm \end{pmatrix} \quad (3.37)$$

3a) for the case of Dirichlet type boundary conditions an edge-point discretisation is employed and  $B_h$  refers to

$$B_h = \text{id}_h, \quad (3.38)$$

3b) for the case of Neumann type boundary conditions a mid-point discretisation is employed and  $B_h$  refers to

$$B_h = \partial_n^\pm. \quad (3.39)$$

*Proof.* By using solely second-order difference quotients as introduced in (2.15), (2.18), and (2.20), (1)–(3b) can be easily deduced from (3.27)–(3.29), (3.31), and (3.32).

An application of Lemma 2.12 yields (3.34) as a consistent discretisation of (3.33) with a LOA of  $\mathcal{O}(h^2 + k)$ . ■

With the discrete equations in (3.34) a linear system of equations can be assembled as shown for Example 2.22. However, a better illustration is provided by the stencil notation given below for the discretised operator  $L_h$ .

**Corollary 3.18.** *Given the discretised operator  $\text{id}_h + k\alpha L_h$  with  $L_h$  as in (3.36) and (3.37), its stencil notation is given by*

$$\mathbb{S} = \left( \begin{array}{c} \begin{bmatrix} 0 & 0 & 0 \\ 0 & 1 & 0 \\ 0 & 0 & 0 \end{bmatrix} \\ \begin{bmatrix} 0 & 0 & 0 \\ 0 & 1 & 0 \\ 0 & 0 & 0 \end{bmatrix} \end{array} \right) - k\alpha \mathbb{S}_{L_h}$$

with

$$\mathbb{S}_{L_h} = \left( \begin{array}{c} \begin{bmatrix} 0 & h_1^{-2} & 0 \\ h_2^{-2} & -2(h_1^{-2} + h_2^{-2}) & h_2^{-2} \\ 0 & h_1^{-2} & 0 \end{bmatrix} \\ \begin{bmatrix} 0 & h_1^{-2} & 0 \\ h_2^{-2} & -2(h_1^{-2} + h_2^{-2}) & h_2^{-2} \\ 0 & h_1^{-2} & 0 \end{bmatrix} \end{array} \right)$$

for the diffusive case and

$$\mathbb{S}_{L_h} = \left( \begin{array}{c} \begin{bmatrix} 0 & \frac{\lambda+2\mu}{h_1^2} & 0 \\ \frac{\mu}{h_2^2} & -2\left(\frac{\lambda+2\mu}{h_1^2} + \frac{\mu}{h_2^2}\right) & \frac{\mu}{h_2^2} \\ 0 & \frac{\lambda+2\mu}{h_1^2} & 0 \end{bmatrix} \\ \begin{bmatrix} \frac{\lambda+\mu}{4h_1h_2} & 0 & -\frac{\lambda+\mu}{4h_1h_2} \\ 0 & \frac{\mu}{h_1^2} & 0 \\ -\frac{\lambda+\mu}{4h_1h_2} & 0 & \frac{\lambda+\mu}{4h_1h_2} \end{bmatrix} \end{array} \right)$$

for the elastic case. Furthermore, these block stencils are block-symmetric in the sense of Definition 2.18.

*Proof.* Follows immediately from Section 2.5. ■

Note, that without the use of averaging quotients  $\partial_1^a$  and  $\partial_2^a$  in the discretisation of the elastic operator, we would end up with inter-grid positions.

For a numerical solution of the discretised initial boundary value problem we employ the grid point mapping from (2.28) and assemble a system

$$\begin{aligned} \mathbf{A}\mathbf{U}^{(l+1)} &= \mathbf{U}^{(l)} + k\mathbf{F}^{(l)}, \quad l \in \mathbb{N}^0, \\ \mathbf{U}^{(0)} &= 0, \end{aligned} \tag{3.40}$$

where  $\mathbf{A}$  is constructed from the block stencil  $\mathbb{S}$  following (2.29) and (2.30) and thus includes both the discrete operator  $\text{id}_h + k\alpha L_h$  and the applicable boundary conditions. By the corollary above we know that  $\mathbb{S}$  is block-symmetric and therefore, by Lemma 2.20, the corresponding block matrix  $\mathbf{A}$  is symmetric. Furthermore, the lemma shows that the symmetry is not affected by the incorporation of the discrete boundary conditions from (3.38) or (3.39).

In addition to the symmetry of  $\mathbf{A}$ , its positive definiteness is ensured by Theorem 2.21 for the diffusive case. For the elastic case, the positiveness of the eigenvalues of  $\mathbf{A}$  depends on the choice of  $\alpha$ ,  $\lambda$ ,  $\mu$ , and on  $h$  and  $k$  as well. Precisely, the eigenvalues are lower bounded by  $1 - k\alpha(\lambda + \mu)/(h_1 h_2)$ , thus, for given  $h$ ,  $\alpha$ ,  $\lambda$ , and  $\mu$ , a choice of

$$k < \frac{h_1 h_2}{\alpha(\lambda + \mu)} \quad (3.41)$$

is sufficient to ensure positive definiteness for the elastic case.

### 3.5 Numerical Solution

Following the discretisation in the previous section, the assembled system of equations (3.40) is to be solved for  $\mathbf{U}^{(l+1)}$  in each iteration step. For given digital images  $R_h, T_h$  and discretisations of the regularisation parameter  $\alpha$ , and – in the case of the elastic regulariser – Lamé parameters  $\lambda, \mu$ , an algorithm can be sketched as follows.

**Algorithm 3.19.**

```

choose  $\mathbf{U}^{(0)}$  and  $k$ , assemble  $\mathbf{A}$ 
for  $l = 0, 1, \dots$  do
    compute force term  $\mathbf{F}$ 
    solve  $\mathbf{A}\mathbf{U}^{(l+1)} = \mathbf{U}^{(l)} + k\mathbf{F}$ 
    compute transformed template image  $T_{\mathbf{U}^{(l+1)}}$ 
end

```

We include a number of remarks which may be helpful to the reader.

- The initial displacement  $\mathbf{U}^{(0)}$  is usually set to the zero function unless further a priori knowledge is given. Additional information could be given by a pre-registration, by point- or surface-based correspondences or by model- or statistic-based information.
- Independently of (3.41), the choice of the time step size  $k$  requires some care. Looking at the right-hand side of the difference equation in (3.34) we observe that for the computation of the updated displacement  $\mathbf{U}^{(l+1)}$ ,  $k$  specifies the impact of the force term  $\mathbf{F}$  compared to the previous displacement  $\mathbf{U}^{(l)}$ . Thus, a large value of  $k$  favours the force term and may lead to a faster convergence to the steady state solution. However, a large  $k$  may also lead to oscillations if the update  $|\mathbf{U}^{(l+1)} - \mathbf{U}^{(l)}|$  is too large with respect to the distance between  $\mathbf{U}^{(l)}$  and the steady state solution. In contrast, a small value of  $k$  leads to a small update yielding a slow convergence in general.

A prediction for a suitable value of  $k$  can be obtained by estimating the terms  $\mathbf{F}$  and  $\mathbf{U}^{(l)}$ . Since the images are normalised to the grey-value interval  $[0, 1]$  (cf. Definition 2.3), each component of the force vector is bounded



by  $1/2h$ . Assuming a voxel width distance as a suitable maximum displacement for the first iteration step,  $\|\mathbf{U}^{(1)}\|_\infty \approx h$  is desired. Then, a value of  $k = 2h^2$  leads to a comparable magnitude of  $\mathbf{F}$  and  $\mathbf{U}^{(1)}$ . Typically,  $\|\mathbf{F}\|_\infty$  is much smaller than  $1/2h$  and  $k$  can be increased. In some cases it might be necessary to adjust  $k$  after the first iteration step and to recompute this step. To this end, inspired by MODERSITZKI (2004), the maximum  $\|\mathbf{U}^{(1)}\|_\infty$  is determined. If the maximum is larger than the voxel width,  $k$  will be reduced. Analogously,  $k$  will be increased if the maximum displacement is much smaller than  $h$ .

In our experiments, this procedure works well. However, since the operator  $\text{id} + k\alpha L$  is not linear in  $k$ , an appropriate rescaling cannot be given explicitly and a few attempts may be required to adjust  $k$ .

Having determined a suitable value for  $k$ , it will remain unchanged during the iteration.

- Due to the independence of  $\mathbf{A}$  of the time level, the assembly of  $\mathbf{A}$  is needed only once. The force term, however, depends on  $l$  and requires assembling in each iteration step.  
Both the assembly of  $\mathbf{A}$  and  $\mathbf{F}$  can be sped up by the use of matrix-vector routines.
- An important task is the solution of the linear system. The size of the system is  $dN$  and thus even a moderate two-dimensional medical image registration problem (with an image size of  $256^2$  voxels) results in a number of 131,072 unknowns. However, the matrix is sparse, highly structured, symmetric, and positive definite (provided  $k$  is chosen appropriately in the case of the elastic regulariser, cf. the previous section). If boundary conditions are properly chosen, solution schemes with linear-logarithmic or even linear complexity as developed by FISCHER & MODERSITZKI (1999, 2002, 2004) can be employed. Nonetheless, these methods require  $\alpha$ ,  $\lambda$ , and  $\mu$  to be constant all over the image domain and do not apply for variable regularisers as described in the next chapter.
- Another point worth of discussion is convergence of the registration scheme. As a matter of fact, instead of the minimisation problem (3.16), we discretised the related initial boundary value problem (3.33). Therefore, convergence can be evaluated in terms of determining a solution to the boundary value problem rather than in terms of determining a solution to the minimisation problem. To this end we discuss the choice of stopping criteria. Note that the definition of a ‘nice’ registration result is hard to specify in analytical terms and still a topic of discussion (MODERSITZKI, 2004). Nonetheless, broadly used indicators are
  - the relative reduction of the similarity measure with respect to the original images or to the previous iteration step,
  - the total or the relative change of  $\mathbf{U}$ , measured in the  $l^2$ - or the  $l^\infty$ -norm,
  - the size of the remaining forces, measured in the  $l^2$ - or the  $l^\infty$ -norm,

and, as developed in this thesis,

- a test on oscillations of the similarity measure. We assume that their occurrence corresponds to oscillations in  $\mathbf{U}$ , which may indicate that the local minimum of the optimisation problem is located within the displacement fields in two subsequent iteration steps<sup>7</sup>. Then, an oscillation in the similarity measure can be detected by evaluating

$$\frac{|\mathcal{D}_{T,R}^{SSD}[\mathbf{U}^{(l-2)}] - \mathcal{D}_{T,R}^{SSD}[\mathbf{U}^{(l-1)}]|}{\varepsilon + |\mathcal{D}_{T,R}^{SSD}[\mathbf{U}^{(l-2)}] - \mathcal{D}_{T,R}^{SSD}[\mathbf{U}^{(l)}]|},$$

where, since  $\mathbf{U}^{(l)}$  is defined on discrete points only, the integral in the definition of  $\mathcal{D}_{T,R}^{SSD}$  is replaced by a sum. While a constant reduction of the similarity measure results in a quotient of 1/2 and a zero reduction in the last iteration step is detected by a quotient of 1, a value much larger than 1 indicates an oscillation. We achieved satisfactory results with a threshold of 10.

- For the computation of the transformed template image  $T_{\mathbf{U}^{(l+1)}}$  an interpolation is required. Here, we used a (bi-)linear scheme.

To speed up the numerical treatment, Algorithm 3.19 is embedded into a multi-resolution approach. By using a downsampling routine with Gaussian filters (TROTTEMBERG ET AL., 2001), image pyramids

$$\{\{R_0, T_0\}, \{R_1, T_1\}, \{R_2, T_2\}, \dots\}$$

are generated, where  $\{R_0, T_0\}$  are equal to the original images and where the image size in each component is halved on transition to the next (coarser) level. Starting with Algorithm 3.19 on the coarsest level, a displacement field (on this level) is obtained. Then, an upsampled field is used as initial displacement  $\mathbf{U}^{(0)}$  on the next finer level.

In the literature (see, e.g. (TROTTEMBERG ET AL., 2001)), down- or upsampling routines are referred to as restriction (when transforming from fine to coarse) or prolongation (from coarse to fine). Here, the full weighting operator is used as restriction operator whereas a bilinear interpolation scheme serves as prolongation operator.

In the final section of this chapter we turn our attention towards the proper choice of the parameters  $\alpha$ ,  $\lambda$ , and  $\mu$ . Their choice has great influence on the registration result. Unfortunately, they are difficult to determine and their choice is still an active field of research.

---

<sup>7</sup>By choosing the time step  $k$  correctly, we can assume that the update in displacement is less than voxel width. In the case of oscillations,  $k$  could be further decreased allowing for an even better alignment of the images. Nonetheless, the displacement would change only on subvoxel level which makes, in our view, a further improvement redundant.

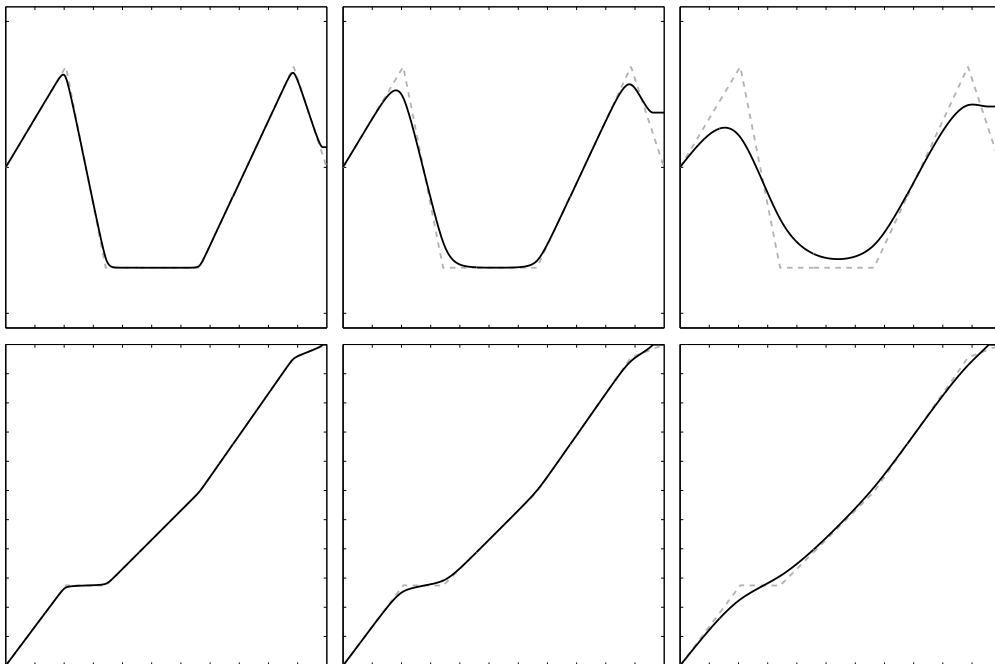


Figure 3.1: An application of a zig-zag type function (dashed line in each of the top row images) to the identity image results in a transformed image (depicted dashed in each of the bottom row images) and is considered as a limit case. Different values for  $\alpha$  ( $5 \cdot 10^{-5}$  in the left column,  $5 \cdot 10^{-4}$  centre and  $5 \cdot 10^{-3}$  in the right column) in the registration lead to different approximations (solid lines) to the limit case.

## 3.6 Choice of Parameters

For both regularisers considered in Section 3.3 we are left with the choice of the regularisation parameter  $\alpha$ . In addition, the elastic regulariser requires the choice of the Lamé parameters  $\lambda$  and  $\mu$ . However,  $\lambda$  and  $\mu$  cannot be chosen independently of  $\alpha$ . The three parameters can be simplified to  $\bar{\lambda} := \alpha\lambda$  and  $\bar{\mu} := \alpha\mu$ , or, alternatively,  $\alpha = 1$  can be set in the case of the elastic regulariser. Let us start with a discussion of  $\alpha$  in the presence of the diffusive regulariser.

### 3.6.1 Regularisation Parameter

The regularisation parameter links the building blocks of similarity measure and regulariser. Choosing it small (large) we expect a larger influence of the similarity measure (regulariser) and thus a transformation being less smooth (highly smooth). For a comparison of various choices for the regularisation parameter, a one-dimensional example is considered.

**Example 3.20.** Let  $d = 1$  and let the template image  $T$  be defined as the identity function on the interval  $[0, 1]$ . The reference image results from the application of a zig-zag type function on  $T$  as depicted with dashed lines in Figure 3.1, top row. Since the problem is one-dimensional, boundary conditions are required at the points  $\{0, 1\}$  only. On the left boundary a condition of

Dirichlet type has been chosen whereas on the right boundary a condition of Neumann type is presumed,

$$u(0) = 0, \quad u'(1) = 0.$$

Then, a registration scheme build up from the SSD measure (3.17) and the diffusive regulariser (3.19) yields an approximation of the reference image whose smoothness depends on the choice of  $\alpha$ . As expected, cf. Figure 3.1, bottom row, the larger  $\alpha$  is chosen the larger is the influence of the regulariser and the smaller is the resulting displacement.

**Remark.** The effect of different amounts of regularisation as visible in the example above reminds of the two types of linearisation introduced in Section 2.4. Replacing the linearisation of time-marching type (2.8) by one of fixed-point type (2.6), the effect of different amounts of regularisation cannot be achieved in the same way. This becomes obvious by a short reformulation of (2.6); independently of the choice of the regulariser, the operator  $L$  can be written as  $L =: \alpha \tilde{L}$  and (2.6) is equivalent to

$$\tilde{L}u^{(l+1)}(x) = \frac{1}{\alpha}f(u^{(l)}(x)), \quad x \in \Omega, \quad l \in \mathbb{N}_0. \quad (3.42)$$

Then, a choice of  $\alpha < 1$  may result in an update  $|u^{(l+1)} - u^{(l)}|$  whose maximum is much larger than voxel width distance. However, bounding the update to voxel width distance has the same effect as a larger choice of  $\alpha$  and, therefore, small values of  $\alpha$  do not lead to different solutions of (3.42) when using a linearisation of fixed-point type. Choosing  $\alpha > 1$ , however, may cause a very small update demanding for a much higher number of iterations compared to the linearisation of time-marching type.

In Example 3.20 the choice of  $\alpha$  has been linked to the smoothness of the resulting displacement. Alternatively, the regularisation parameter can be considered as a parameter controlling the capture range of a (peak) force.

**Example 3.21.** Let a template image be given with two non-zero pixels in its centre. Let the reference image consist of the same pixels but shifted by one pixel width in vertical direction. Then, solving this problem with the SSD measure, the diffusive regulariser and boundary conditions of Dirichlet type, we observe a peak force. The larger  $\alpha$ , the more this peak force is smoothed and the larger the capture range of the pixel shift, cf. Figure 3.2.

Having discussed the regularisation parameter in the examples above, its effect seems to be well understood: A large amount of regularisation results in a displacement which acts on a large region but with small amplitude. In contrast, a small amount of regularisation returns a displacement which is restricted to a small region but may show a larger amplitude. However, a proper choice of  $\alpha$  is still a challenging task as the following example reveals.

**Example 3.22.** Given an image pair (cf. Figure 3.3, top left, for the template image) we assume a regularisation parameter  $\alpha^*$  to be optimal from the view of

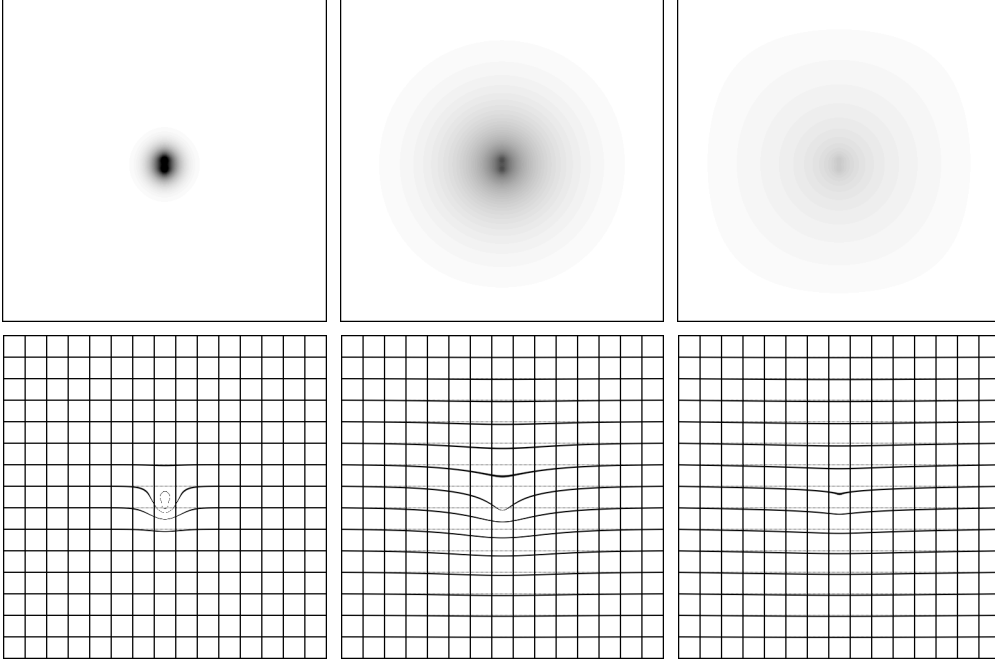


Figure 3.2: Visualised displacement field determined by solving a registration problem (see text) resulting in a peak force in the centre of the image.  $\alpha$  has been chosen as 0.08, 0.4, and 2 (from left to right). In the upper row the displacement field is visualised by plotting  $\|u(x)\|_2$  of each displacement vector  $u(x)$ , in the lower row  $u$  is applied to a Cartesian grid (the original grid is underlaid in light grey).

an application, and a time step size  $k^*$  chosen accordingly to Section 3.5. Note that, following Definition 2.2, the grey-values of the images are normalised to the interval  $[0, 1]$  before employing the registration algorithm.

Furthermore, we assume the same image pair given again, but now with a simulated metal artefact in the upper left corner of the template image of, say, maximum grey-value 2. Normalising this image according to Definition 2.2 results in an image where the grey-values of the non-artefact structures are of half value than before, cf. Figure 3.3, top right. For the non-artefact structures both the difference  $R - T_u$  and the gradient  $\nabla T_u$  is halved and, therefore, when using for instance the SSD measure, their contribution to the force term  $f(u(x)) = [R(x) - T_u(x)]\nabla T_u(x)$  is reduced to 25%, i.e.  $f^{\text{metal}} = 0.25 f^{\text{orig}}$ . Consequently, when employing the registration algorithm, the resulting displacement field for the image pair including an artefact differs from that for the original image pair as shown in Figure 3.3, bottom left and centre.

A short inspection of the discretised initial boundary value problem (3.34) reveals the difference equation

$$(\text{id}_h + k^* \alpha^* L_h) U^{i,j,l+1} = U^{i,j,l} + k^* f_h^{\text{orig}} U^{i,j,l}$$

to be equivalent with

$$(\text{id}_h + k^{\text{metal}} \alpha^{\text{metal}} L_h) U^{i,j,l+1} = U^{i,j,l} + k^{\text{metal}} f_h^{\text{metal}} U^{i,j,l}$$

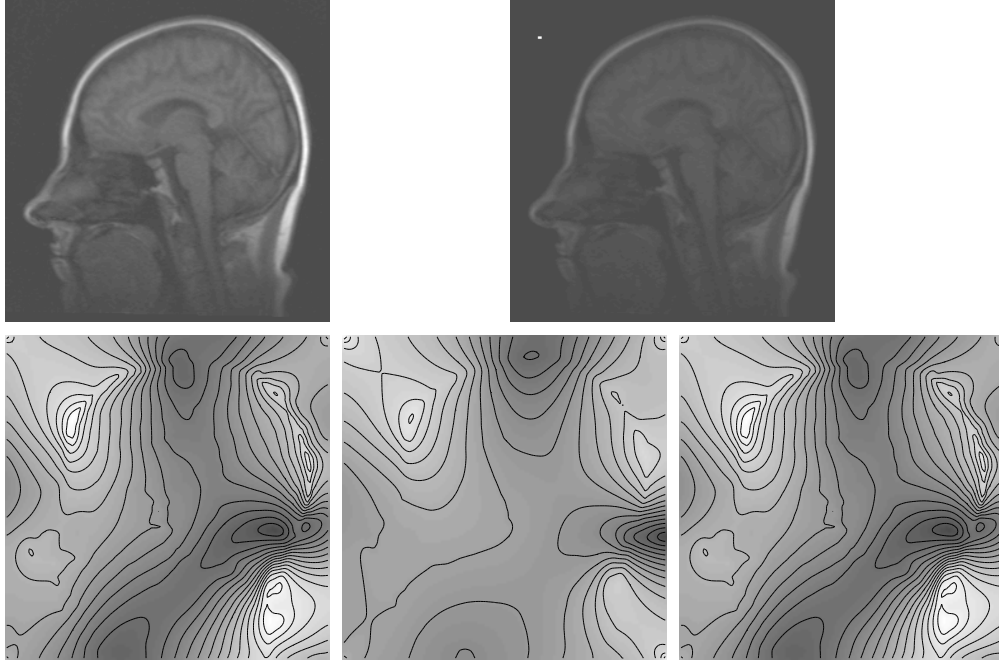


Figure 3.3: In the upper row the template image is shown, once original (left), once with a pseudo metal artefact in its upper left corner (right). Below, the resulting displacement fields are shown by colour-coding the  $l^2$ -norm of each displacement vectors (dark grey corresponds to small vectors, light grey to large ones; for better visualisation contour lines have been added): On the left for the original image, in the centre for the image with a metal artefact, and on the right again for the metal artefact image but now with a corrected value of  $\alpha$ . See text for further explanations.

provided  $\alpha^{\text{metal}} = 0.25\alpha^*$  and  $k^{\text{metal}} = 4k^*$ . Then, employing the registration algorithm again for the metal images, we receive a displacement field (cf. Figure 3.3, bottom right) which is the same as for the original image pair but now with a regularisation parameter being reduced to one fourth. Note that the relation linking  $k^{\text{metal}}$  to  $k^*$  causes a lower number of iterations only and does not change the regularity of the displacement field.

Thus, in the presence of image artefacts or noise, different choices of  $\alpha$  may be essential in order to obtain a registration result showing the same degree of smoothness than for the original image pair.

This observation can be extended to applications where the displacement of a particular region of an image is of interest. Here, the choice of the regularisation parameter may be a difficult task since its value may highly depend on the content of the whole image. This agrees to the observation in the literature that a fully automatic choice of  $\alpha$  is still a challenging problem (MODERSITZKI, 2004) and may require further a-priori information.

### 3.6.2 Lamé Parameters

The elastic regulariser includes two additional parameters to discuss, the Lamé parameters  $\lambda$  and  $\mu$ . However, as argued at the beginning of Section 3.6, due to

the dependence of  $\alpha$  and the Lamé parameters on each other, the regularisation weight can be ignored, i.e.  $\alpha = 1$ . We investigate the Euler-Lagrange equation for the elastic case and combine it with that for some similarity measure,

$$-(\mu\Delta + (\lambda + \mu)\nabla \cdot \nabla)u = f(u),$$

which can be transformed into

$$-\left(\Delta + \left(\frac{\lambda}{\mu} + 1\right)\nabla \cdot \nabla\right)u = \frac{1}{\mu}f(u).$$

Recalling Section 3.3.2 we make use of the more intuitive parameters  $E$  and  $\nu$  describing Young's modulus and Poisson's ratio, respectively, and substitute  $\lambda$  and  $\mu$  by relations from (3.23),

$$-\left(\Delta + \frac{1}{1-2\nu}\nabla \cdot \nabla\right)u = \frac{2(1+\nu)}{E}f(u). \quad (3.43)$$

We observe that  $E$  appears on the right-hand side only. Moreover,  $E$  may be seen as a scaling of the force term  $f$ . This scaling coefficient is little dominated by  $\nu$ , since its physically meaningful value is within the interval  $[0, 0.5[$  and, therefore, the scaling coefficient is in the range  $[2/E, 3/E[$ . In contrast,  $\nu$  takes a dominant role on the left-hand side of (3.43). Here, it controls the weighting of the Laplacian term vs. the divergence term. While the Laplacian acts separately on each component, the divergence term causes the coupling of components due to its mixed derivative terms. This coupling effect is the more dominant, the larger  $\nu$  is chosen and ranges from being equal to the Laplacian influence in the case of  $\nu = 0$  to its exclusive preference if  $\nu$  is close to 0.5. Consequently,  $\nu \in [0, 0.5[$  controls the coupling of the components of the displacement field. In terms of the Lamé parameters, this range corresponds to  $\lambda$  chosen from the interval  $[0, \infty[$ . We illustrate this effect in the following example.

**Example 3.23.** We consider an image with a square in its centre. Instead of the force term resulting from a similarity measure we employ again artificial forces. They are located on the right and on the left of the square in order to pull it apart. Then, solving (3.40) with  $\mathbf{A}$  originating from the elastic regulariser and boundary conditions of Neumann type, we model the expansion of an elastic bar with different material properties, cf. Figure 3.4. For all runs  $\mu = 1$  is chosen fixed whereas  $\lambda$  varies.

Employing a value  $\lambda = 0$  (corresponding to  $\nu = 0$ ), a displacement field results which shows a small amount of transversal movement (relatively to the longitudinal movement) caused by coupling effects, cf. Figure 3.4, centre column. Increasing  $\lambda$  enlarges this effect: When applying the same stretching forces to the bar, it gets more thinned the larger  $\lambda$  is chosen, cf. the right column for a value  $\lambda = 10^3$  (corresponding to  $\nu = 0.4995$ ). For comparison we disregard the assumption  $\lambda \geq 0$  from Definition 3.15 for the last case and choose  $\lambda = -\mu$  (corresponding to  $\nu = -\infty$ ), cf. the left column of Figure 3.4. Here, the coupling effect has been switched off and the bar does not get thinned at all when being stretched. This case displays the reaction of the diffusive regulariser (since the

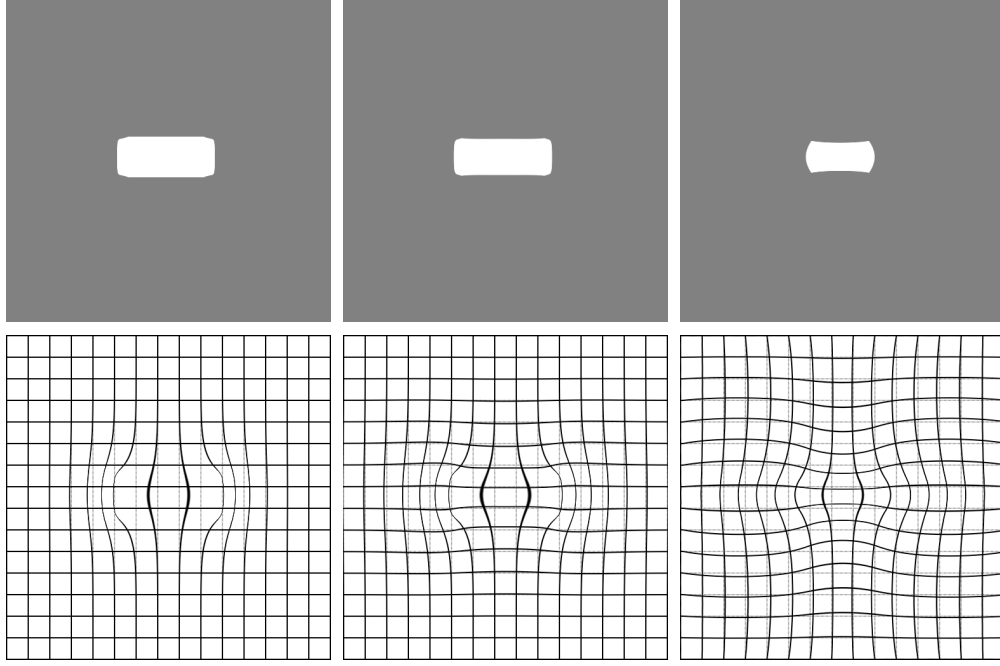


Figure 3.4: Results for the stretching of an elastic square with different material properties are depicted in the upper row. Below, the same displacement field is applied to a Cartesian grid. For better comparison, the original non-deformed grid is underlaid in light grey. In all cases  $\mu = 1$  is chosen. The centre and the right column refer to values of  $\lambda = 0$  and  $\lambda = 10^3$  (corresponding to  $\nu = 0$  and  $\nu = 0.4995$ ), respectively, whereas the left column originates from the not physically meaningful choice of  $\lambda = -\mu$  (corresponding to  $\nu = -\infty$ ).

Euler-Lagrange equation for the elastic regulariser reduces to the one for the diffusive regulariser if  $\lambda = -\mu$ ).

Summarising, a horizontal stretching of an elastic bar leads to a relative transversal movement whose amount becomes larger the larger  $\lambda$  (or  $\nu$ ) is chosen. For the different cases, this transversal movement appears in Figure 3.4, bottom row, as displacement of the horizontal lines in the Cartesian grid with regard to the original grid. In the (non-physical) case of  $\lambda = -\mu$  (or  $\nu = -\infty$ ) the transversal movement has vanished at all.

**Remark.** In Chapter 6, a large value of  $\lambda$  compared to  $\mu$  will be used to achieve results which show volume preservation. This is motivated by the physical interpretation of incompressibility corresponding to a large value of  $\lambda/\mu$ . However, in the example above, the volume is not preserved even in the case of  $\lambda = 10^3$ , moreover, the deformed square object is by 19% larger than the original square. The reason of this behaviour can be traced back to the underlying Hooke's Law which is valid only for small displacements. Clearly, an enlargement to a size more than double cannot be interpreted as a 'small' displacement (cf. (PECKAR, 1998)) and the assumption of Hooke's Law is violated.



As a consequence of using  $\lambda$  (resp.  $\nu$ ) as the control parameter of the relative transversal movement we do not agree with authors (e.g. (BAJCSY & KOVAČIČ, 1989; MODERSITZKI, 2004)) who suggested to set  $\lambda = 0$  in all cases for practical reasons. Such a choice cannot distinguish between different amounts of transversal movement as they occur with different types of soft tissues.

We are left with the question of how to choose the Lamé parameters for a specific application. HAGEMANN (2001) reported on a literature study comparing values for brain tissue and for skull bone. Although, for the same type of anatomical structure the values differ a lot, a better correlation was observed when comparing the quotients  $\lambda^{\text{brain}}/\mu^{\text{brain}}$  and  $\lambda^{\text{skull}}/\mu^{\text{skull}}$  for brain tissue and skull bone, respectively. These ratios prescribe the amount of elasticity in a relative way rather than in an absolute one. This mirrors nicely the fact that the grey-value scale of the images (and thus the scale of  $f$ ) can be arbitrarily chosen. Nevertheless, the ratios may serve as orientation only: To reflect different applications such as brain registration in an inter-subject or intra-subject context, possibly even with a brain shift involved, an adaption of the ratios seems to be reasonable.

However, different amounts of elasticity cannot be mixed in a single application since the Lamé parameters are constant in the entire domain. The following chapter extends the registration scheme described so far and allows to provide image structures such as bone or soft tissue structures with individual elastic properties.



---

## 4 Variable Regularisation

---

This chapter extends the regularisation approach described so far in two directions: It introduces the concept of material variability and prepares for topological changes. Starting from a motivation, Section 4.2 describes how to incorporate variability into the regularisation framework. By the use of the variable diffusive or the variable elastic regulariser from Section 4.3 it is possible to force a specific material behaviour in specified image regions. Furthermore, these regions may displace independent of each other but without resulting in non-physical solutions such as an overlap or swap of regions. Linked to an initial boundary value problem, discretisation and numerical treatments are presented in Section 4.4 and 4.5 respectively. The chapter is concluded by a discussion of the choice of parameters.

### 4.1 Motivation

The need for variability in the regularisation and the material properties can be best seen by considering a synthetic example. Let the template image consists of two objects next to each other as shown in Figure 4.1, left. Both objects are pulled at their top. For the left one we assume a stretching in the force direction, simulating the deformation of a soft-tissue object being pulled. The right object represents a bone structure, thus – under the same pulling force – it moves slightly in direction of the acting force but preserves its shape. In addition, the reference image possesses an artefact which is located near to the top of the right object, cf. Figure 4.1, centre left. This artefact will help us to study the effect of additional properties in the registration framework.

For a registration of the described image pair we choose the SSD measure and the elastic regulariser with Lamé parameters  $\lambda = 2$  and  $\mu = 4$ . We use Neumann boundary conditions and set the regularisation parameter to  $\alpha = 1/32$ . The result, shown in Figure 4.1, centre right<sup>1</sup>, reveals a failure of registration.

---

<sup>1</sup>For purpose of visualisation, the transformed template image is generated in such a way that after registration the displacement is applied to a modified template image where both objects are underlayed with a chequerboard pattern.

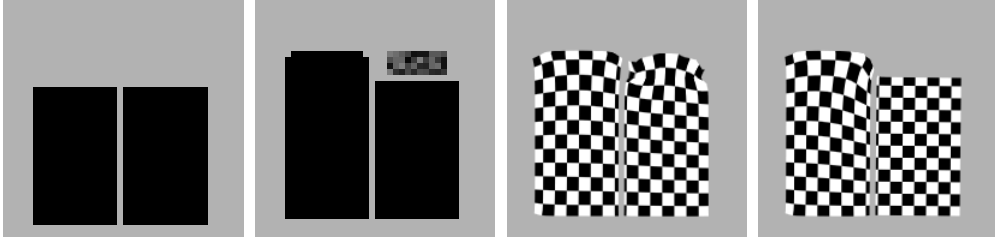


Figure 4.1: Template and reference image are shown on the left, two registration results are shown on the right. Centre right the result for a constant choice of parameters is depicted, beside  $\mu = 4000$  is chosen for the right object. For visualisation purpose, the template image is underlayed with a chequerboard pattern retrospectively of the registration.

In particular the right object, representing bone structure, is misaligned and deformed. A closer inspection of this object shows the reason: Although its shape coincides in both given images, the registration tries to optimise the *overall* similarity (besides the regularisation). Thus, a straightening of the right object similar to that of the left one reduces the distance between reference and transformed image but does not change the penalisation by the regulariser significantly. From the view of the minimiser, an expansion of both objects is therefore preferred.

By attaching material properties to the objects, further knowledge can be added. For the Lamé parameters of the right object dedicated values are specified (here  $\mu = 4000$ ) whereas the other parameters as well as  $\mu$  in the rest of the image remain unchanged. Now, the algorithm is not only intensity-based but knowledge-based as well. A registration results in a displacement being more intuitively satisfying than before (Figure 4.1, right). Due to the prescribed rigidity (modelled by  $\mu$ , cf. Section 3.3.2 for a discussion of the Lamé parameters), the regulariser has a greater influence locally compared to the distance measure and the right object preserves its shape. Furthermore, an upward movement yielding an improved similarity of the grey-values with respect to the artefact does not arise, since at the same time this would reduce similarity of the grey-values in the lower part of the object.

However, in both experiments it is remarkable that the displacements of the two objects depend on each other: While in the first experiment the right object is stretched more on its left size, in the second experiment the left object appears as being clipped to the right one. Consequently, the displacement of one object depends on that of the other one – regardless of the use of individual material properties.

To investigate this observation in greater detail, we consider a second illustrative example. Again, the images consist of two objects, this time identical in shape but separated from each other by a gap of variable size, cf. Figure 4.2, left column. The size of the gap is assumed to be small in the template image and large in the reference image.

For the registration the same setting as for the first experiment is used. The result indicates two effects, cf. Figure 4.2, second column. Firstly, the size of

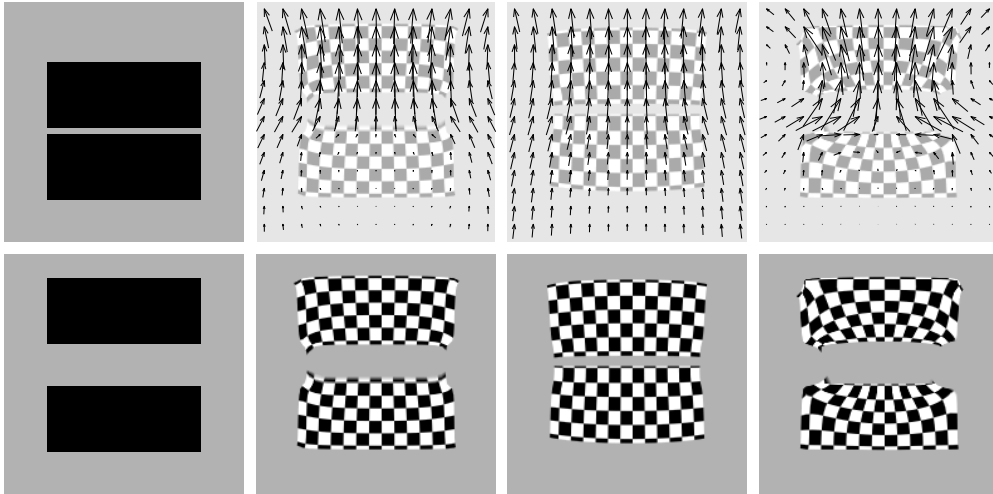


Figure 4.2: For a given image pair (top left for the template image and bottom left for the reference one) and a regularisation parameter of  $\alpha = 1/32$ ,  $\alpha = 1/4$ , and  $\alpha = 1/128$  (second to last column) various registration results can be obtained. In the bottom row the transformed template is depicted, for better visualisation in the top row the displacement field on a coarsed grid is added.

the gap is enlarged, but by far not as much as required by the reference image. Furthermore, the contours of the objects along the gap get blurred due to the regularisation of the displacement field. Secondly, both objects get thinned in the neighbourhood of the gap. This is caused by the use of an elastic model having no knowledge of the image structure and thus considering the whole image as a single elastic block which gets thinned when stretching it (cf. the displacement field in Figure 4.2, top centre left).

For an improved registration result one could choose a larger value for  $\alpha$ , for instance  $\alpha = 1/4$  as in Figure 4.2, third column. Then, the shape of the objects is better preserved, but the larger  $\alpha$  is, the more the gap remains in its template position. In contrast, one could choose a smaller value, leading to a correct gap in the reference image, cf. Figure 4.2, right column, for  $\alpha = 1/128$ . However, the regulariser is now weakened over the entire image domain. Deformations may occur in regions other than wanted and image noise will start to influence the result.

As a better choice we suggest a combination of both effects. By defining a small value of  $\alpha$  in the gap region and a large one within the objects we expect the gap to become larger and the objects to displace uniformly.

Therefore, instead of a globally uniform regularisation, a spatially dependent regularisation is the essential prerequisite for the registration of a material-dependent problem. In particular, only regions with a gap that is expected to become larger or smaller, need a local reduction of smoothness whereas all other regions shall be regularised according to the chosen physical model.

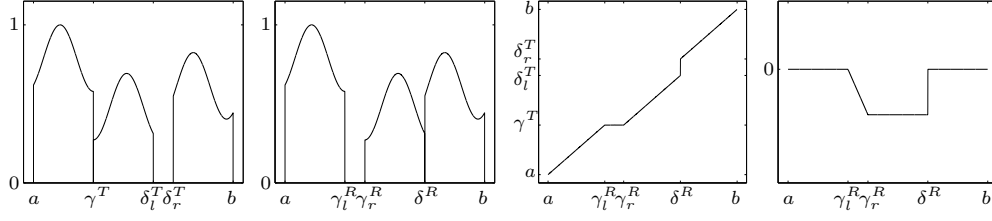


Figure 4.3: Artificial 1D image  $T$  (left) which can be transformed into  $R$  (centre left) using an ideal mapping  $x + u(x)$  (centre right) with the displacement  $u$  (right).

## 4.2 Variable Influence of Regularisation

To obtain a spatially dependent regularisation, we replace the constant weighting factor  $\alpha$  by a continuously differentiable weighting function  $\alpha : \Omega \rightarrow \mathbb{R}^+$ . First of all it is not clear, *if* a specific choice of the weighting function can enforce a particular behaviour of the solution as required in a material-dependent problem. Then, one has to detect the cases *where* a specific choice shall apply. Since this decision cannot simply be deduced from the grey-values, further knowledge is required.

Note that our interest lies in determining a minimiser of the general minimisation problem introduced in (3.1). Its existence and uniqueness are important issues and need investigation. However, their proof is outside the scope of this thesis and we remain with an investigation of the necessary condition for a minimiser.

### 4.2.1 Choice of the Weighting Function

Having replaced the weighting factor  $\alpha$  by a weighting function  $\alpha(x)$ , we are concerned with the choice of  $\alpha(x)$ . Our purpose is twofold.

Firstly, we wish to model a gap becoming larger as seen in the synthetic example in Figure 4.2. Here, we observed how a pulling force on the upper object yielded an enlargement of the gap between the objects. The second case is vice versa. Given two objects with a large gap between them, we wish to model a shrinking gap by applying a pushing force on the upper object. Therefore the question is, how to choose  $\alpha$  in order to force the displacement field to exhibit a particular behaviour. To this end, the analytical solution of a one-dimensional variational model will be inspected. Afterwards, we will construct sequences for  $\alpha$  and  $u$  which converge to limit functions showing the desired behaviour.

Let us note, that our aim is not to propose a one-dimensional registration method based on an analytical solution. Instead we are aiming at bringing forward insights from the analytical inspection of different weighting functions towards a generalised variational approach.

Given the one-dimensional registration problem as shown in Figure 4.3, left and centre left, the material objects from the two-dimensional problem correspond to the three intervals  $\{(a, \gamma^T), (\gamma^T, \delta_l^T), (\delta_l^T, \delta_r^T), (\delta_r^T, b)\}$  and  $\{(a, \gamma_l^R), (\gamma_l^R, \gamma_r^R), (\gamma_r^R, \delta^R), (\delta^R, b)\}$  in the template and the reference image, respectively. An ideal solution to this problem is given by the mapping depicted in Figure 4.3, centre right. Applying this mapping to the template image results in the reference image. Here, the

constant function value in the interval  $(\gamma_l^R, \gamma_r^R)$  is responsible for enlarging a gap and the approximated step in the function values around  $\delta^R$  causes a shrinkage of a gap. By disregarding the trivial part of that mapping we are left with the displacement function  $u$  itself, shown in Figure 4.3, right. Here, the ramp corresponds to the enlarging gap and the approximated step to the shrinking gap.

We modify the diffusive regulariser from Section 3.3.2 by incorporating a weighting function<sup>2</sup>. From a straightforward application of variational calculus (cf. Section 3.1) we know that minimising the sum of the SSD measure and the modified regulariser,

$$\int_a^b [R(x) - T_u(x)]^2 dx + \int_a^b \alpha(x) [u'(x)]^2 dx , \quad (4.1)$$

supplemented by boundary conditions of, for instance, Dirichlet-type, leads to the boundary value problem

$$\begin{aligned} [\alpha(x)u'(x)]' &= -[R(x) - T_u(x)]T_u'(x) , \quad x \in (a, b) , \\ u(a) &= u_a , \\ u(b) &= u_b . \end{aligned} \quad (4.2)$$

To investigate the relation between  $\alpha$  and  $u$ , an analytical solution of (4.2) is of great utility. However, (4.2) is nonlinear in  $u$  and in general the solution of this nonlinear differential equation cannot be given explicitly. Alternatively, we consider a registration depending on the inner forces only (i.e.  $\int [R - T_u]^2 dx$  is assumed to be constant) and set the right-hand side to zero which corresponds to the diffusion equation in the stationary case. For this reduced form an analytical solution is available,

$$u(x) = u_a + \frac{u_b - u_a}{\int_a^b \frac{1}{\alpha(t)} dt} \int_a^x \frac{1}{\alpha(t)} dt . \quad (4.3)$$

Recalling our purpose for the choice of  $\alpha$  let us consider the case of an enlarging gap and that of a shrinking gap. To this end we will construct sequences of weighting functions whose limit functions represent these cases.

Let  $(\alpha_\tau)_{\tau \in \mathbb{N}}$  denote a sequence of weighting functions and let  $(u_\tau)_{\tau \in \mathbb{N}}$  be the sequence of solutions determined by (4.3) when substituting  $\alpha$  by  $\alpha_\tau$ .

We start with the case of a shrinking gap. Here, a weighting function is searched in order to let two intervals with a gap between them move together (as the centre and the right interval in Figure 4.3). Placing forces pushing the intervals together corresponds to boundary conditions with  $u_a < u_b$ . Now,  $\alpha_\tau$  is searched such that  $u_\tau$  converges to a step function as  $\tau \rightarrow \infty$ . Note that the variational model aims at minimising the integral sum in (4.1). Thus a candidate function  $\hat{u}$  with a high value of  $\hat{u}'$  at any position is more penalised than a function whose gradient is small everywhere. Consequently,  $\hat{u}$  will be less preferred in terms of a solution to the minimisation of (4.1). A sequence  $u_\tau$ , which exhibits

---

<sup>2</sup>Since the value of the weighting function depends on  $x$ , it has to be included in the integrand.

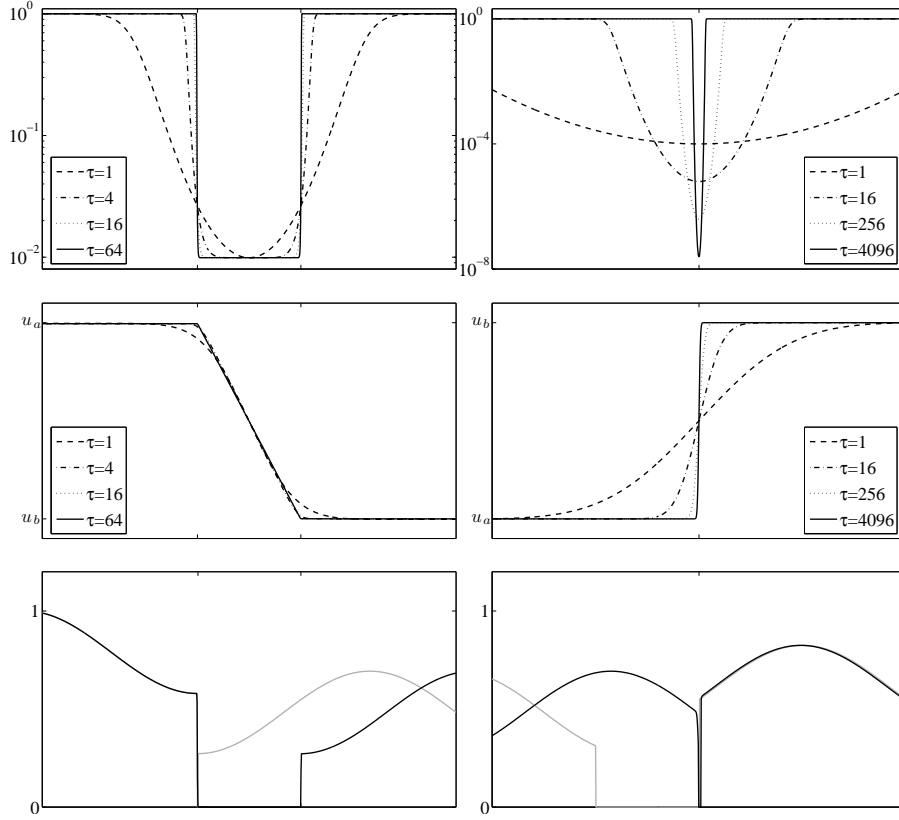


Figure 4.4: Relation between weighting functions  $\alpha$  (top row), displacement functions  $u$  according to (4.3), (centre row), and transformed template images (bottom row) for the ramp case (left) and the step case (right). For better comparison in the bottom row the original template image is added in light grey.

a discontinuity at some position in its limit case, shows an increasing gradient and, therefore, requires a small weighting at the same position in order to be likely a minimum solution to (4.1). Apart from that position, a differing weighting is not required. From Figure 4.4, top and centre right, we observe this property for a Dirac-shaped weighting function,

$$\alpha_\tau(x) = \frac{1}{1 + c_1 \tau \exp(-\tau x^2)}.$$

Applying  $u_\tau$  to a subset of the template image from Figure 4.3 yields a shrinking of the gap interval  $[\delta_l^T, \delta_r^T]$  as shown in Figure 4.4, bottom right.

The second case concerns the enlargement of a gap. We assume a pulling force on the right interval from which we deduce boundary conditions with  $u_a > u_b$ . Choosing a cup-shaped weighting function as for instance

$$\alpha_\tau(x) = \frac{1}{1 + c_2 \exp(-x^{2\tau})},$$

we obtain a displacement which is in the limit  $\tau \rightarrow \infty$  linear within the cup and exhibits a kink at each side. For  $\tau \rightarrow \infty$  the desired ramp function is



obtained (Figure 4.4, top and centre left). When applied to a subset of the same template image than before, we receive an enlargement of the gap around  $\gamma^T$ , see Figure 4.4, bottom left.

We are thus able to choose a specific weighting function such that  $u$  according to (4.2) displays the desired behaviour. It remains to be determined, in which cases  $u$  shall be forced to display one of these behaviours. Further knowledge is required and given by a segmentation.

#### 4.2.2 Segmentation

Here, the aim is to compute a meaningful segmentation of an image, that is, a decomposition of the domain of the image into regions.

Recalling the motivation of an image in Section 2.1, it is considered as an exposure from a scene. In general, different objects in the exposure can be identified. These are either obviously separated from each other (like two ferries on the sea), or *appear* as side-by-side (like a vertebra and an adjacent intervertebral disc in a human body). However, in both cases the objects can be clearly separated from each other and their positions can be collected in various connected sets as for instance for the medical example,

$$\begin{aligned}\Omega^1 &:= \{x \in \Omega \mid x \text{ belongs to the vertebra} \} , \\ \Omega^2 &:= \{x \in \Omega \mid x \text{ belongs to the intervertebral disc} \} .\end{aligned}$$

We assume that these sets are open and, moreover, represent disjoint sets. When taking their closures they have a non-zero intersection (since we assumed the vertebra and the intervertebral disc being adjacent to each other) belonging to neither of them. We include this assumption in the following definition.

**Definition 4.1** (Decomposition). *A decomposition of a domain  $\Omega$  is given by a set*

$$M(\Omega) = \{\Omega^0, \Omega^1, \dots, \Omega^m\}$$

*such that*

1. *each region  $\Omega^i \subset \Omega$ ,  $i = 0, \dots, m$ , is an open set,*
2. *any two regions are disjoint, and*
3. *the union of the closed regions covers  $\bar{\Omega}$ , i.e.  $\bar{\Omega} = \cup_{i=0}^m \bar{\Omega}^i$ .*

*In addition, for  $i = 1, \dots, m$ , each set  $\Omega^i$  is assumed to be connected.*

*Furthermore, by  $\Gamma^{i,j}$  we denote the common boundary of two regions  $\Omega^i, \Omega^j$ ,*

$$\Gamma^{i,j} := \bar{\Omega}^i \cap \bar{\Omega}^j .$$

Note that  $\Omega^0$  is in general not connected and does serve as the background of an image for our application.

Care has to be taken with respect to a decomposition of the interpolated image. For instance, in the medical example, the gap between vertebra and intervertebral disc may not be visible after the acquisition process, and, therefore, just as

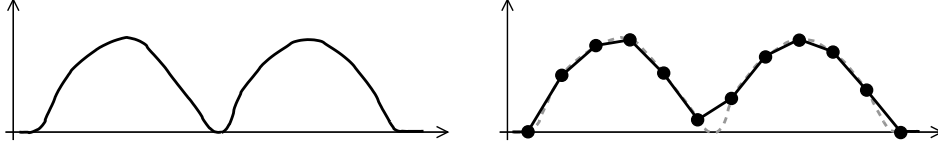


Figure 4.5: Example for an image showing two distinct regions separated by a gap of zero grey-value (left). On the right, a sampling routine has been performed, followed by a linear interpolation of the discrete set of grey-values which results in a vanishing gap. Note that the gap size is chosen smaller than the spacing of the sampling points.

little can it be recognised in the interpolated image, cf. Figure 4.5. To ensure its existence at least in the transformed differentiable image, further a-priori knowledge is required. This topic will be addressed in Chapter 5.

In the remaining part of this section two common approaches for segmentation are described which will be frequently used in Chapter 6.

### Trivial Case

For the case of the one-dimensional problem from Figure 4.3 a segmentation is trivial and consists of a labelling of the known intervals. Thus, for instance for the image  $T$  with  $\Omega = (a, b)$  we have

$$\Omega^1 = (a, \gamma^T), \quad \Omega^2 = (\gamma^T, \delta_l^T), \quad \Omega^3 = (\delta_r^T, b), \quad \text{and} \quad \Omega^0 = (\delta_l^T, \delta_r^T).$$

### Active Contour Approach

Following (XU & PRINCE, 1998) we implemented an active contour approach which is also known as ‘snake approach’. Although, the scheme is applicable to both two- and three-dimensional problems, we describe the two-dimensional case only.

Starting from an initial contour  $p_0 : [0, 1] \rightarrow \mathbb{R}^2$ , a displaced contour  $p$  is searched such that it is smooth and aligns with the gradient of the underlying image. To this end, a minimisation problem is formulated,

$$\int_0^1 \beta_1(p'(x))^2 + \beta_2(p''(x))^2 + E_{\text{ext}}(p(x)) dx \xrightarrow{p} \min, \quad (4.4)$$

where the first two terms of the integral refer to the smoothness (weighted by coefficients  $\beta_1, \beta_2 \in \mathbb{R}^+$ ) of the contour and the last term acts as a driving force. Similarly to the the minimisation of the joint functional (3.16), a minimum solution may be interpreted as a balance between inner forces (i.e., the smoothness) and outer forces (i.e., the driving force).

Having obtained a minimum of (4.4), the displaced contour is usually well aligned to an image structure. By applying, for instance, a region growing scheme afterwards, a region  $\Omega^z$  can be labelled, and, gradually, a decomposition of  $\Omega$  (i.e., a segmentation of the image defined on  $\Omega$ ) can be obtained. For various examples we refer to Chapter 6.

Note that the approach has its drawback in prescribing the same smoothness everywhere on the contour. In many applications, for instance the segmentation of bone structures, parts of the contour are expected to show either a larger curvature (e.g. around the head of a bone) whereas other parts require a small curvature (e.g. along the shaft). Then, a constant choice of the coefficients  $\beta_1$  and  $\beta_2$  may turn out to be inappropriate and, consequently, the approach may benefit from a variable weighting of  $(p')^2$  and  $(p'')^2$  in conjunction with an initial setting according to the expected curvature. Such an extension requires weighting functions and is described, e.g., by XU (1999) or TERZOPOULOS (2003).

### 4.3 Variable Regularisation

In contrast to a regularisation from Chapter 3, a *variable regulariser* exerts a spatially variable influence on the minimisation functional. By a variable influence in particular the regularisation function  $\alpha$  is addressed. Moreover, spatially varying Lamé parameters are needed to support the registration of material-dependent problems.

Note that in the previous section the non-linearity of the boundary value problem (4.2) has been disregarded. Instead, linearity in  $u$  has been assumed and  $u$  could be explicitly stated in terms of  $\alpha$ . However, in general we are faced with a non-linear boundary value problem solved by an iterative scheme, cf. Section 2.4. Here, each time level may require a dedicated weighting function which can be easily seen when taking the zero time level and the final time level: In the first case,  $\alpha$  can be deduced from the template image  $T$ , in the latter case from the reference image  $R$ . Consequently, for an iterative treatment of a non-linear problem,  $\alpha$  has to evolve along with  $u$  and we have to consider  $\alpha(x, u)$  instead of  $\alpha(x)$ . The same argument applies to the Lamé parameters  $\lambda$  and  $\mu$ . In analogy to the notation for the transformed template image we use the abbreviation  $\alpha_u := \alpha(x + u(x))$  for each of the three parameters.

**Remark.** Since in a backward Lagrangian approach a position  $x$  in the coordinate frame of the reference image is mapped to a position  $x + u(x)$  in the template frame, the values  $\alpha_u$ ,  $\lambda_u$  and  $\mu_u$  are to be evaluated with respect to a segmentation of the template image.

Taking instead the values  $\alpha$ ,  $\lambda$ , and  $\mu$  together with a segmentation of the reference image, may look like an appropriate alternative. However, it fails in cases of large segmented overlap regions (for an example, see Figure 6.3). Such regions can be detected by a segmentation of both images, yielding decompositions  $\Omega_T^0, \Omega_T^1, \dots, \Omega_T^m$  and  $\Omega_R^0, \Omega_R^1, \dots, \Omega_R^m$  for the template and the reference image, respectively. Then, an overlap of two different regions is given by  $\Omega_T^i \cap \Omega_R^j$  with  $i \neq j$ . Nevertheless, in the special case an image pair has no non-zero overlap regions, a choice of the values  $\alpha$ ,  $\lambda$ , and  $\mu$  on the basis of a segmentation of the reference image can serve as an appropriate alternative. In general, non-zero overlap regions occur (at least with some background region of an image as  $\Omega_T^i$  or  $\Omega_R^j$ ) and the decomposition  $\{\Omega_R^j\}_j$  in a backward Lagrangian approach leads to an incorrect description of material properties. Thus, with a general applicability in mind we skip the case of choosing  $\alpha$ ,  $\lambda$ , and  $\mu$  from a segmentation

of the reference image and remain at a segmentation of the template image in conjunction with transformed values  $\alpha_u$ ,  $\lambda_u$ ,  $\mu_u$ .

### 4.3.1 Variable Diffusive Regularisation

On the basis of the diffusive regulariser from Section 3.3.2 we define the so-called *variable diffusive regulariser*.

**Definition 4.2** (Variable Diffusive Regularisation). *Given a displacement field  $u \in \mathcal{U}$  and a weighting function  $\alpha \in \mathcal{C}^1(\bar{\Omega}, \mathbb{R}^+)$ , the variable diffusive regulariser is defined as*

$$\mathcal{S}_\alpha^{\text{vardiff}}[u] := \frac{1}{2} \int_{\Omega} \alpha_u(x) \sum_{n=1}^d \|\nabla u_n(x)\|_2^2 dx .$$

The differentiability requirement with respect to  $\alpha$  is obvious by the following lemma.

**Lemma 4.3** (Euler-Lagrange Equation for the Variable Diffusive Regulariser). *The system of Euler-Lagrange equations of  $\mathcal{S}_\alpha^{\text{vardiff}} \rightarrow \min$  is given by*

$$\frac{1}{2} \nabla \alpha_u(x) \sum_{n=1}^d \|\nabla u_n(x)\|_2^2 - \nabla \cdot (\alpha_u(x) \nabla u(x)) = 0 , \quad x \in \Omega . \quad (4.5)$$

*Proof.* Let  $F := \frac{1}{2} \alpha_u \sum_{n=1}^d \|\nabla u_n\|_2^2$ . Then we have  $\nabla_u F = \frac{1}{2} \nabla \alpha_u \sum_{n=1}^d \|\nabla u_n\|_2^2$  and  $\nabla \cdot \nabla_{\nabla u} F = \nabla \cdot (\alpha_u \nabla u)$ . An application of Lemma 3.9 completes the proof. ■

Investigating (4.5) we recognise the divergence term from the Euler-Lagrange equation in the diffusive case, (3.20). The action of the first term in (4.5) is, however, less obvious.

To better understand its contribution we combine the SSD measure (3.17) firstly with the diffusive regulariser (3.19), and secondly with the variable diffusive regulariser. In both cases the resulting initial boundary value problem in its one-dimensional form can be formulated as

$$\begin{aligned} \frac{\partial u(x, t)}{\partial t} &= -[-(\alpha_u u'(x, t))' + \underbrace{[R - T_u]T_u'}_{-f(u(x, t))} - \underbrace{\frac{1}{2} \alpha_u' (u'(x, t))^2}_{g(u(x, t))}] \\ &= (\alpha_u u'(x, t))' + f(u(x, t)) + g(u(x, t)) , \quad x \in \Omega , \quad t \in \mathbb{R}_0^+ , \end{aligned} \quad (4.6)$$

where  $g = 0$  in the first case.

For purpose of illustration, we consider an image pair as depicted in Figure 4.6, left. In the first case  $\alpha$  is chosen constant, in the second case the weighting function  $\alpha$  has been chosen in accordance to Section 4.2: In the interval  $[-1, 1]$ ,  $\alpha(x)$  is chosen small compared to the rest of the image. From a registration of the template onto the reference image we expect a shift of the position 1 to the right leading to an enlargement of the centre interval  $[-1, 1]$ .

We start with the first case, i.e.  $g = 0$ . If  $u$  is constant or even zero, the dominating term in (4.6) is  $f$  which is depicted in Figure 4.6, top right, for

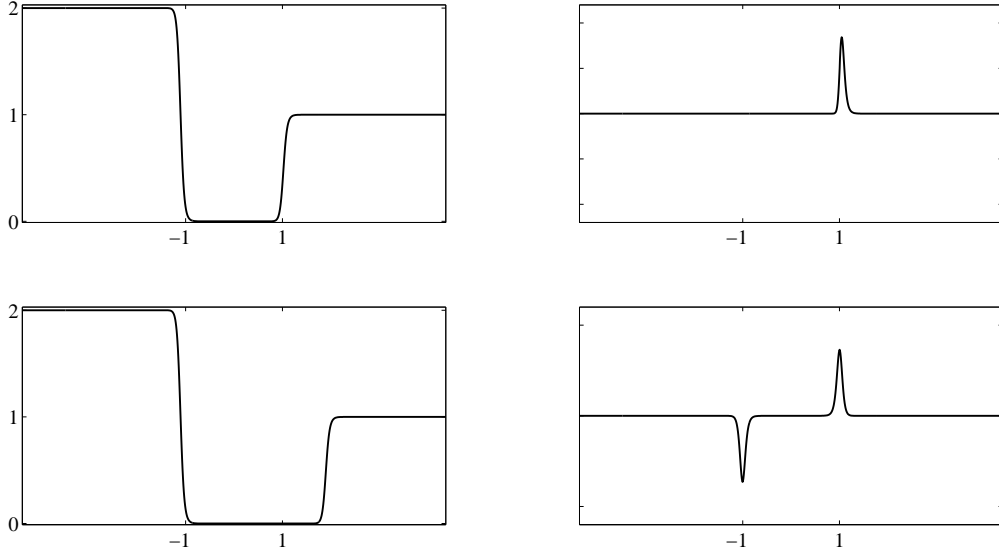


Figure 4.6: For an image pair consisting of template (top left) and reference image (bottom left) the force term resulting from the SSD measure is depicted (top right) together with the spatial derivative of an appropriate weighting function  $\alpha$  (bottom right), see text for further details.

$u = 0$ . The peak force results from the grey-value difference in the image pair and from the gradient in the template image. Note that the sign of this force depends on the signs of  $R - T_u$  and  $T'_u$ . Then, a positive  $f$  leads to an increment in  $u$  and – due to the backward Lagrangian approach – to a transformed template image showing the expected shift to the right.

Now, we investigate the second case with a variable diffusive regulariser. In analogy to  $f$  we will interpret  $g$  as an additional force acting on  $u$ . First of all, we notice that in contrast to  $f$ ,  $g$  is non-zero only if  $u' \neq 0$  (i.e. a displacement has to taken place already). Consequently, in Figure 4.6, bottom right,  $\alpha'$  is depicted instead of  $g$ . However,  $g$  differs from  $\alpha'$  only in magnitude since its sign depends only on  $\alpha'$  and not on  $u'$ . Assuming  $u' \neq 0$ , the action of the additional force can be described as follows, cf. (4.6): A positive value of  $\alpha'$ , and thus of  $g$ , yields a local increase in  $u$  whereas a negative value yields a local decrease in  $u$ . With respect to the considered image pair we conclude an increased shift to the right around the position  $x = 1$  and a possible shift to the left close to the position  $x = -1$ .

This agrees well with the view of the minimiser: An enlargement of a region with a decreased  $\alpha$  offers a better adaption in terms of the similarity measure, with no significant penalisation by the regularising term at the same time, and is therefore preferred.

**Remark.** For the interested reader we note a connection of  $g$  to a similar term arising in the context of level-set problems. AUBERT & KORNPROBST (2002) investigated an initial boundary value problem  $\partial u / \partial t = \alpha'(x)u'(x)$  with a so-called transport term on its right-hand side. For an evolution in time a behaviour as described above can be observed.

We conclude the investigation of the variable diffusive regulariser with the natural boundary condition which is similar to the one for the diffusive regulariser,

$$\alpha_u(x)(\nabla u(x), \mathbf{n}(x)) = 0, \quad x \in \partial\Omega.$$

By setting  $\alpha$  constant, the condition simplifies to (3.21).

### 4.3.2 Variable Elastic Regularisation

The elastic regulariser from Section 3.3.2 equipped with spatially varying parameters yields the so-called *variable elastic regulariser*. Likewise to  $\alpha$  in the variable diffusive regulariser, to determine the Euler-Lagrange equation we need the Lamé parameters to be continuously differentiable.

**Definition 4.4** (Variable Elastic Regularisation). *Given a displacement field  $u \in \mathcal{U}$ , a weighting function  $\alpha \in \mathcal{C}^1(\bar{\Omega}, \mathbb{R}^+)$  as well as material functions  $\lambda \in \mathcal{C}^1(\bar{\Omega}, \mathbb{R}_0^+)$ ,  $\mu \in \mathcal{C}^1(\bar{\Omega}, \mathbb{R}^+)$ , the variable elastic regulariser is defined as*

$$\mathcal{S}_{\alpha, \lambda, \mu}^{\text{varelas}}[u] = \int_{\Omega} \alpha_u(x) \left( \frac{\mu_u(x)}{4} \sum_{i,j=1}^d (\partial_{x_j} u_i(x) + \partial_{x_i} u_j(x))^2 + \frac{\lambda_u(x)}{2} (\nabla \cdot u(x))^2 \right) dx.$$

**Lemma 4.5** (Euler-Lagrange Equation for the Variable Elastic Regulariser). *The system of Euler-Lagrange equations of  $\mathcal{S}_{\alpha, \lambda, \mu}^{\text{varelas}} \longrightarrow \min$  is given by*

$$\begin{aligned} \frac{1}{4} \nabla[\alpha_u \mu_u](x) \sum_{i,j=1}^d (\partial_{x_j} u_i(x) + \partial_{x_i} u_j(x))^2 + \frac{1}{2} \nabla[\alpha_u \lambda_u](x) (\nabla \cdot u(x))^2 \\ - \nabla \cdot [\alpha_u \mu_u (\nabla u + (\nabla u)^T)](x) - \nabla[\alpha_u \lambda_u \nabla \cdot u](x) = 0, \quad x \in \Omega. \end{aligned} \quad (4.7)$$

*Proof.* Let  $F_1 := \frac{\alpha_u \mu_u}{4} \sum_{i,j=1}^d (\partial_{x_j} u_i + \partial_{x_i} u_j)^2$  and let  $F_2 := \frac{\alpha_u \lambda_u}{2} (\nabla \cdot u)^2$ . Then

$$\nabla_u F_1 = \frac{1}{4} \nabla[\alpha_u \mu_u] \sum_{i,j=1}^d (\partial_{x_j} u_i + \partial_{x_i} u_j)^2$$

and

$$\nabla \cdot \nabla_{\nabla u} F_1 = \nabla \cdot [\alpha_u \mu_u (\nabla u + (\nabla u)^T)].$$

Furthermore, we have

$$\nabla_u F_2 = \frac{1}{2} \nabla[\alpha_u \lambda_u] (\nabla \cdot u)^2$$

and

$$\nabla_{\nabla u} F_2 = \alpha_u \lambda_u \text{diag}(\nabla \cdot u),$$

where  $\text{diag}(\nabla \cdot u)$  denotes a diagonal matrix with entries  $\nabla \cdot u$ . Then, for the  $i$ -th component of  $\nabla \cdot \nabla_{\nabla u} F_2$  it follows

$$\begin{aligned} (\nabla \cdot \nabla_{\nabla u} F_2)_i &= \sum_{j=1}^d \partial_{x_j} \left[ \alpha_u \lambda_u (\text{diag}(\nabla \cdot u))_{i,j} \right] \\ &= \partial_{x_i} [\alpha_u \lambda_u \nabla \cdot u] \end{aligned}$$

since  $\text{diag}(\nabla \cdot u)$  has zero entries for  $i \neq j$ . Together with Lemma 3.9 the proposition follows. ■

Likewise to the case of the variable diffusive regulariser, the derived differential equation (4.7) includes terms we are already familiar with: the last two terms correspond to the Euler-Lagrange equation in the elastic case, cf. (3.24). For the first two terms the same argumentation as for the variable diffusive regulariser applies – a positive value of  $\alpha'$  will cause these terms to be positive and, therefore,  $u$  will be locally increased, provided that  $\lambda$  and  $\mu$  are constant. However, for non-constant  $\lambda$  or  $\mu$  an additional local increase or decrease in  $u$  depends on the gradients of  $\alpha\lambda$  and  $\alpha\mu$ .

**Remark.** In order to get some insight in the influence of  $\lambda$  and  $\mu$ , we present an estimation for the two-dimensional case. Taking the first two terms out of (4.7), a simple calculation yields

$$\begin{aligned} \frac{1}{4} \sum_{i,j=1}^2 (\partial_{x_j} u_i + \partial_{x_i} u_j)^2 &\geq (\partial_{x_1} u_1)^2 + (\partial_{x_2} u_2)^2 \\ &\stackrel{*}{\geq} \frac{1}{2} ((\partial_{x_1} u_1)^2 + (\partial_{x_2} u_2)^2) + \partial_{x_1} u_1 \partial_{x_2} u_2 \\ &= \frac{1}{2} (\nabla \cdot u)^2, \end{aligned}$$

where in (\*) Cauchy's inequality is used. Thus, for the direction of the additional force, the influence of  $\mu$  (as a factor of the first term) is larger or equal compared to the one of  $\lambda$  (which is a factor of the second term).

Again, the natural boundary condition,

$$(\alpha_u(x) \mu_u(x) (\nabla u(x) + (\nabla u(x))^T) + \alpha_u(x) \lambda_u(x) \text{diag}(\nabla \cdot u(x)), \mathbf{n}(x)) = 0,$$

where  $x \in \partial\Omega$ , simplifies to the one for the elastic regulariser (3.25) in the case of constant parameters.

### 4.3.3 Link to Boundary Value Problems

Similar to the procedure in the case of constant parameters, a joint Euler-Lagrange equation can be constructed. Note that we collect the terms in (4.5) and (4.7) with a linear dependency on  $u$  or on its derivatives in  $Lu$  and those

with a non-linear dependency in  $g(u)$ . This allocation will become handy in the numerical treatment. Then we obtain

$$Lu(x) = f(u(x)) + g(u(x)) , \quad x \in \Omega , \quad (4.8)$$

with,

1) following from the similarity measure,

$$f(u) := [R - T_u] \nabla T_u , \quad (4.9)$$

and, dependent on the choice of the regulariser,

2a) for the variable diffusive case

$$Lu := -\nabla \cdot (\alpha_u \nabla u) , \quad (4.10)$$

$$g(u) := \frac{1}{2} \nabla \alpha_u \sum_{n=1}^d \|\nabla u_n\|_2^2 , \quad (4.11)$$

2b) and for the variable elastic case

$$Lu := -\nabla \cdot [\alpha_u \mu_u (\nabla u + (\nabla u)^T)] - \nabla [\alpha_u \lambda_u \nabla \cdot u] , \quad (4.12)$$

$$g(u) := \frac{1}{4} \nabla [\alpha_u \mu_u] \sum_{i,j=1}^d (\partial_{x_j} u_i + \partial_{x_i} u_j)^2 + \frac{1}{2} \nabla [\alpha_u \lambda_u] (\nabla \cdot u)^2 . \quad (4.13)$$

Likewise to the case of constant parameters, the Euler-Lagrange equation can be interpreted as an equation describing the balance between inner and outer forces. Here, the regularising term contributes both to the inner forces on the left-hand side of the equation and to the outer ones, included in the right-hand side.

Adding a boundary condition

$$Bu(x) = 0 , \quad x \in \partial\Omega , \quad (4.14)$$

such as

$$B := \text{id} \quad (4.15)$$

for a Dirichlet type condition or

$$B := \partial / \partial \mathbf{n} \quad (4.16)$$

for a Neumann type condition, (4.8) and (4.14) together form a boundary value problem.

In line of Section 3.3.3 an initial boundary value problem results,

$$\begin{aligned} \frac{\partial u(x, t)}{\partial t} &= -[Lu(x, t) - f(u(x, t)) - g(u(x, t))] , & x \in \Omega , \quad t \in \mathbb{R}_0^+ , \\ u(x, 0) &= u^{(0)}(x) , & x \in \Omega , \\ Bu(x, t) &= q(x, t) , & x \in \partial\Omega , \quad t \in \mathbb{R}_0^+ \end{aligned} \quad (4.17)$$

with  $u^{(0)} : \bar{\Omega} \rightarrow \mathbb{R}^d$  as a smooth initial function.

In order to discretise this system, various difference formulas can be derived.



**Example 4.6** (Discretisation of (4.10)). As an example we consider the term  $\nabla \cdot (\alpha_u \nabla u)$  from the variable diffusive case which can be discretised either as

$$\begin{pmatrix} \partial_1^\pm [\alpha_U \partial_1^\pm U_1] + \partial_2^\pm [\alpha_U \partial_2^\pm U_1] \\ \partial_1^\pm [\alpha_U \partial_1^\pm U_2] + \partial_2^\pm [\alpha_U \partial_2^\pm U_2] \end{pmatrix} \quad (4.18)$$

or, after applying the chain rule, as

$$\begin{pmatrix} \partial_1^\pm \alpha_U \partial_1^a \partial_1^\pm U_1 + \alpha_U \partial_{11}^\pm U_1 + \partial_2^\pm \alpha_U \partial_2^a \partial_2^\pm U_1 + \alpha_U \partial_{22}^\pm U_1 \\ \partial_1^\pm \alpha_U \partial_1^a \partial_1^\pm U_2 + \alpha_U \partial_{11}^\pm U_2 + \partial_2^\pm \alpha_U \partial_2^a \partial_2^\pm U_2 + \alpha_U \partial_{22}^\pm U_2 \end{pmatrix}. \quad (4.19)$$

With a computationally efficient numerical treatment of (4.17) in mind, the symmetry of the matrix of the resulting system of equations is a property which is highly desirable.

In the following section this example will be revisited to discuss advantages as well as disadvantages of the discretisations above.

As before, we will follow the scheme

$$\text{discretised operator} \Rightarrow \text{stencil notation} \Rightarrow \text{system matrix}$$

and deduce the symmetry from the stencil instead from the discretised operator. However, the stencil notation used so far does not include a dependency on the spatial position. Since in (4.10) or (4.12) the operator  $L$  depends itself on  $u$ , the stencil is not constant any more and we introduce the notation of a *variable stencil*.

#### 4.3.4 Variable Stencil Notation

In analogy to Section 2.5 we define a variable stencil, i.e., a stencil whose entries depend on the spatial position. To this end let  $(i, j)$  denote a grid point of the discretised domain  $\Omega_h$ . We recall the matrix  $G(U_n^{i,j,l})$  of discrete values around a centre  $U_n^{i,j,l}$  and define a variable stencil as follows.

**Definition 4.7** (Variable Stencil). *A variable stencil (of size 1) around the centre  $(i, j) \in \Omega_h$  is given by a matrix  $S$  with entries  $s^{\kappa_1, \kappa_2}(i, j)$  and indices  $\kappa_1, \kappa_2 \in \{-1, 0, 1\}$ , such that*

$$S := \begin{bmatrix} s^{-1, -1}(i, j) & s^{-1, 0}(i, j) & s^{-1, 1}(i, j) \\ s^{0, -1}(i, j) & s^{0, 0}(i, j) & s^{0, 1}(i, j) \\ s^{1, -1}(i, j) & s^{1, 0}(i, j) & s^{1, 1}(i, j) \end{bmatrix}.$$

Then the convolution of  $G(U_n^{i,j,l})$  with a variable stencil is given by

$$S * G(U_n^{i,j,l}) = \sum_{\kappa_1, \kappa_2 = -1}^1 s^{\kappa_1, \kappa_2}(i, j) g^{\kappa_1, \kappa_2}. \quad (4.20)$$

**Example 4.8** (Discretisation of (4.10) Revisited). We return to the discretisations from (4.18) and (4.19) and investigate their notation in stencil form. For

ease of presentation we assume an isotropic grid spacing, i.e.  $h_1 = h_2 =: h$ , and comment on the first component only. Then we have

$$\partial_1^\pm [\alpha_U^{i,j,l} \partial_1^\pm U_1^{i,j,l}] + \partial_2^\pm [\alpha_U^{i,j,l} \partial_2^\pm U_1^{i,j,l}] = S * G(U_1^{i,j,l})$$

with

$$S := \frac{1}{h^2} \begin{bmatrix} 0 & \alpha_U^{i-\frac{1}{2},j,l} & 0 \\ \alpha_U^{i,j-\frac{1}{2},l} & -\sum_{\kappa_1, \kappa_2=0}^1 \alpha_U^{i-\frac{1}{2}+\kappa_1, j-\frac{1}{2}+\kappa_2, l} & \alpha_U^{i,j+\frac{1}{2},l} \\ 0 & \alpha_U^{i+\frac{1}{2},j,l} & 0 \end{bmatrix}, \quad (4.21)$$

and

$$\partial_1^\pm \alpha_U^{i,j,l} \partial_1^a \partial_1^\pm U_1 + \alpha_U^{i,j,l} \partial_{11}^\pm U_1 + \partial_2^\pm \alpha_U^{i,j,l} \partial_2^a \partial_2^\pm U_1 + \alpha_U^{i,j,l} \partial_{22}^\pm U_1 = S * G(U_1^{i,j,l})$$

with

$$S := \frac{1}{h^2} \begin{bmatrix} 0 & \frac{-\alpha_U^{i-\frac{1}{2},j,l} + 2\alpha_U^{i,j,l} + \alpha_U^{i+\frac{1}{2},j,l}}{2} & 0 \\ \frac{-\alpha_U^{i,j-\frac{1}{2},l} + 2\alpha_U^{i,j,l} + \alpha_U^{i,j+\frac{1}{2},l}}{2} & -4\alpha_U^{i,j,l} & \frac{\alpha_U^{i,j-\frac{1}{2},l} + 2\alpha_U^{i,j,l} - \alpha_U^{i,j+\frac{1}{2},l}}{2} \\ 0 & \frac{\alpha_U^{i-\frac{1}{2},j,l} + 2\alpha_U^{i,j,l} - \alpha_U^{i+\frac{1}{2},j,l}}{2} & 0 \end{bmatrix}, \quad (4.22)$$

respectively. From a closer look at the stencil entries, we may suspect the latter stencil to be non-symmetric. However, the symmetry property for variable stencils needs to be established first.

In extension of Definition 2.17 we define the transpose of a variable stencil.

**Definition 4.9** (Transpose of a Variable Stencil). *Given variable stencils  $S_1$  and  $S_2$  with entries  $s_1^{\kappa_1, \kappa_2}(i, j)$  and  $s_2^{\kappa_1, \kappa_2}(i, j)$ ,  $\kappa_1, \kappa_2 \in \{-1, 0, 1\}$ ,  $S_2$  is transposed to  $S_1$  if*

$$s_1^{\kappa_1, \kappa_2}(i - \frac{\kappa_1}{2}, j - \frac{\kappa_2}{2}) = s_2^{-\kappa_1, -\kappa_2}(i + \frac{\kappa_1}{2}, j + \frac{\kappa_2}{2}), \quad \kappa_1, \kappa_2 \in \{-1, 0, 1\}.$$

Again, the transpose of a stencil is denoted by  $\mathbb{T}$ .

In the following definition we make use of a block stencil. It has been already introduced in Definition 2.16 for non-variable stencils. Its application to variable stencils is straightforward.

**Definition 4.10** ((Block-)Symmetric Variable (Block) Stencil). *Given a variable stencil  $S$  with entries  $s^{\kappa_1, \kappa_2}(i, j)$ ,  $\kappa_1, \kappa_2 \in \{-1, 0, 1\}$ ,  $S$  is called symmetric if it is equal to its transpose, i.e. if  $S = S^\mathbb{T}$ .*

*Furthermore, a variable block stencil  $\mathbb{S} = (S_{\omega_1, \omega_2})_{\omega_1, \omega_2}$  is called block-symmetric if  $S_{\omega_1, \omega_2} = S_{\omega_2, \omega_1}^\mathbb{T}$  holds for all  $\omega_1, \omega_2 \in \{1, 2\}$ .*

Returning to Example 4.8 we observe that the variable stencil (4.21) is symmetric whereas the one in (4.22) is not. For the discretisation of the remaining terms of the initial boundary value problem (4.17) we keep this observation in mind to ensure the symmetry of all occurring stencils. After the assembly of the

system of equations to be solved, the last step will be to prove the equivalence of stencil symmetry and matrix symmetry.

Before, we note that for the variable stencils boundary conditions have been disregarded so far. As a matter of fact, boundary conditions apply if the convolution in (4.20) is applied to a grid point for which a neighbouring grid point belongs to  $\partial\Omega_h$ . However, the argumentation from Section 2.5 can be applied equally to the present case and it can be concluded that the (block-)symmetry condition is not affected by boundary conditions of either Dirichlet or Neumann type.

## 4.4 Discretisation

For a discretisation of (4.17) we use the framework developed in Section 3.4, now with  $g(u)$  handled in the same way as  $f(u)$ . The ‘transformed’ parameter functions  $\alpha_U$ ,  $\lambda_U$ , and  $\mu_U$  are defined in analogy to  $T_U$ .

As in Section 3.4 we have  $\Omega = (0, 1)^2$ . The section starts with the description of the discrete equations and proceeds by presenting the corresponding stencils.

**Lemma 4.11.** *Given the IBVP 4.17 with abbreviations as in (4.9)–(4.16), a discretisation with a local order of accuracy of  $\mathcal{O}(h^2 + k)$  is given by*

$$\begin{aligned} (\text{id}_h + kL_{h,k}^{l+1})U^{i,j,l+1} &= U^{i,j,l} + kf_h U^{i,j,l} + kg_{h,k} U^{i,j,l}, & (i,j) \in \Omega_h, \quad l \in \mathbb{N}_0, \\ U^{i,j,0} &= u^{(0)}(x_i, y_j), & (i,j) \in \bar{\Omega}_h, \\ B_h U^{i,j,l+1} &= 0, & (i,j) \in \partial\Omega_h, \quad l \in \mathbb{N}_0, \end{aligned} \quad (4.23)$$

where (note that due to space limitations the terms  $U^{i,j,l}$ ,  $U_1^{i,j,l}$ ,  $U_2^{i,j,l}$ ,  $\alpha_U^{i,j,l}$ ,  $\lambda_U^{i,j,l}$ , and  $\mu_U^{i,j,l}$  are abbreviated by  $U$ ,  $U_1$ ,  $U_2$ ,  $\alpha$ ,  $\lambda$ , and  $\mu$ , respectively)

1)  $f_h$  refers to the discretised similarity measure as in Lemma 3.17,

2a) for the variable diffusive case,  $L_{h,k}^{l+1}$  refers to the discretised operator

$$L_{h,k}^{l+1} = - \begin{pmatrix} \partial_1^\pm[\alpha\partial_1^\pm] + \partial_2^\pm[\alpha\partial_2^\pm] & 0 \\ 0 & \partial_1^\pm[\alpha\partial_1^\pm] + \partial_2^\pm[\alpha\partial_2^\pm] \end{pmatrix} \quad (4.24)$$

and  $g_{h,k}$  is given by

$$g_{h,k}U = - \frac{1}{2} \begin{pmatrix} \partial_1^\pm\alpha\{(\partial_1^\pm U_1)^2 + (\partial_2^\pm U_1)^2 + (\partial_1^\pm U_2)^2 + (\partial_2^\pm U_2)^2\} \\ \partial_2^\pm\alpha\{(\partial_1^\pm U_1)^2 + (\partial_2^\pm U_1)^2 + (\partial_1^\pm U_2)^2 + (\partial_2^\pm U_2)^2\} \end{pmatrix}, \quad (4.25)$$

2b) for the variable elastic case,  $L_{h,k}^{l+1}$  refers to the discretised operator

$$L_{h,k}^{l+1} = - \begin{pmatrix} \partial_1^\pm[\alpha(\lambda + 2\mu)\partial_1^\pm] + \partial_2^\pm[\alpha\mu\partial_2^\pm] & \partial_2^\pm\partial_2^\pm[\alpha\mu\partial_1^\pm\partial_1^\pm] + \partial_1^\pm\partial_1^\pm[\alpha\lambda\partial_2^\pm\partial_2^\pm] \\ \partial_1^\pm\partial_1^\pm[\alpha\mu\partial_2^\pm\partial_2^\pm] + \partial_2^\pm\partial_2^\pm[\alpha\lambda\partial_1^\pm\partial_1^\pm] & \partial_1^\pm[\alpha\mu\partial_1^\pm] + \partial_2^\pm[\alpha(\lambda + 2\mu)\partial_2^\pm] \end{pmatrix} \quad (4.26)$$

and  $g_{h,k}$  is given by

$$g_{h,k}U = -\frac{1}{4} \begin{pmatrix} \partial_1^\pm[\alpha\mu]\{4(\partial_1^\pm U_1)^2 + 2(\partial_1^\pm U_2 + \partial_2^\pm U_1)^2 + 4(\partial_2^\pm U_2)^2\} \\ \partial_2^\pm[\alpha\mu]\{4(\partial_1^\pm U_1)^2 + 2(\partial_1^\pm U_2 + \partial_2^\pm U_1)^2 + 4(\partial_2^\pm U_2)^2\} \end{pmatrix} \quad (4.27)$$

$$-\frac{1}{2} \begin{pmatrix} \partial_1^\pm[\alpha\lambda](\partial_1^\pm U_1 + \partial_2^\pm U_2)^2 \\ \partial_2^\pm[\alpha\lambda](\partial_1^\pm U_1 + \partial_2^\pm U_2)^2 \end{pmatrix}, \quad (4.28)$$

3)  $B_h$  refers to the boundary operators as in Lemma 3.17,

respectively.

*Proof.* The derivation of (2a) and (2b) is straightforward from (4.10)–(4.13) by using solely second-order difference quotients as introduced in (2.15).

Then, in analogy to Lemma 3.17, an application of Lemma 2.12 (here with  $f_h U^{i,j,l} + g_{h,k} U^{i,j,l}$  instead of  $f_h U^{i,j,l}$ ) yields (4.23) as a consistent discretisation of (4.17) with a LOA of  $\mathcal{O}(h^2 + k)$  which completes the proof. ■

The following corollary states the discretised operator  $L_{h,k}$  in stencil notation. Due to space limitations, the transformed parameter functions  $\alpha_U$ ,  $\lambda_U$ , and  $\mu_U$  are abbreviated by  $\alpha$ ,  $\lambda$ , and  $\mu$ , respectively. Moreover, in each superindex the time level  $l$  is omitted.

**Corollary 4.12.** *Given the discretised operator  $\text{id}_h + kL_{h,k}$  with  $L_{h,k}$  as in (4.24) and (4.26), its stencil notation is given by*

$$\mathbb{S} = \begin{pmatrix} \begin{bmatrix} 0 & 0 & 0 \\ 0 & 1 & 0 \\ 0 & 0 & 0 \end{bmatrix} \\ \begin{bmatrix} 0 & 0 & 0 \\ 0 & 1 & 0 \\ 0 & 0 & 0 \end{bmatrix} \end{pmatrix} - k \begin{pmatrix} S_{1,1} & S_{1,2} \\ S_{2,1} & S_{2,2} \end{pmatrix}$$

with, in the variable diffusive case,

$$S_{1,1} = \begin{bmatrix} 0 & h_1^{-2}[\alpha]^{i-\frac{1}{2},j} & 0 \\ h_2^{-2}[\alpha]^{i,j-\frac{1}{2}} & \Sigma & h_2^{-2}[\alpha]^{i,j+\frac{1}{2}} \\ 0 & h_1^{-2}[\alpha]^{i+\frac{1}{2},j} & 0 \end{bmatrix}, \quad (4.29)$$

$$S_{2,2} = S_{1,1},$$

$$S_{1,2} = S_{2,1} = 0,$$

and

$$\Sigma := -\frac{[\alpha]^{i-\frac{1}{2},j} + [\alpha]^{i+\frac{1}{2},j}}{h_1^2} - \frac{[\alpha]^{i,j-\frac{1}{2}} + [\alpha]^{i,j+\frac{1}{2}}}{h_2^2},$$

and with, in the variable elastic case,

$$S_{1,1} = \begin{bmatrix} 0 & h_1^{-2}[\alpha(\lambda + 2\mu)]^{i-\frac{1}{2},j} & 0 \\ h_2^{-2}[\alpha\mu]^{i,j-\frac{1}{2}} & \Sigma_1 & h_2^{-2}[\alpha\mu]^{i,j+\frac{1}{2}} \\ 0 & h_1^{-2}[\alpha(\lambda + 2\mu)]^{i+\frac{1}{2},j} & 0 \end{bmatrix},$$

$$S_{2,2} = \begin{bmatrix} 0 & h_1^{-2}[\alpha\mu]^{i-\frac{1}{2},j} & 0 \\ h_2^{-2}[\alpha(\lambda + 2\mu)]^{i,j-\frac{1}{2}} & \Sigma_2 & h_2^{-2}[\alpha(\lambda + 2\mu)]^{i,j+\frac{1}{2}} \\ 0 & h_1^{-2}[\alpha\mu]^{i+\frac{1}{2},j} & 0 \end{bmatrix}, \quad (4.30)$$

$$S_{1,2} = \frac{1}{4h_1h_2} \begin{bmatrix} [\alpha\lambda]^{i-1,j} + [\alpha\mu]^{i,j-1} & 0 & -[\alpha\lambda]^{i-1,j} - [\alpha\mu]^{i,j+1} \\ 0 & 0 & 0 \\ -[\alpha\lambda]^{i+1,j} - [\alpha\mu]^{i,j-1} & 0 & [\alpha\lambda]^{i+1,j} + [\alpha\mu]^{i,j+1} \end{bmatrix},$$

$$S_{2,1} = \frac{1}{4h_1h_2} \begin{bmatrix} [\alpha\lambda]^{i,j-1} + [\alpha\mu]^{i-1,j} & 0 & -[\alpha\lambda]^{i,j+1} - [\alpha\mu]^{i-1,j} \\ 0 & 0 & 0 \\ -[\alpha\lambda]^{i,j-1} - [\alpha\mu]^{i+1,j} & 0 & [\alpha\lambda]^{i,j+1} + [\alpha\mu]^{i+1,j} \end{bmatrix},$$

and

$$\Sigma_1 := -\frac{[\alpha(\lambda + 2\mu)]^{i-\frac{1}{2},j} + [\alpha(\lambda + 2\mu)]^{i+\frac{1}{2},j}}{h_1^2} - \frac{[\alpha\mu]^{i,j-\frac{1}{2}} + [\alpha\mu]^{i,j+\frac{1}{2}}}{h_2^2},$$

$$\Sigma_2 := -\frac{[\alpha\mu]^{i-\frac{1}{2},j} + [\alpha\mu]^{i+\frac{1}{2},j}}{h_1^2} - \frac{[\alpha(\lambda + 2\mu)]^{i,j-\frac{1}{2}} + [\alpha(\lambda + 2\mu)]^{i,j+\frac{1}{2}}}{h_2^2}.$$

Furthermore, these variable block stencils are block-symmetric in the sense of Definition 4.10.

*Proof.* Follows from Sections 2.5 and 4.3.4. ■

The following remark provides an interpretation of the spatial dependencies in the stencils above.

**Remark.** For a better understanding of the stencils from (4.29) and (4.30), Figure 4.7 provides a visualisation of the dependence schemes.

For the stencil entries in the variable diffusive case, a symmetric dependence on the spatial positions of  $\alpha_U$ ,  $\lambda_U$ , and  $\mu_U$  can be observed, cf. Figure 4.7, left. Here,  $\alpha_U$  is discretised on semi-inter-grid positions (i.e., in one component the position coincides with the grid, in the other component the position is in between the grid) and each of its discretised values serves as coefficient of  $U_1$  and  $U_2$  on the two nearest grid points (indicated by dashed ellipses).

For the variable elastic case, the same situation holds for  $\alpha_U$  and  $\mu_U$  included in the stencils  $S_{1,1}$  and  $S_{2,2}$ . In contrast, the dependence scheme for  $\lambda_U$  is asymmetric and in  $S_{1,1}$  ( $S_{2,2}$ )  $\lambda_U$  is a coefficient of  $U_1$  ( $U_2$ ) only (depicted in Figure 4.7, center left). Turning our attention towards the stencils  $S_{1,2}$  and  $S_{2,1}$  we observe discretised values on grid positions only. Here,  $\alpha_U$  is independent of

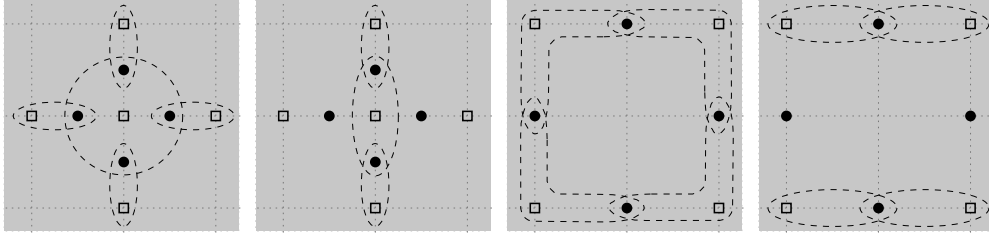


Figure 4.7: Dependence schemes for stencils in the variable diffusive or elastic case. Positions of  $U$  are marked by squares, positions of the parameters by filled circles. See text for further details.

the component and each of its discretised values serves as coefficient of  $U_1$  and  $U_2$  on the adjacent edge positions (shown in Figure 4.7, center right). For  $\lambda_U$  in  $S_{1,2}$  and for  $\mu_U$  in  $S_{2,1}$  the dependence scheme is restricted to the top and the bottom edge positions as is apparent from Figure 4.7, right. Similarly, the dependence scheme for  $\mu_U$  in  $S_{1,2}$  and the one for  $\lambda_U$  in  $S_{2,1}$  show their action on the left and right edge positions (not shown).

With a numerical solution of the discretised initial boundary value problem in mind we employ the grid point mapping  $\xi$  from (2.28) and assemble a system

$$\begin{aligned} \mathbf{A}^{(l+1)} \mathbf{U}^{(l+1)} &= \mathbf{U}^{(l)} + k\mathbf{F}^{(l)} + k\mathbf{G}^{(l)}, \quad l \in \mathbb{N}^0, \\ \mathbf{U}^{(0)} &= 0. \end{aligned} \quad (4.31)$$

Here,  $\mathbf{F}^{(l)}$  and  $\mathbf{G}^{(l)}$  result from (3.35), (4.25), and (4.28) using the grid point mapping. For the block matrix

$$\mathbf{A}^{(l+1)} = \begin{pmatrix} \mathbf{A}_{1,1} & \mathbf{A}_{1,2} \\ \mathbf{A}_{2,1} & \mathbf{A}_{2,2} \end{pmatrix}$$

we assume the discretised domain  $\Omega_h$  to consist of  $N_1 \times N_2$  grid points such that each matrix<sup>3</sup>  $\mathbf{A}_{\omega_1, \omega_2} = (\mathbf{a}_{\omega_1, \omega_2}^{i,j})_{i,j \in \mathbb{N}_{\leq N_1 N_2}}$ ,  $\omega_1, \omega_2 \in \mathbb{N}_{\leq 2}$ , can be constructed from the variable block stencil

$$\mathbb{S} = \begin{pmatrix} S_{1,1} & S_{1,2} \\ S_{2,1} & S_{2,2} \end{pmatrix}$$

by the mapping

$$\mathbf{a}_{\omega_1, \omega_2}^{\xi(i,j), \xi(i+\kappa_1, j+\kappa_2)} := s_{\omega_1, \omega_2}^{\kappa_1, \kappa_2}(i, j) \quad (4.32)$$

with  $i \in \mathbb{N}_{\leq n_1}$ ,  $j \in \mathbb{N}_{\leq n_2}$ , and  $\kappa_1, \kappa_2 \in \{-1, 0, 1\}$  provided that  $i + \kappa_1 \in \mathbb{N}_{\leq n_1}$  and  $j + \kappa_2 \in \mathbb{N}_{\leq n_2}$ . Here, the variable block stencil corresponds either to the variable diffusive regulariser or to the variable elastic regulariser.

Boundary conditions of Dirichlet type are automatically incorporated (see Section 2.5 for further details), those of Neumann type require an update of the

<sup>3</sup>Note that, as for the stencils from Corollary 4.12, the time level is omitted due to space limitations.

diagonal elements of  $\mathbf{A}_{\omega_1, \omega_2}$  for which  $i \in \{1, N_1\}$  or  $j \in \{1, N_2\}$ ,

$$\mathbf{a}_{\omega_1, \omega_2}^{\xi(i,j), \xi(i,j)} := \begin{cases} \sum_{\kappa_1 + \kappa_2 \leq 0} s_{\omega_1, \omega_2}^{\kappa_1, \kappa_2}(i, j) & , (i, j) \in \{(1, 1), (N_1, N_2)\} \\ \sum_{\kappa_2 = -1}^1 s_{\omega_1, \omega_2}^{\kappa_1, \kappa_2}(i, j) + s_{\omega_1, \omega_2}^{0,0}(i, j) & , i \in \{1, N_1\}, j \notin \{1, N_2\} \\ \sum_{\kappa_2 \geq \kappa_1} s_{\omega_1, \omega_2}^{\kappa_1, \kappa_2}(i, j) & , (i, j) \in \{(1, N_2), (N_1, 1)\} \\ \sum_{\kappa_1 = -1}^1 s_{\omega_1, \omega_2}^{\kappa_1, 1}(i, j) + s_{\omega_1, \omega_2}^{0,0}(i, j) & , i \notin \{1, N_1\}, j \in \{1, N_2\} \end{cases} \quad (4.33)$$

Then,  $\mathbf{A}^{(l+1)}$  includes both the discrete operator  $id_h + kL_{h,k}^{(l+1)}$  and the applicable boundary conditions. By the corollary above we know that  $\mathbb{S}$  is block-symmetric. The following lemma generalises Lemma 2.20 and will close the gap between the symmetry of  $\mathbf{A}^{(l+1)}$  and the block-symmetry of  $\mathbb{S}$ .

**Lemma 4.13** (Symmetry of the System Matrix  $\mathbf{A}$ ). *Let  $\omega_1, \omega_2 \in \mathbb{N}_{\leq 2}$ , let  $\mathbb{S} = (S_{\omega_1, \omega_2})_{\omega_1, \omega_2}$  denote a variable block stencil of size 2, and let  $\mathbf{A}$  denote a block matrix with matrices  $\mathbf{A}_{\omega_1, \omega_2}$  defined via (4.32) in the case of Dirichlet boundary conditions and additionally via (4.33) in the case of Neumann boundary conditions.*

*Then  $\mathbf{A}$  is symmetric if and only if  $\mathbb{S}$  is block-symmetric.*

*Proof.* First, we assume that  $\mathbb{S}$  is block-symmetric and establish the symmetry of  $\mathbf{A}$ .

Due to the block-symmetry, the equalities  $S_{1,1} = (S_{1,1})^\top$ ,  $S_{2,2} = (S_{2,2})^\top$ , and  $S_{1,2} = (S_{2,1})^\top$  follow from Definition 4.10. We start by showing the symmetry of  $\mathbf{A}_{1,1}$  and  $\mathbf{A}_{2,2}$ , and disregard, in the first instance, the boundary stencils.

Let  $i \in \mathbb{N}_{\leq N_1}$ ,  $j \in \mathbb{N}_{\leq N_2}$ . In addition, let  $\kappa_1, \kappa_2 \in \{-1, 0, 1\}$  provided that  $i + \kappa_1 \in \mathbb{N}_{\leq N_1}$  and  $j + \kappa_2 \in \mathbb{N}_{\leq N_2}$ . Then we can express any non-zero entry of  $\mathbf{A}_{1,1}$  by

$$\mathbf{a}_{1,1}^{\xi(i,j), \xi(i+\kappa_1, j+\kappa_2)} = s_{1,1}^{\kappa_1, \kappa_2}(i, j)$$

which is equal to  $s_{1,1}^{-\kappa_1, -\kappa_2}(i + \kappa_1, j + \kappa_2)$  due to  $S_{1,1} = (S_{1,1})^\top$ . We choose  $\hat{i}, \hat{j}$  such that  $\hat{i}, \hat{i} - \kappa_1 \in \mathbb{N}_{\leq N_1}$  and  $\hat{j}, \hat{j} - \kappa_2 \in \mathbb{N}_{\leq N_2}$ . Then the entry  $\mathbf{a}_{1,1}^{\xi(\hat{i}, \hat{j}), \xi(\hat{i} - \kappa_1, \hat{j} - \kappa_2)}$  exists and, moreover, is given by  $s_{1,1}^{-\kappa_1, -\kappa_2}(\hat{i}, \hat{j})$ . Finally we choose a coordinate transformation

$$\hat{i} = i + \kappa_1, \quad \hat{j} = j + \kappa_2$$

and end up with the equality

$$\begin{aligned} \mathbf{a}_{1,1}^{\xi(i,j), \xi(i+\kappa_1, j+\kappa_2)} &= s_{1,1}^{\kappa_1, \kappa_2}(i, j) \\ &\stackrel{*}{=} s_{1,1}^{-\kappa_1, -\kappa_2}(i + \kappa_1, j + \kappa_2) \\ &= s_{1,1}^{-\kappa_1, -\kappa_2}(\hat{i}, \hat{j}) \\ &= \mathbf{a}_{1,1}^{\xi(\hat{i}, \hat{j}), \xi(\hat{i} - \kappa_1, \hat{j} - \kappa_2)} \\ &= \mathbf{a}_{1,1}^{\xi(i+\kappa_1, j+\kappa_2), \xi(i, j)} \end{aligned} \quad (4.34)$$

showing the symmetry of  $\mathbf{A}_{1,1}$ . Note that the use of the stencil symmetry is marked by  $*$ . Coming back to the boundary stencils, these do not change the conclusion: In the Dirichlet case the argumentation above fits as well, in the

Neumann case for  $\kappa_1 = \kappa_2 = 0$  the stencil terms in (4.34) are replaced by an appropriate term from (4.33) which does not change the overall equality. The symmetry of  $\mathbf{A}_{2,2}$  can be proven analogously.

We are left with the symmetry of any non-zero entry in  $\mathbf{A}_{1,2}$  and the corresponding entry in  $\mathbf{A}_{2,1}$ . Let  $i, j, \kappa_1, \kappa_2$  be as above. It remains to show that

$$\mathbf{a}_{1,2}^{\xi(i,j),\xi(i+\kappa_1,j+\kappa_2)} \stackrel{!}{=} \mathbf{a}_{2,1}^{\xi(i+\kappa_1,j+\kappa_2),\xi(i,j)}.$$

Here, the argumentation from the case  $\mathbf{A}_{1,1}$  can be reused and we end up, disregarding any boundary stencils in the first instance, with

$$\begin{aligned} \mathbf{a}_{1,2}^{\xi(i,j),\xi(i+\kappa_1,j+\kappa_2)} &= s_{1,2}^{\kappa_1,\kappa_2}(i,j) \\ &\stackrel{*}{=} s_{2,1}^{-\kappa_1,-\kappa_2}(i+\kappa_1,j+\kappa_2) \\ &= s_{2,1}^{-\kappa_1,-\kappa_2}(\hat{i},\hat{j}) \\ &= \mathbf{a}_{2,1}^{\xi(\hat{i},\hat{j}),\xi(\hat{i}-\kappa_1,\hat{j}-\kappa_2)} \\ &= \mathbf{a}_{2,1}^{\xi(i+\kappa_1,j+\kappa_2),\xi(i,j)} \end{aligned} \tag{4.35}$$

where in  $*$  the block-symmetry of  $\mathbb{S}$  has been employed. Likewise to the case  $\mathbf{A}_{1,1}$ , boundary stencils from a Dirichlet condition do not change the conclusion. In the Neumann case for  $\kappa_1 = \kappa_2 = 0$ , any stencil entry in (4.35) is replaced by appropriate terms from (4.33) which does not change the overall equality. Thus,  $\mathbf{A}$  is symmetric.

We proceed by assuming that  $\mathbf{A}$  is symmetric and establish the symmetry of the block stencil.

From the construction of  $\mathbf{A}$  we know that each non-zero entry is given by (4.32) and additionally by (4.33) for Neumann boundary conditions.

Let  $i \in \mathbb{N}_{\leq N_1}$ ,  $j \in \mathbb{N}_{\leq N_2}$ . In addition, let  $\kappa_1, \kappa_2 \in \{-1, 0, 1\}$  provided that  $i + \kappa_1 \in \mathbb{N}_{\leq N_1}$  and  $j + \kappa_2 \in \mathbb{N}_{\leq N_2}$ . From the symmetry of  $\mathbf{A}$  and thus from the one of  $\mathbf{A}_{1,1}$  we know  $\mathbf{a}_{1,1}^{\xi(i,j),\xi(i+\kappa_1,j+\kappa_2)} = \mathbf{a}_{1,1}^{\xi(i+\kappa_1,j+\kappa_2),\xi(i,j)}$ . Then, (4.34) and in particular the equality marked by  $*$  holds. Since Neumann boundary conditions only affect matrix entries on the diagonal (i.e.,  $\kappa_1 = \kappa_2 = 0$ ), (4.34) still holds. From  $*$ , it is straightforward to establish that the stencil  $S_{1,1}$  is symmetric. The symmetry of the stencil  $S_{2,2}$  can be obtained analogously.

The final task is to show the equivalence  $S_{1,2} = (S_{2,1})^\top$ . Since  $\mathbf{A}$  is symmetric, the entries  $\mathbf{a}_{1,2}^{\xi(i,j),\xi(i+\kappa_1,j+\kappa_2)}$  and  $\mathbf{a}_{2,1}^{\xi(i+\kappa_1,j+\kappa_2),\xi(i,j)}$  are equal. Then, (4.35) and in particular the equality marked by  $*$  follow. As before, the conclusion holds for Neumann boundary conditions as well. Thus  $S_{1,2} = (S_{2,1})^\top$  and the block stencil  $\mathbb{S}$  is block-symmetric. ■

Returning to the assembled system (4.31) we can conclude that the block matrix  $\mathbf{A}^{(l+1)}$  is symmetric. Furthermore, the lemma shows that the symmetry is not affected by the incorporation of the discrete boundary conditions from (3.38) or (3.39).

A last time we recall the introductory discretisation example and make use of Lemma 4.13.



**Example 4.14** (Discretisation of (4.10) Revisited). Having discretised the term  $\nabla \cdot (\alpha_u \nabla u)$  by (4.18) and (4.19), the latter discretisation turned out to be non-symmetric in stencil notation. Lemma 4.13 shows that this stencil yields a system of equations whose matrix is non-symmetric. Summarizing, an application of the chain rule for the divergence term is not preferable.

In addition to the symmetry property of the matrix  $\mathbf{A}^{(l+1)}$ , the matrix is positive definite for the variable diffusive case which can be directly deduced from Theorem 2.21. For the variable elastic case, the positive definiteness depends on the choice of  $\alpha$ ,  $\lambda$ ,  $\mu$ ,  $h$ , and  $k$ . However, for given  $h$ ,  $\alpha$ ,  $\lambda$ ,  $\mu$ , an upper bound similar to (3.41) can be achieved. For

$$k < \frac{h_1 h_2}{\|\alpha\|_\infty (\|\lambda\|_\infty + \|\mu\|_\infty)} \quad (4.36)$$

the positive definiteness of  $\mathbf{A}^{(l+1)}$  is ensured for the variable elastic case, too.

## 4.5 Numerical Solution

With the discretisation from the previous section we are faced with the numerical solution of the assembled system (4.31). For given digital images  $R_h, T_h$  and discretisations of a regularisation function  $\alpha_{u^{(0)}}$ , and – in the case of the elastic regulariser – Lamé parameter functions  $\lambda_{u^{(0)}}$  and  $\mu_{u^{(0)}}$ , the system can be treated by the following algorithm.

### Algorithm 4.15.

```

choose  $\mathbf{U}^{(0)}$  and  $k$ 
for  $l = 0, 1, \dots$  do
    compute force terms  $\mathbf{F}$  and  $\mathbf{G}$ 
    assemble  $\mathbf{A}$ 
    solve  $\mathbf{A}\mathbf{U}^{(l+1)} = \mathbf{U}^{(l)} + k\mathbf{F} + k\mathbf{G}$ 
    compute transformed template image  $T_{\mathbf{U}^{(l+1)}}$ 
    compute  $\alpha_{\mathbf{U}^{(l+1)}}$ ,  $\lambda_{\mathbf{U}^{(l+1)}}$ ,  $\mu_{\mathbf{U}^{(l+1)}}$ 
end
```

In addition to the remarks from Section 3.5 we present some notes and observations concerning implementation issues.

- When deriving the joint Euler-Lagrange equation (4.8) we suggested an allocation of the terms originating from the regulariser: Those terms with a linear dependency on  $u$  were collected in the operator  $L$ , those with a non-linear dependency in the function  $g$ . Then, the assembly (4.31) resulted in a linear system of equations.

Note that  $L$  is discretised at time level  $l+1$  whereas the time level of the discretisation of  $g$  is changed to  $l$ . However, this additional discretisation error is of the same order as the one for  $f$  and, following Lemma 4.11, is bounded by  $\mathcal{O}(k)$ .

- Recalling the size of the images to be  $N_1 \times N_2$  voxels, the assembled system consists of  $2N_1N_2$  equations. However, only a small percentage of the  $4N_1^2N_2^2$  matrix entries is non-zero. In order to estimate this percentage we observe from the stencils given in Corollary 4.12 the number of non-zero diagonals to be 5 for the variable diffusive regulariser and 13 for the variable elastic regulariser. Since the matrix is symmetric, only 3 (7) of them need to be stored which results in an upper bound for the number of non-zero matrix entries of  $6N_1N_2$  for the variable diffusive regulariser and  $14N_1N_2$  for the variable elastic regulariser. For a typical two-dimensional image of size  $256 \times 256$  this corresponds to a percentage of 0.002% (0.005%) non-zero entries in the system matrix. However, the storage amount is equivalent to 6 (14) additional images of the same resolution. Consequently, an explicit representation of the system matrix can only be recommended for images of moderate size.
- When using variable parameters, these are typically designed such that their gradient takes locally high values. This may cause a displacement field with a large gradient at the same positions, cf. the motivating example in Figure 4.4. Since the function  $g$  is built up from products of differentiated parameter functions and the differentiated displacement field, a large gradient in each factor results in a large value of  $g$ . As a consequence, stability problems are likely to be observed and a largely decreased temporal step size is required.

A stabilized solution is provided by the *minmod slope* technique as described by LEVEQUE (1992). For some function  $s : \mathbb{R} \rightarrow \mathbb{R}$  and equidistantly distributed nodes  $(x^i)_i$ , the derivative of  $s$  at  $x^i$  is approximated by

$$\frac{1}{x^{i+1}-x^i} \minmod(s(x^{i+1}) - s(x^i), s(x^i) - s(x^{i-1}))$$

where

$$\minmod(a, b) := \frac{1}{2}(\operatorname{sgn}(a) + \operatorname{sgn}(b)) \min(|a|, |b|) .$$

Here, the naming results from the construction of the minmod term: From the left-hand and the right-hand derivative at  $x^i$ , the one with smaller modulus is chosen. By employing the minmod technique for derivatives in  $g$ , a stabilised scheme can be observed.

- If the given images are of moderate size, a direct solution scheme for the assembled system can be employed. For a positive definite system matrix as occurring here (in case of the variable elastic regulariser, provided  $k$  is chosen appropriately, cf. (4.36) for an upper bound), a Cholesky factorisation is used. If the matrix is indefinite, a Gaussian elimination with partial pivoting is employed as supplied by the Matlab \-operator. For a practical treatment of larger images, multigrid techniques are advisable but not discussed in this thesis.
- The multi-resolution scheme from Section 3.5 is extended by pyramids for the parameter functions  $\alpha$ ,  $\lambda$ , and  $\mu$ .

## 4.6 Choice of Parameters

The choice of parameters for the variable regularisers differs from that for the standard regularisers from Chapter 3. In the presence of variable regularisers, the regularisation parameter  $\alpha$  takes the ‘gap role’ by allowing gaps to change their size, i.e., by decreasing  $\alpha$  locally, a gap between different image structures is allowed to either enlarge or shrink. In contrast, the Lamé parameters take the ‘elastic role’ and focus on modelling different elastic properties which include the approximated preservation of volume or shape.

Note that for any choice of parameters in the following, the parameters are assumed to be differentiable, i.e., when prescribing different values in adjacent regions  $\Omega^i, \Omega^j$ , a smooth transition is assumed.

### 4.6.1 Regularisation Parameter

By a variable regularisation, image regions can be regularised individually. For illustration we revisit Example 3.20 and modify it in two ways. In both examples the variable diffusive regulariser is used and we are faced with the regularisation parameter  $\alpha$  only. Therefore,  $\alpha$  takes both the gap role and the elastic role.

**Example 4.16.** In this example we take template and reference image as in Example 3.20 but modify the reference image (cf. the dashed line in each plot from the bottom row in Figure 4.8) by adding white noise with a standard deviation of 10% of the previous grey-value scale in the interval where the zig-zag type function is constant. The removal of noise (or of metal artefacts as discussed in Example 3.22) is still an active field of research in image reconstruction. In this context we are interested in how well the registration scheme copes with the presence of noise in a certain image region.

As before, at position  $x = 0$  a boundary condition of Dirichlet type is presumed, at position  $x = 1$  one of Neumann type. For the registration three different settings are employed.

The first setting is the same as the first one in Example 3.20 (cf. the first column in Figure 3.1), i.e.  $\alpha \equiv 5 \cdot 10^{-5}$ . For the remaining settings we do not change  $\alpha$  in the entire interval  $[0, 1]$  but within the centre interval where the zig-zag type function is constant. Here,  $\alpha$  is increased by a factor of 10 for the second setting and by a factor 100 for the last setting.

An investigation of the resulting displacement function (depicted solid in each of the top row images in Figure 4.8) reveals an influence of the added noise which is the smaller the larger  $\alpha$  is locally chosen. In particular, the displacement function from the third setting differs hardly from the result obtained without any added noise. This is also visible from the transformed identity image shown in the bottom row of Figure 4.8 (solid lines): The larger  $\alpha$  is locally chosen, the less the transformed template is influenced by the noise in the reference image.

**Example 4.17.** Let the template and the reference image be given as in Example 3.20. Boundary conditions are again of mixed type. For the regularisation, three different settings are considered.

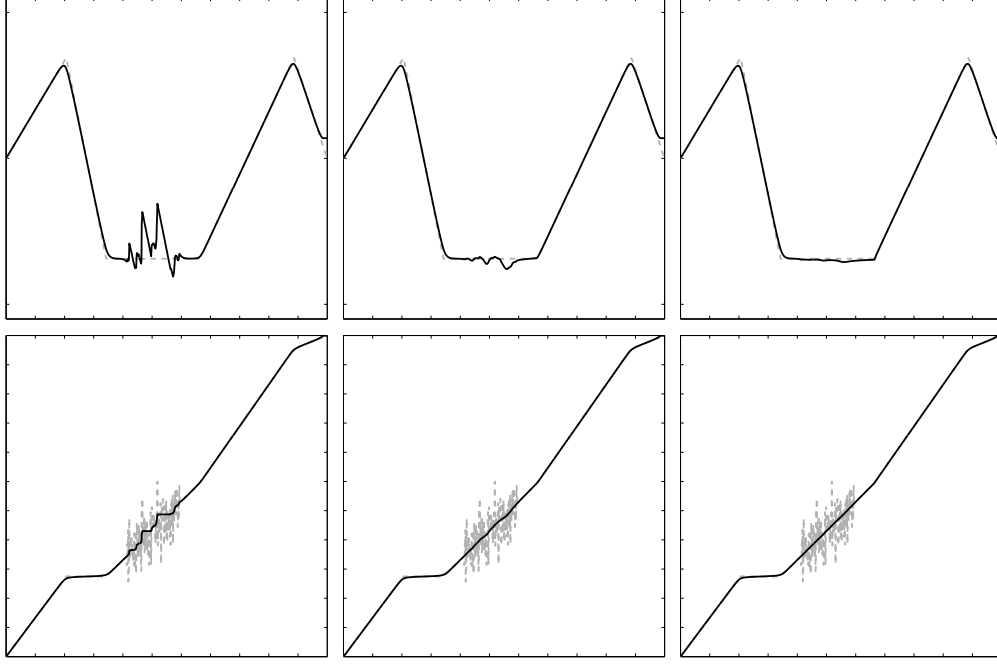


Figure 4.8: An application of a zig-zag type function (dashed line in each of the top row images) to the identity image results in a transformed image (depicted dashed in each of the bottom row images) to which in the centre interval white noise has been added. The regularisation is chosen as  $\alpha(x) = 5 \cdot 10^{-5}$  in all the three columns except from the centre interval where  $\alpha$  is multiplied by 10 (centre column) and 100 (right column). The registration result is depicted solid with respect to the displacement function (top row) and the transformed identity image (bottom row).

The first setting with  $\alpha \equiv 5 \cdot 10^{-5}$  is the same as the first one in Example 3.20, cf. the first column in Figure 3.1, and serves as reference setting. For the remaining settings, we increase  $\alpha$  in the entire interval  $[0, 1]$  to  $5 \cdot 10^{-4}$  and  $5 \cdot 10^{-3}$  in the second and the third setting, respectively, except from a certain position within that interval where the reference image is close to constant. At this position the regularisation remains the value of  $\alpha(x) = 5 \cdot 10^{-5}$  in all the three settings. Therefore,  $\alpha$  takes – similarly to the step case depicted in Figure 4.4 – the form of a Dirac-shaped weighting function (Figure 4.9, top left) and allows for the enlargement of a gap.

For the result of the registration our observation is twofold. Globally, the displacement function (cf. Figure 4.9, top centre and right) and the transformed template image (bottom centre and right) show the same behaviour as in Figure 4.4: the larger  $\alpha$  is, the smoother are both  $u$  and  $T_u$ . Locally, however, the result is less regularised and fits nicely with the zig-zag type function. Moreover, due to the dependence of  $\alpha$  on  $u$ , the formerly peak-shaped region of reduced regularisation is automatically extended to the entire region where the reference image is close to constant ( $\alpha_u$  is shown in Figure 4.9, bottom left). Such a result demonstrates the capability of a locally reduced regularisation while preserving the overall smoothness.

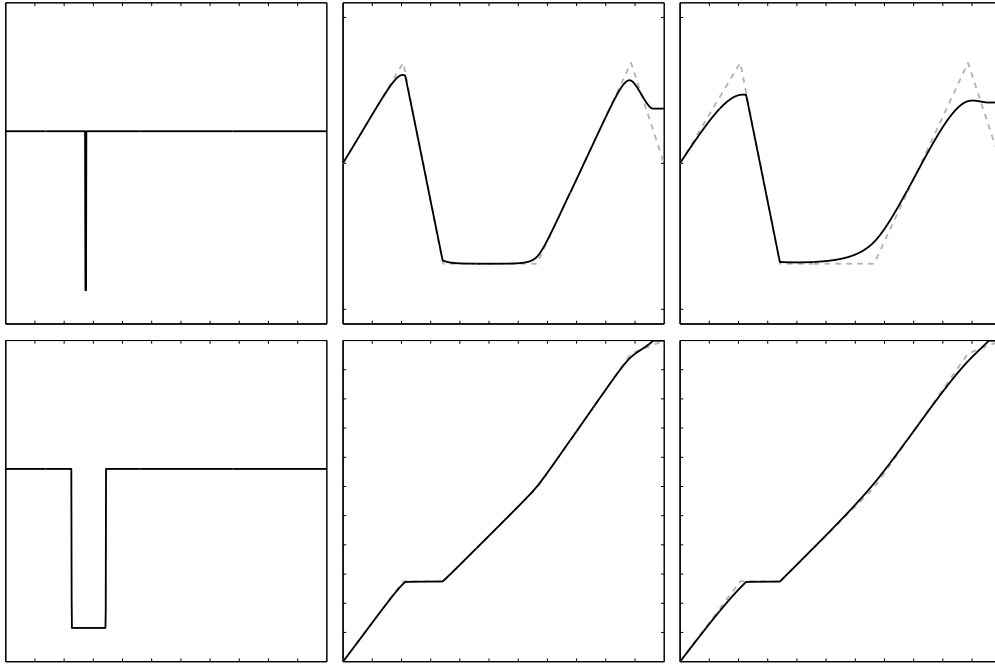


Figure 4.9: An application of a zig-zag type function (dashed line in top centre and top right) to the identity image results in a transformed image (depicted dashed in bottom centre and bottom right). Various regularisation functions (shown schematically in the left column before and after registration, see text for further details) result in globally smooth but locally less smooth displacement functions (solid line in top centre and right). Below, their application to the identity image is depicted in solid lines.

Summarizing, the regularisation parameter can be used to regularise various image regions individually as well as to let a gap enlarge or shrink. While in the first case  $\alpha$  was increased in a region to reduce the influence of noise, in the latter case  $\alpha$  was decreased at a position where a gap was likely to enlarge.

By the variable diffusive regulariser both the elastic and the gap role are supported. In the following section we will investigate the variable elastic regulariser. Here, the elastic role is taken by the Lamé parameters.

#### 4.6.2 Lamé Parameters

By a variable elastic regulariser, individual elastic properties can be assigned to various regions of the same image. To illustrate this property we modify Example 3.23.

**Example 4.18.** Let the setting be as in Example 3.23 except for  $\lambda$  which is chosen spatially variant. Within the square located in the centre of the template image (not shown),  $\lambda = 1000$  is chosen, whereas in the remaining part of the image,  $\lambda = 0$  is set. This setting corresponds to the deformation of a composite consisting of an (almost) incompressible object which is embedded in a highly compressible one. By the artificial forces acting on the left- and the right-hand side of the square it can be observed, on the one hand, how the incompressible

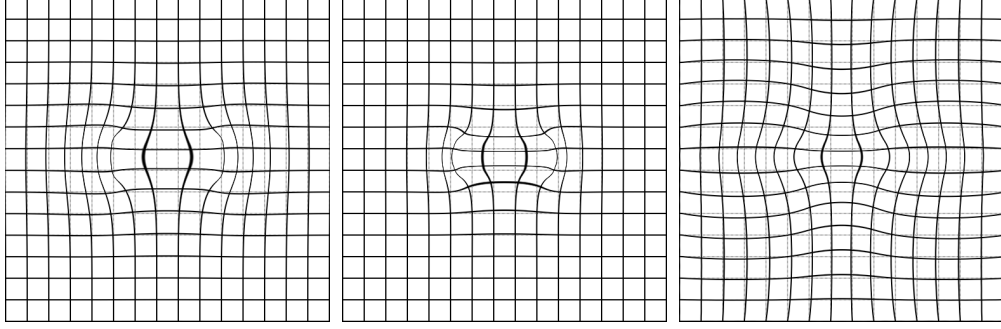


Figure 4.10: Visualized displacement field resulting from the stretching of a composite object (centre), see text for further details. For comparison, the stretching of a single object is displayed on the left (with  $\lambda \equiv 0$ ) and on the right (with  $\lambda \equiv 1000$ ).

square is stretched and, on the other hand, how the deformation induced by the stretch is damped within the compressible object.

For comparison we added results from Example 3.23 with  $\lambda$  being constant in the entire domain (see Figure 4.10 for  $\lambda \equiv 0$  (left) and  $\lambda \equiv 1000$  (right), these are the same as in Figure 3.4, second and third column).

From the displacement field in the composite case (cf. Figure 4.10, centre) we observe within the inner object a stretching similar to the one in the incompressible case (note in particular the shrinkage in the component transversal to the acting forces). In the outer object the deformation is damped as in the compressible case (note the stretch in the longitudinal component as well as the nearly vanished shrinkage in the transversal component).

In summary, the variable regularisers allow for modelling locally varying elastic properties as well as for the enlargement or shrinkage of dedicated image regions. However, the displacement function  $u$  and the involved parameter functions  $\alpha$ ,  $\lambda$ , and  $\mu$  are required to be differentiable. The drawback of this scheme lies in the restriction that any gap likely to enlarge has to be already ‘visible’ in the template image, i.e., a gap of voxel width has to exist. In the context of the composite this means that the modelling of a composite object whose parts are not fixed to each other (metaphorically speaking, like forgetting the glue) is not supported. This case will be discussed in the following chapter.

---

## 5 Piecewise Variable Regularisation

---

Chapter 3 started by describing an image registration scheme where any parameter function was constant and the displacement field a smooth function. Then, in Chapter 4, the parameter functions were allowed to depend on the spatial position but, like the displacement function, they were still required to be smooth. However, a lowered degree of smoothness – or even a discontinuous displacement field – may show up in various image registration problems.

As an example towards a lowered differentiability we consider a composite of different materials. In the mathematical formulation, this leads to a parameter function being constant within each material object and showing a step discontinuity at the interface. We show for a one-dimensional example how the variational calculus deals with this kind of problems before we extend the setting to other types of discontinuities.

**Example 5.1** (Composite). We choose the SSD measure and the variable diffusive regulariser from Definition 3.11 and Definition 4.2, respectively, and modify them in two aspects. Firstly, the domain  $\Omega$  is divided into two subdomains,

$$\Omega = \Omega^1 \cup \Omega^2, \quad \Omega^1 = (a, \gamma), \quad \Omega^2 = (\gamma, b),$$

with a common boundary  $\Gamma^{1,2} = \{\gamma\}$ . Secondly, the regularisation parameter  $\alpha$  is given the role of the discontinuous parameter function and set as  $\alpha(x) = \alpha^z > 0$  in  $\Omega^z$  for  $z = 1, 2$ . Then the minimisation problem reads

$$\frac{1}{2} \sum_{z=1}^2 \int_{\Omega^z} [R(x) - T_u(x)]^2 dx + \int_{\Omega^z} \alpha^z [u'(x)]^2 dx \xrightarrow{u} \min. \quad (5.1)$$

Note that  $u$  does not belong to a solution space consisting of functions being differentiable in the entire domain as in (3.2). Instead, the differentiability requirement for this problem is lowered in such a way that at  $\gamma$  any function  $u$  needs to be continuous only. With a space of test functions  $\mathcal{V}$  of the same

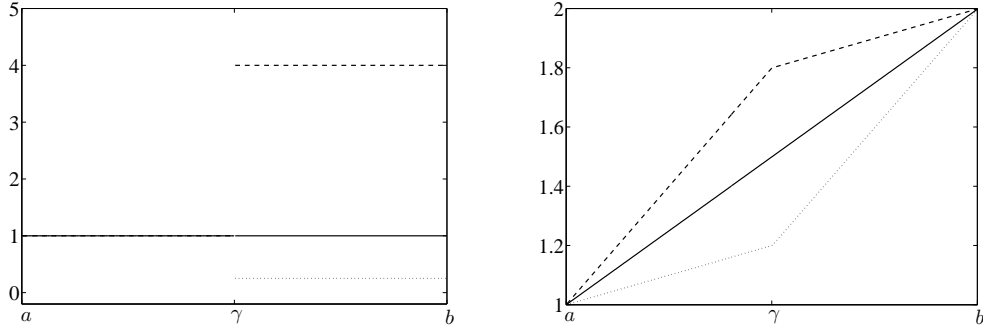


Figure 5.1:  $\alpha$  (left) and  $u$  (right) are depicted for a numerical solution of (5.2) with  $\alpha^1=1$  and  $\alpha^2 \in \{0.25, 1, 4\}$  for the dotted, solid, and dashed line, respectively.

lowered differentiability, the Gâteaux derivative of (5.1) is given by

$$\begin{aligned} & - \sum_{z=1}^2 \int_{\Omega^z} [R(x) - T_u(x)] T'_u(x) v(x) dx + \int_{\Omega^z} \alpha^z u''(x) v(x) dx \\ & + \{ \alpha^1 (u'v)(\gamma-) - \alpha^2 (u'v)(\gamma+) \} + \{ \alpha^1 (u'v)(b) - \alpha^2 (u'v)(a) \} = 0 \end{aligned}$$

to hold for all  $v \in \mathcal{V}$ . Note that at the position  $\gamma$ ,  $v$  is still continuous, thus  $v(\gamma) = v(\gamma-) = v(\gamma+)$ . By employing Dirichlet boundary conditions on  $a$  and  $b$ , the second curly bracketed term vanishes. In addition, to apply the Fundamental Lemma of Variation 3.7, the first curly bracket has to vanish as well. We call the resulting additional condition

$$\{ \alpha^1 u'(\gamma-) - \alpha^2 u'(\gamma+) \} v(\gamma) = 0$$

a *natural interface condition* which is motivated by the analogy to natural boundary conditions. By Theorem 3.7 and due to  $\alpha^z$  being positive, we finally arrive at the boundary value problem

$$\begin{aligned} \alpha^z u''(x) &= -[R(x) - T_u(x)] T'_u(x), & x \in \Omega^z, \quad z = 1, 2, \\ \alpha^1 u'(\gamma-) &= \alpha^2 u'(\gamma+), \\ u(x) &= 0, & x \in \partial\Omega. \end{aligned} \tag{5.2}$$

The major difference to the variational approach described in Chapter 3 (cf., for instance, Example 3.8) is given by the additional interface condition at  $\gamma$ . Note that, if  $\alpha^1 = \alpha^2$ , the natural interface condition simplifies to  $u'$  being continuous at  $\gamma$ .

For a numerical solution to (5.2) we choose  $u(a) = 1$  and  $u(b) = 2$ . Moreover, we choose  $T, R$  such that  $[R(x) - T_u(x)] T'_u(x) \equiv 0$  since we are interested in the effect of a discontinuous regularisation parameter rather than in the effect of the image content. For fixed  $\alpha^1$  and various choices for  $\alpha^2$  as depicted in Figure 5.1, left, a continuous solution  $u$  with a discontinuity in its first derivative at  $\gamma$  is visible (shown in Figure 5.1, right). Approximately the same result can be achieved when solving (5.2) analytically with  $\alpha$  chosen as a function of arctan type.



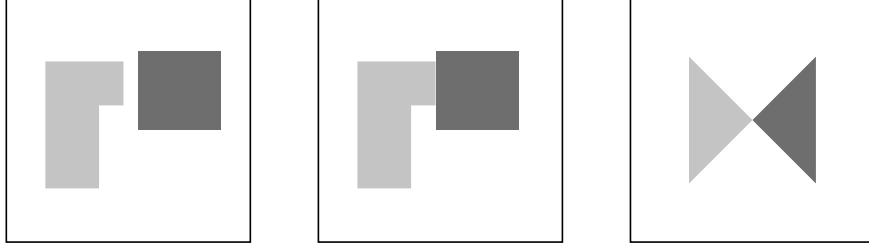


Figure 5.2: Each decomposition consists of three regions – two object regions,  $\Omega^1$  and  $\Omega^2$ , and a background region  $\Omega^0$ . The left and the centre decomposition are topologically different but not the left and the right one.

**Remark.** The boundary value problem 5.2 as the necessary condition to (5.1) requires  $u$  to be twice continuously differentiable within  $\Omega^1$  and  $\Omega^2$ . However, by OBERLE (1998) it has been shown that a necessary condition for a solution of (5.1) can be achieved without the use of partial integration and, furthermore, that a continuous first derivative of  $u$  in  $\Omega^1$  and  $\Omega^2$  is sufficient. Then, if  $\alpha$  is constant, i.e.  $\alpha^1 = \alpha^2$ , the lowered differentiability at  $\gamma$  is regained and we conclude that the minimisation problem

$$\frac{1}{2} \int_{\Omega} [R(x) - T_u(x)]^2 dx + \frac{1}{2} \int_{\Omega} \alpha [u'(x)]^2 dx \xrightarrow{u} \min$$

with  $\alpha$  being constant serves as a special case of (5.1).

Alternatively, the composite object may consist of various materials which are *not* fixed to each other. To distinguish this setting of a ‘moving composite’ from the former setting of a (fixed) composite, we define a *topological change*.

**Definition 5.2** (Topological Change). *Given a domain  $\Omega$  with decompositions*

$$M_a(\Omega) := \{\Omega_a^0, \Omega_a^1, \Omega_a^2\} \quad \text{and} \quad M_b(\Omega) := \{\Omega_b^0, \Omega_b^1, \Omega_b^2\}$$

*such that the common boundary of  $\Omega_a^1$  and  $\Omega_a^2$  is a zero set whereas the one of  $\Omega_b^1$  and  $\Omega_b^2$  is non-zero with measure larger than zero, then  $M_a$  and  $M_b$  are said to be topologically different, or, in other words, when switching from  $M_a$  to  $M_b$ , a topological change occurs.*

In Figure 5.2, left and centre, an example for a topological change is depicted. Note that the decomposition depicted on the right is *not* topologically different from the left one since the common boundary  $\Gamma^{1,2}$  is a set of measure zero.

Furthermore, it can be observed that an image according to Definition 2.2 and with a decomposition as depicted in Figure 5.2, left, may be non-smooth after being transformed according to Figure 5.2, centre. In contrast, given an image with a decomposition as in Figure 5.2, centre, is smooth by definition and, moreover, preserves its smoothness during transition to an image with a decomposition according to Figure 5.2, left. Summarising, in case of a closing gap, the transformed image is not necessarily smooth which motivates a less restricted definition of an image.

**Definition 5.3** (Piecewise Smooth Image). *Given a domain  $\Omega$  with a decomposition  $M(\Omega) = \{\Omega^0, \Omega^1, \dots, \Omega^m\}$ , a piecewise smooth image  $I$  is defined as a mapping  $I : \bar{\Omega} \rightarrow [0, 1]$  such that, for each  $z = 0, \dots, m$ ,  $I$  is smooth on  $\Omega^z$ . In addition, let  $\text{Img}_{\mathcal{PS}}(M(\Omega))$  define the set of piecewise smooth images on a decomposition  $M(\Omega)$ .*

Clearly, a setting with a topological change is more challenging than before, since now a discontinuity in the displacement field may occur. Determining the Euler-Lagrange equation for this setting is not obvious and call for a repeated investigation of variational calculus which is subject of the following section. Afterwards, Section 5.2 describes how to introduce discontinuities in the registration scheme whereas the final sections are devoted to its discretisation and numerical solution.

## 5.1 Calculus of Variations Revisited

Throughout this section let  $M(\Omega) = \{\Omega^0, \Omega^1, \dots, \Omega^m\}$  be a decomposition of  $\Omega$ . Then, with a functional  $F : \bar{\Omega} \times \mathbb{R}^d \times \mathbb{R}^{d \times d} \rightarrow \mathbb{R}$  a slight modification of the general minimisation problem from (3.1) and (3.5) yields

$$\mathcal{J} : \mathcal{U} \rightarrow \mathbb{R}, \quad \mathcal{J}[u] := \sum_{z=0}^m \int_{\Omega^z} F[x, u(x), \nabla u(x)] dx \xrightarrow{u} \min \quad \text{on } \bar{\Omega}. \quad (5.3)$$

Note that the solution space  $\mathcal{U}$  for this problem is not properly defined yet. With Example 5.1 in mind, our aim is to construct an enlarged solution space such that it includes functions which are at certain positions not necessarily differentiable or not even continuous.

**Definition 5.4** ( $\mathcal{PC}^p, \mathcal{PC}^{\text{const}}$ ). *Given a domain  $\Omega$  with decomposition  $M(\Omega)$ , the space of  $p$ -times piecewise continuously differentiable functions is defined as*

$$\mathcal{PC}^p(M(\Omega), \mathbb{R}^d) := \{u \mid u|_{\Omega^z} \in \mathcal{C}^p(\Omega^z \cup (\partial\Omega^z \cap \partial\Omega), \mathbb{R}^d), z = 0, 1, \dots, m\}.$$

Moreover, the space of piecewise constant functions is given by

$$\mathcal{PC}^{\text{const}}(M(\Omega), \mathbb{R}^d) := \{u \mid u : \bar{\Omega} \rightarrow \mathbb{R}^d, u|_{\Omega^z} \equiv \text{const}, z = 0, 1, \dots, m\}.$$

Note that the differentiability is required in regions whose boundary may be included in parts. In such a case, a derivative is understood in a one-sided sense. Furthermore we note that for  $m = 0$  the space  $\mathcal{PC}^p(M(\Omega), \mathbb{R}^d)$  is equivalent to the space  $\mathcal{C}^p(\bar{\Omega}, \mathbb{R}^d)$ .

Based on the definition above, solution and test space can be enlarged. They consist of functions which are twice continuously differentiable within each region  $\Omega^z$  but not necessarily continuous at the common boundaries,

$$\begin{aligned} \mathcal{U}_{\mathcal{PC}} &:= \{u \mid u \in \mathcal{PC}^2(M(\Omega), \mathbb{R}^d), u \text{ fulfills boundary conditions on } \partial\Omega\}, \\ \mathcal{V}_{\mathcal{PC}} &:= \{v \mid v = u - \hat{u}, u, \hat{u} \in \mathcal{U}_{\mathcal{PC}}\}. \end{aligned}$$

It is important to note that  $\mathcal{U}_{\mathcal{PC}}$  and  $\mathcal{V}_{\mathcal{PC}}$  are based on the same decomposition  $M$ . Thus, the possible positions of a discontinuity in functions from  $\mathcal{U}_{\mathcal{PC}}$  and

$\mathcal{V}_{\mathcal{PC}}$  coincide and the former definitions of a neighbourhood, a local minimiser, a Gâteaux derivative, and a stationary point (cf. Definitions 3.1–3.4) are valid in the context of  $\mathcal{U}_{\mathcal{PC}}$  and  $\mathcal{V}_{\mathcal{PC}}$  as well. Also, the necessary condition for a local minimiser remains the same as stated in Theorem 3.5. Finally we note that by a Gâteaux-differentiable functional we still assume the functional to be Gâteaux-differentiable in all directions of the respective test space.

Having constructed an appropriate solution space for the minimisation problem (5.3) we investigate the condition for a stationary point of  $\mathcal{J}$  which is, following Theorem 3.5, the necessary condition for a solution of (5.3). Before, an extension of the Fundamental Lemma of Variation is presented.

**Lemma 5.5** (Extended Lemma of Variation). *Let  $\theta : \Omega \rightarrow \mathbb{R}^d$  be continuous in each  $\Omega^z$ . Then  $\sum_{z=0}^m \int_{\Omega^z} (\theta, v) dx = 0$  holds for all test functions  $v \in \mathcal{V}_{\mathcal{PC}}$  if and only if  $\theta$  is identically zero on  $\Omega^z$  for all  $z = 0, \dots, m$ .*

*Proof.* First, we assume  $\sum_{z=0}^m \int_{\Omega^z} (\theta, v) dx = 0$  to hold for all test functions and establish by contradiction that  $\theta \equiv 0$ .

Let  $n \in \{1, \dots, d\}$ ,  $z \in \{0, \dots, m\}$ . Suppose that  $\theta_n(\zeta) \neq 0$  for some  $\zeta \in \Omega^z$ . Then, since  $\theta_n$  is continuous at  $\zeta$ , there exists a neighbourhood  $\mathcal{B}_\varepsilon(\zeta) \subset \Omega^z$  with  $\varepsilon > 0$ , such that  $\theta_n(x) > 0$  or  $\theta_n(x) < 0$  everywhere in  $\mathcal{B}_\varepsilon(\zeta)$ . Choosing a  $v \in \mathcal{V}$  such that  $v_n(x)$  is positive within  $\mathcal{B}_\varepsilon(\zeta)$  and zero within  $\Omega \setminus \mathcal{B}_\varepsilon(\zeta)$  and such that  $v_\eta(x)$  is identically zero for  $\eta \neq n$ , we can conclude  $\sum_{z=0}^m \int_{\Omega^z} (\theta, v) dx \neq 0$  for the chosen  $v$ . This is a contradiction to the assumption.

It turns, from setting  $\theta \equiv 0$ , it follows immediately that  $\sum_{z=0}^m \int_{\Omega^z} (\theta, v) dx = 0$  for all test functions. ■

To distinguish the normal vector with respect to the boundary of the domain from the one with respect to the boundary of a region, we make use of the notation  $\mathbf{n}^z$  as the unit normal vector pointing outward with respect to the region  $\Omega^z$ .

**Lemma 5.6** (Necessary Condition). *Every solution  $u \in \mathcal{PC}^2(M(\Omega), \mathbb{R}^d)$  of the general minimisation problem (5.3) with a Gâteaux-differentiable functional  $\mathcal{J}$  is a solution of the boundary value problem consisting of the system of Euler-Lagrange equations*

$$\nabla_u F - \nabla \cdot \nabla_{\nabla u} F = 0 \quad \text{on } \Omega^z, \quad z = 0, \dots, m, \quad (5.4)$$

*natural interface conditions*

$$(\nabla_{\nabla u} F, \mathbf{n}^z) = 0 \quad \text{on } \partial\Omega^z \setminus \partial\Omega, \quad z = 0, \dots, m, \quad (5.5)$$

*and boundary conditions which can be either of essential type (when given by the solution space  $\mathcal{U}_{\mathcal{PC}}$ ) or of natural type,*

$$(\nabla_{\nabla u} F, \mathbf{n}) = 0 \quad \text{on } \partial\Omega. \quad (5.6)$$

*Proof.* Let solution spaces

$$\begin{aligned}\mathcal{U}_{\mathcal{PC}} &:= \{u \mid u \in \mathcal{PC}^2(M(\Omega), \mathbb{R}^d)\}, \quad \check{\mathcal{U}}_{\mathcal{PC}} := \{u \mid u \in \mathcal{U}_{\mathcal{PC}}, u = c \text{ on } \partial\Omega\}, \\ \tilde{\mathcal{U}}_{\mathcal{PC}} &:= \{u \mid u \in \check{\mathcal{U}}_{\mathcal{PC}}, u = c \text{ on } \partial\Omega^z, z = 0, \dots, m\}\end{aligned}$$

and corresponding test spaces

$$\begin{aligned}\mathcal{V}_{\mathcal{PC}} &:= \{v \mid v \in \mathcal{PC}^2(M(\Omega), \mathbb{R}^d)\}, \quad \check{\mathcal{V}}_{\mathcal{PC}} := \{v \mid v \in \mathcal{V}_{\mathcal{PC}}, v = 0 \text{ on } \partial\Omega\}, \\ \tilde{\mathcal{V}}_{\mathcal{PC}} &:= \{v \mid v \in \check{\mathcal{V}}_{\mathcal{PC}}, v = 0 \text{ on } \partial\Omega^z, z = 0, \dots, m\}\end{aligned}$$

be given. Let  $u \in \mathcal{U}_{\mathcal{PC}}, v \in \mathcal{V}_{\mathcal{PC}}, \tau \in \mathbb{R}$ . Then, by setting the Gâteaux derivative of  $\mathcal{J}$  for  $u$  in the direction of  $v$  to zero, in analogy to Lemma 3.6 we arrive at

$$\begin{aligned}0 = \delta\mathcal{J}[u; v] &= \left. \frac{d\mathcal{J}[u + \tau v]}{d\tau} \right|_{\tau=0} \\ &= \sum_{z=0}^m \int_{\Omega^z} \left. \frac{dF[x, u(x) + \tau v(x), \nabla u(x) + \tau \nabla v(x)]}{d\tau} \right|_{\tau=0} dx \\ &= \sum_{z=0}^m \int_{\Omega^z} \sum_{n=1}^d \frac{\partial F}{\partial u_n} v_n + \sum_{n,\eta=1}^d \frac{\partial F}{\partial u_{n,x_\eta}} v_{n,x_\eta} dx \\ &= \sum_{z=0}^m \int_{\Omega^z} (\nabla_u F - \nabla \cdot \nabla_{\nabla u} F, v) dx \\ &\quad + \sum_{z=0}^m \int_{\partial\Omega^z} \sum_{n=1}^d (\nabla_{\nabla u_n} F, \mathbf{n}^z) v_n dx, \tag{5.7}\end{aligned}$$

holding for all test functions  $v \in \mathcal{V}_{\mathcal{PC}}$ , as the condition for a stationary point of  $\mathcal{J}$ . In particular, (5.7) holds for a subspace of  $\mathcal{V}_{\mathcal{PC}}$ , e.g. for all  $v \in \tilde{\mathcal{V}}_{\mathcal{PC}}$ . Since, for  $\tilde{\mathcal{V}}_{\mathcal{PC}}$ , the boundary integral in (5.7) is zero due to the prescribed boundary and interface conditions, Lemma 5.5 can be applied which implies the Euler-Lagrange equations (5.4). Inserting them into (5.7) yields

$$\sum_{z=0}^m \int_{\partial\Omega^z} \underbrace{\sum_{n=1}^d (\nabla_{\nabla u_n} F, \mathbf{n}^z) v_n}_{=:\Psi} dx = 0$$

to hold for all test functions from  $\mathcal{V}_{\mathcal{PC}}$ . With the abbreviation  $\Psi$  for the integrand, the equation can be rewritten as

$$0 = \sum_{z=0}^m \int_{\partial\Omega^z} \Psi dx = \int_{\partial\Omega} \Psi dx + \sum_{z=0}^m \int_{\partial\Omega^z \setminus \partial\Omega} \Psi dx. \tag{5.8}$$

Here, on the right-hand side the first term acts on the boundary of  $\Omega$  and is the same as in Section 3.1. It vanishes in the case of essential boundary conditions on  $\partial\Omega$  (i.e.,  $u \in \check{\mathcal{U}}_{\mathcal{PC}}$ ). The second term represents the natural interface condition and acts on the boundary of each single region  $\Omega^z$ .

However, in both the case of essential and of natural boundary conditions on  $\partial\Omega$ , (5.8) holds for all  $\mathcal{V}$ . Since  $v \in \mathcal{V}$  can be arbitrarily chosen, (5.5) and – in the case of natural conditions on  $\partial\Omega$  – additionally (5.6) must be satisfied.  $\blacksquare$

Compared to the necessary condition derived in Chapter 3, now on each region  $\Omega^z$  a system of Euler-Lagrange equations is given which consists of the same difference equation and is supplemented by additional interface conditions on each inner boundary  $\partial\Omega^z$ .

We revisit Example 5.1, but now with a displacement function  $u$  being not necessarily continuous at  $\gamma$ .

**Example 5.7** (Moving Composite). Let the minimisation problem (5.1) be given together with the specifications from Example 5.1 except for  $u \in \mathcal{U}_{\mathcal{PC}}$  and  $v \in \mathcal{V}_{\mathcal{PC}}$ . By Lemma 5.6, the boundary value problem

$$\begin{aligned} \alpha^z u''(x) &= -[R(x) - T_u(x)]T'_u(x), & x \in \Omega^z, \ z = 1, 2, \\ \alpha^1 u'(\gamma-) &= 0, \\ \alpha^2 u'(\gamma+) &= 0, \\ u(x) &= 0, & x \in \partial\Omega \end{aligned}$$

results. As in Example 5.1, the additional assumption  $\alpha^1 = \alpha^2$  simplifies the natural interface condition to  $u'$  being continuous (actually, even to  $u'(\gamma) = 0$ ). However, we cannot conclude the continuity of  $u$  which can be seen from the fact that for a general functional  $F$  on the common boundary  $\Gamma^{z_1, z_2}$  of two regions  $\Omega^{z_1}, \Omega^{z_2}$ , the equations

$$(\nabla_{\nabla u} F, \mathbf{n}^{z_1})|_{\partial\Omega^{z_1}} = 0 \quad \text{and} \quad (\nabla_{\nabla u} F, \mathbf{n}^{z_2})|_{\partial\Omega^{z_2}} = 0$$

are not sufficient for  $u|_{\partial\Omega^{z_1}} = u|_{\partial\Omega^{z_2}}$  to hold on  $\Gamma^{z_1, z_2}$ . As a consequence and in contrast to Example 5.1, the minimisation problem (5.1) cannot be obtained as a special case of the moving composite.

## 5.2 Discontinuities in Image Registration

Coming back to image registration, the functionals  $\mathcal{J}$  and  $F$  in (5.3) are chosen according to the sum of distance measure and regularising term. Based on a decomposition  $M(\Omega_R)$ , i.e. with respect to the domain of the reference image, into regions  $\Omega^z$ , Definition 3.11 can be extended as follows.

**Definition 5.8** (Piecewise SSD Measure). *Given a decomposition  $M(\Omega_R)$ , images  $T \in \text{Img}(\Omega_T)$ ,  $R \in \text{Img}_{\mathcal{PS}}(M(\Omega_R))$ , and a displacement field  $u \in \mathcal{U}_{\mathcal{PC}}$ , the piecewise SSD measure is defined as*

$$\mathcal{D}_{T,R}^{pSSD}[u] := \frac{1}{2} \sum_{z=0}^m \int_{\Omega^z} [R(x) - T_u(x)]^2 dx. \quad (5.9)$$

Determining the corresponding Euler-Lagrange equation is obvious, in particular since  $\nabla_{\nabla u}[R(x) - T_u(x)]^2 = 0$  and, thus, the natural interface condition (5.5) vanishes.

**Lemma 5.9** (Euler-Lagrange Equation for the Piecewise SSD Measure). *The system of Euler-Lagrange equations for the piecewise SSD measure is given by*

$$-[R(x) - T_u(x)]\nabla T_u(x) = 0, \quad x \in \Omega^z, \quad z = 0, \dots, m. \quad (5.10)$$

*Proof.* By straightforward application of Lemma 5.6. ■

The investigation of appropriate regularisers requires the consideration of the parameter functions  $\alpha$ ,  $\lambda$ , and  $\mu$ . With an application similar to Example 5.1 in mind, the functions are set constant within each region, e.g.,

$$\alpha(x) = \alpha^z, \quad x \in \Omega^z.$$

In contrast to the variable regularisers  $\mathcal{S}_\alpha^{vardiff}$  and  $\mathcal{S}_{\alpha,\lambda,\mu}^{varelas}$ , here, the parameter functions are evaluated with respect to a position  $x \in \Omega_R$ , thus according to a decomposition  $M(\Omega_R)$ . Otherwise, i.e., when evaluating with respect to a position  $x + u(x) \in \Omega_T$ , we may obtain a solution  $u^*$  to the Euler-Lagrange equation where  $u^*$  is not well defined. This happens if, for fixed  $z \in \{0, \dots, m\}$ ,  $u^*$  does not map a boundary  $\partial\Omega_R^z$  onto  $\partial\Omega_T^z$  and, thus, a discontinuity in a parameter function (located on  $\partial\Omega_T^z$ ) is mapped into  $\Omega_R^z$  instead on  $\partial\Omega_R^z$ . As a consequence from the initialisation of the parameter functions in  $\Omega_R$ , the additional term  $g$  occurring with the variable regularisers will be zero for the piecewise variable regularisers.

**Definition 5.10** (Piecewise Diffusive Regularisation). *Given a decomposition  $M(\Omega_R)$ , a weighting function  $\alpha \in \mathcal{PC}^{const}(M(\Omega_R), \mathbb{R}^+)$ , and a displacement field  $u \in \mathcal{UPC}$ , the piecewise diffusive regulariser is defined as*

$$\mathcal{S}_\alpha^{pdiff}[u] := \frac{1}{2} \sum_{z=0}^m \alpha^z \int_{\Omega^z} \sum_{n=1}^d \|\nabla u_n(x)\|_2^2 dx. \quad (5.11)$$

**Lemma 5.11** (Euler-Lagrange Equation for the Piecewise Diffusive Regulariser). *The system of Euler-Lagrange equations and natural interface conditions for the piecewise diffusive regulariser is given by*

$$\begin{aligned} -\alpha^z \Delta u(x) &= 0, & x \in \Omega^z, \quad z = 0, \dots, m, \\ \alpha^z (\nabla u(x), \mathbf{n}^z(x)) &= 0, & x \in \partial\Omega^z \setminus \partial\Omega, \quad z = 0, \dots, m. \end{aligned} \quad (5.12)$$

*Proof.* Follows from Lemma 3.14 and Lemma 5.6. ■

**Definition 5.12** (Piecewise Elastic Regularisation). *Given a decomposition  $M(\Omega_R)$ , a weighting function  $\alpha \in \mathcal{PC}^{const}(M(\Omega_R), \mathbb{R}^+)$  as well as material functions  $\lambda, \mu \in \mathcal{PC}^{const}(M(\Omega_R), \mathbb{R}_0^+)$  with  $\lambda(x) + \mu(x) > 0$  for all  $x \in \bar{\Omega}_R$ , and a displacement field  $u \in \mathcal{UPC}$ , the piecewise elastic regulariser is defined as*

$$\mathcal{S}_{\alpha,\lambda,\mu}^{pelas}[u] = \sum_{z=0}^m \alpha^z \int_{\Omega^z} \frac{\mu^z}{4} \sum_{\zeta,\eta=1}^d (\partial_{x_\eta} u_\zeta(x) + \partial_{x_\zeta} u_\eta(x))^2 + \frac{\lambda^z}{2} (\nabla \cdot u(x))^2 dx. \quad (5.13)$$

**Lemma 5.13** (Euler-Lagrange Equation for the Piecewise Elastic Regulariser). *The system of Euler-Lagrange equations and natural interface conditions for the piecewise elastic regulariser is given by*

$$\begin{aligned} -\alpha^z \mu^z \Delta u(x) - \alpha^z (\lambda^z + \mu^z) \nabla \cdot \nabla u(x) &= 0, & x \in \Omega^z, \\ \alpha^z (\mu^z (\nabla u(x) + (\nabla u(x))^T) + \lambda^z \text{diag}(\nabla \cdot u(x)), \mathbf{n}^z(x)) &= 0, & x \in \partial\Omega^z \setminus \partial\Omega, \end{aligned} \quad (5.14)$$

where  $z = 0, \dots, m$ .

*Proof.* By straightforward application of Lemma 3.16 and Lemma 5.6. ■

Having determined the Euler-Lagrange equations for different similarity and regularisation terms, we collect these results and build up a joint (system of) Euler-Lagrange equation(s). For the general functional  $\mathcal{J}$  as in (3.16) we obtain

$$\begin{aligned} L^z u(x) &= f(u(x)), & x \in \Omega^z, \quad z = 0, \dots, m, \\ B^z u(x) &= 0, & x \in \partial\Omega^z \setminus \partial\Omega, \quad z = 0, \dots, m, \end{aligned} \quad (5.15)$$

with

1) following from the similarity measure

$$f(u) := [R - T_u] \nabla T_u, \quad (5.16)$$

and, dependent on the choice of the regulariser,

2a) for the piecewise diffusive case

$$L^z := -\alpha^z \Delta, \quad (5.17)$$

$$B^z := \alpha^z (\nabla, \mathbf{n}^z), \quad (5.18)$$

2b) and for the piecewise elastic case

$$L^z := -\alpha^z \mu^z \Delta - \alpha^z (\lambda^z + \mu^z) \nabla \cdot \nabla, \quad (5.19)$$

$$B^z := \alpha^z (\mu^z (\nabla + \nabla^T) + \lambda^z \text{diag}(\nabla \cdot), \mathbf{n}^z). \quad (5.20)$$

Adding a boundary condition

$$Bu(x) = 0, \quad x \in \partial\Omega, \quad (5.21)$$

such as

$$B := \text{id} \quad (5.22)$$

for a Dirichlet type condition or

$$B := \partial / \partial \mathbf{n} \quad (5.23)$$

for a Neumann type condition, (5.15) and (5.21) form a boundary value problem. The deduced initial boundary value problem,

$$\begin{aligned}
\frac{\partial u(x, t)}{\partial t} &= -[L^z u(x, t) - f(u(x, t))] , & x \in \Omega^z , \ z = 0, \dots, m , \ t \in \mathbb{R}_0^+ , \\
B^z u(x, t) &= 0 , & x \in \partial\Omega^z \setminus \partial\Omega , \ z = 0, \dots, m , \ t \in \mathbb{R}_0^+ , \\
u(x, 0) &= u^{(0)}(x) , & x \in \bar{\Omega} , \\
Bu(x, t) &= 0 , & x \in \partial\Omega , \ t \in \mathbb{R}_0^+ ,
\end{aligned} \tag{5.24}$$

differs from (3.33) and (4.17) in the additional natural interface condition. Note that  $u^{(0)} : \bar{\Omega} \rightarrow \mathbb{R}^d$  serves as an initial function which is smooth at least on each region  $\Omega^z$ .

Before we proceed with the discretisation of (5.24) we conclude the section with an important remark.

**Remark.** Due to the choice of a solution space consisting of piecewise continuously differentiable functions, a solution  $u^*$  may describe a non-physically meaningful transformation resulting in an overlap or in a swap of regions.

Although, in an implementation these cases may not occur or may be circumvented by further restrictions, from a mathematical point of view, functions with these properties are possible solutions of the minimisation problem. To our best knowledge, a formulation of the minimisation problem which, on the one hand, allows for topological changes, and, on the other hand, prevents from a swap of regions or an overlap of non-background regions, is not known yet and describes a topic for future investigation.

### 5.3 Discretisation

For a discretisation of the initial boundary value problem (5.24) the framework developed in Section 3.4 is used. In particular we have  $\Omega = (0, 1)^2$ .

**Lemma 5.14.** *Given the initial boundary value problem in (5.24) with abbreviations (5.16)–(5.19), (5.22) and (5.23), a discretisation with a local order of accuracy of  $\mathcal{O}(h^2 + k)$  is given by*

$$\begin{aligned}
(\text{id}_h + kL_h^z)U^{i,j,l+1} &= U^{i,j,l} + kf_h U^{i,j,l} , & (i, j) \in \Omega_h^z , \ l \in \mathbb{N}_0 , \\
B_h^z U^{i,j,l+1} &= 0 , & (i, j) \in (\partial\Omega^z \setminus \partial\Omega)_h , \ l \in \mathbb{N}_0 , \\
U^{i,j,0} &= u^{(0)}(x_i, y_j) , & (i, j) \in \bar{\Omega}_h , \\
B_h U^{i,j,l+1} &= 0 , & (i, j) \in \partial\Omega_h , \ l \in \mathbb{N}_0 ,
\end{aligned} \tag{5.25}$$

where

1)  $f_h$  refers to the discretised similarity measure as in Lemma 3.17,



2a) for the piecewise diffusive case,  $L_h^z$  refers to the discretised operator

$$L_h^z = -\alpha^z \begin{pmatrix} \partial_{11}^\pm + \partial_{22}^\pm & 0 \\ 0 & \partial_{11}^\pm + \partial_{22}^\pm \end{pmatrix}, \quad (5.26)$$

and  $B_h^z$  is given by

$$B_h^z = \alpha^z \begin{pmatrix} \mathbf{n}_1^z \partial_1^\pm + \mathbf{n}_2^z \partial_2^\pm & 0 \\ 0 & \mathbf{n}_1^z \partial_1^\pm + \mathbf{n}_2^z \partial_2^\pm \end{pmatrix}, \quad (5.27)$$

2b) for the piecewise elastic case,  $L_h^z$  refers to the discretised operator

$$L_h^z = -\alpha^z \begin{pmatrix} (\lambda^z + 2\mu^z)\partial_{11}^\pm + \mu^z\partial_{22}^\pm & (\lambda^z + \mu^z)\partial_1^a\partial_2^a\partial_{12}^\pm \\ (\lambda^z + \mu^z)\partial_1^a\partial_2^a\partial_{12}^\pm & \mu^z\partial_{11}^\pm + (\lambda^z + 2\mu^z)\partial_{22}^\pm \end{pmatrix} \quad (5.28)$$

and  $B_h^z$  is given by

$$B_h^z = \alpha^z \begin{pmatrix} (\lambda^z + 2\mu^z)\mathbf{n}_1^z\partial_1^\pm + \mu^z\mathbf{n}_2^z\partial_2^\pm & \lambda^z\mathbf{n}_1^z\partial_2^\pm + \mu^z\mathbf{n}_2^z\partial_1^\pm \\ \mu^z\mathbf{n}_1^z\partial_2^\pm + \lambda^z\mathbf{n}_2^z\partial_1^\pm & \mu^z\mathbf{n}_1^z\partial_1^\pm + (\lambda^z + 2\mu^z)\mathbf{n}_2^z\partial_2^\pm \end{pmatrix} \quad (5.29)$$

3)  $B_h$  refers to the boundary operators as in Lemma 3.17,

respectively.

*Proof.* The derivation of the discretised operators differs from Lemma 3.34 only by the additional constant  $\alpha^z$  which neither complicates the discretisation nor affects the local order of accuracy. Furthermore, the discretisation of (5.27) and (5.29) involve solely second-order difference quotients and Lemma 2.12 can be applied to conclude the proof. ■

Since the discretised operators differ from those in Lemma 3.34 only by a factor, we refer for the stencil notation to Corollary 3.18.

Similarly to Section 3.4, a linear system of equation can be assembled, here with respect to each region,

$$\begin{aligned} \mathbf{A}^z \mathbf{U}^{z,(l+1)} &= \mathbf{U}^{z,(l)} + k \mathbf{F}^{z,(l)}, & l \in \mathbb{N}^0, \quad z = 0, \dots, m, \\ \mathbf{U}^{z,(0)} &= 0, & z = 0, \dots, m. \end{aligned}$$

## 5.4 Numerical Solution

Following the discretisation from the previous section, for each region  $\Omega^z$  an assembled system is to be solved for  $\mathbf{U}^{z,(l+1)}$  in each iteration step. Then, for given digital images  $R_h, T_h$  and discretisations of a piecewise constant regularisation function  $\alpha$ , and – in the case of the elastic regulariser – piecewise constant Lamé parameter functions  $\lambda$  and  $\mu$ , an algorithm reads as follows.

**Algorithm 5.15.**

```

choose  $U^{(0)}$  and  $k$ 
for  $l = 0, 1, \dots$  do
  for  $z = 1, \dots, m$  do
    compute force term  $F^z$ 
    assemble  $A^z$ 
    solve  $A^z U^{z,(l+1)} = U^{z,(l)} + k F^z$ 
  end
  compute transformed template image  $T_{U^{(l+1)}}$ 
end

```

In addition to the remarks given in Sections 3.5 and 4.5 it is worth to notice that

- Algorithm 5.15 computes the displacement field for the regions  $\Omega^1, \dots, \Omega^m$  only and not for background structures of the image which are included in  $\Omega^0$ ,
- due to the decomposition into regions, instead of one system of large size,  $m$  systems of equations of smaller size have to be solved which require less effort in terms of computational time and storage,
- due to the constant parameter functions in each region, fast solving routines as described, for instance, in (FISCHER & MODERSITZKI, 1999, 2002, 2004) can be employed,
- the computation of the transformed template image  $T_{U^{(l+1)}}$  requires particular care: Assuming the situation of two regions being adjacent in the template image but separated from each other in the reference image (i.e., a topological change occurs), a gap is required to open between the regions while transition from the template onto the reference image. Since the interpolation of  $T_{U^{(l+1)}}$  takes place in the domain of the template image,  $\Omega_T$ , additional knowledge is essential to ensure the opening of a gap in the reference image.

Motivated by a setting as depicted in Figure 4.2 we introduce a *virtual gap*. Here, we are faced with two regions  $\Omega^1, \Omega^2$  separated by a gap (belonging to a region  $\Omega^0$  collecting all background structures) of small width in the template and of large width in the reference image. Clearly, the common boundary  $\Gamma^{1,2}$  is a zero set as long as there exists a positive lower bound for the width of the gap. Employing a registration algorithm with an appropriate grid spacing  $h$ , a common interpolation scheme can be used to assign a grey-value out of the gap in the discretised template image to the corresponding position within the gap in the discretised reference image. However, by shrinking the (physical) gap in the template image such that  $\Gamma^{1,2} \neq \emptyset$ , a common interpolation scheme fails since the gap is no longer contained in a discretisation of the template image regardless of the choice of  $h$ . At this point, a virtual gap comes into play and acts in the same way as a (physical) gap.

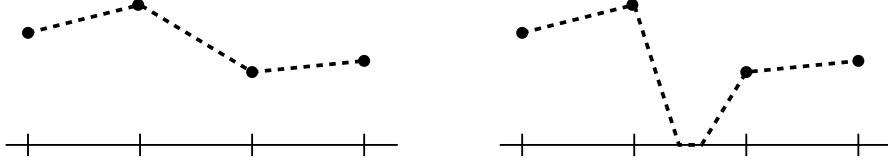


Figure 5.3: Results of using a linear interpolation operator  $\mathcal{I}$  (left) and of using a combination of  $\mathcal{I}$  and  $\mathcal{I}_{virt}$  referring to a virtual gap located between the two centre positions (right). Note that the grey-value of the virtual gap can be arbitrarily chosen.

As a drawback, a decomposition of the template image is required in addition to the one of the reference image. Moreover, this decomposition  $M(\Omega_T)$  is required such that each region  $\Omega_T^z$  corresponds intrinsically to a region  $\Omega_R^z$  from the decomposition  $M(\Omega_R)$ . With domain discretisations  $\{\Omega_{h,R}^z\}_{z=0}^m, \{\Omega_{h,T}^z\}_{z=0}^m$  the set of positions with nearest neighbouring points belonging to  $\Omega_{h,T}^z$  and to a neighbouring discretised region can be described as

$$\Gamma^z := \{x \in \Omega \mid \mathcal{B}_{\infty,1}(x) \cap \Omega_h^z \neq \emptyset \wedge \mathcal{B}_{\infty,1}(x) \cap \Omega_h^{\hat{z}} \neq \emptyset \text{ for all } \hat{z} \neq z\}$$

where  $\mathcal{B}_{\infty,1}(x) := \{y \in \Omega \mid \|y - x\|_{\infty} < 1\}$  denotes a neighbourhood with respect to the  $l^{\infty}$ -norm with radius 1 around  $x$ . Then, given a discrete position  $x_{i,j} \in \Omega_R^z$ , the grey-value of  $T$  at the transformed position is determined by

$$T_U^{i,j,l+1} := \begin{cases} \mathcal{I}(T_h, x_{i,j} + U^{i,j,l+1}) & , x_{i,j} + U^{i,j,l+1} \notin \Gamma^z \\ \mathcal{I}_{virt}(T_h, x_{i,j} + U^{i,j,l+1}) & , x_{i,j} + U^{i,j,l+1} \in \Gamma^z \end{cases} \quad (5.30)$$

with  $\mathcal{I}$  as a linear interpolation operator.  $\mathcal{I}_{virt}$  denotes the interpolation operator acting in the virtual gap region and can be defined, e.g., as depicted in Figure 5.3.

Summarising, a numerical scheme enabling for topological changes is achievable but requires additional knowledge given by decompositions into sets of regions corresponding intrinsically to each other. Furthermore, a solution of the proposed scheme is not guaranteed to show neither a swap of regions nor an overlap of two non-background regions.



---

## 6 Results

---

The proposed methods from Chapter 4 and Chapter 5 have been applied to various image registration problems. In order to investigate the properties of the methods, we start with the application to synthetic images in one and two dimensions. Here, a ground truth is available and allows for an objective evaluation of the resulting displacement field. We proceed with the investigation of medical applications where a ground truth is not available in general.

### 6.1 Synthetic Images

We start with the registration of synthetic images, and turn our attention first towards the weighting function,  $\alpha$ . To this end, we revisit the one-dimensional problem depicted in Figure 4.3. A similar problem, but in two dimensions, has been introduced in Figure 4.2, which we consider next. Then, by extending the variability to the Lamé parameters, the introductory registration problem from Figure 4.1 can be solved successfully. Next, we consider a rotation problem as an example for the embedding of a rigid object in an elastic surrounding. Finally, an elastic phantom will be investigated.

These images have been chosen to illustrate the behaviour of the proposed approaches for different settings as they are likely to occur with clinical applications.

#### 6.1.1 1D Case

To outline some fundamental properties of the variable regularisation, we begin with a one-dimensional problem. The problem is similar to the one from Figure 4.3 but now with five objects, cf. Figure 6.1, top row, for the template image  $T$  and the reference image  $R$ . For the outer objects, there is no change in position during transition from  $T$  to  $R$ . The other objects are designed such that they indeed change their positions in such a way that gaps between them either enlarge or shrink, or, when employing a piecewise variable regulariser, in such a way that gaps show up or disappear.

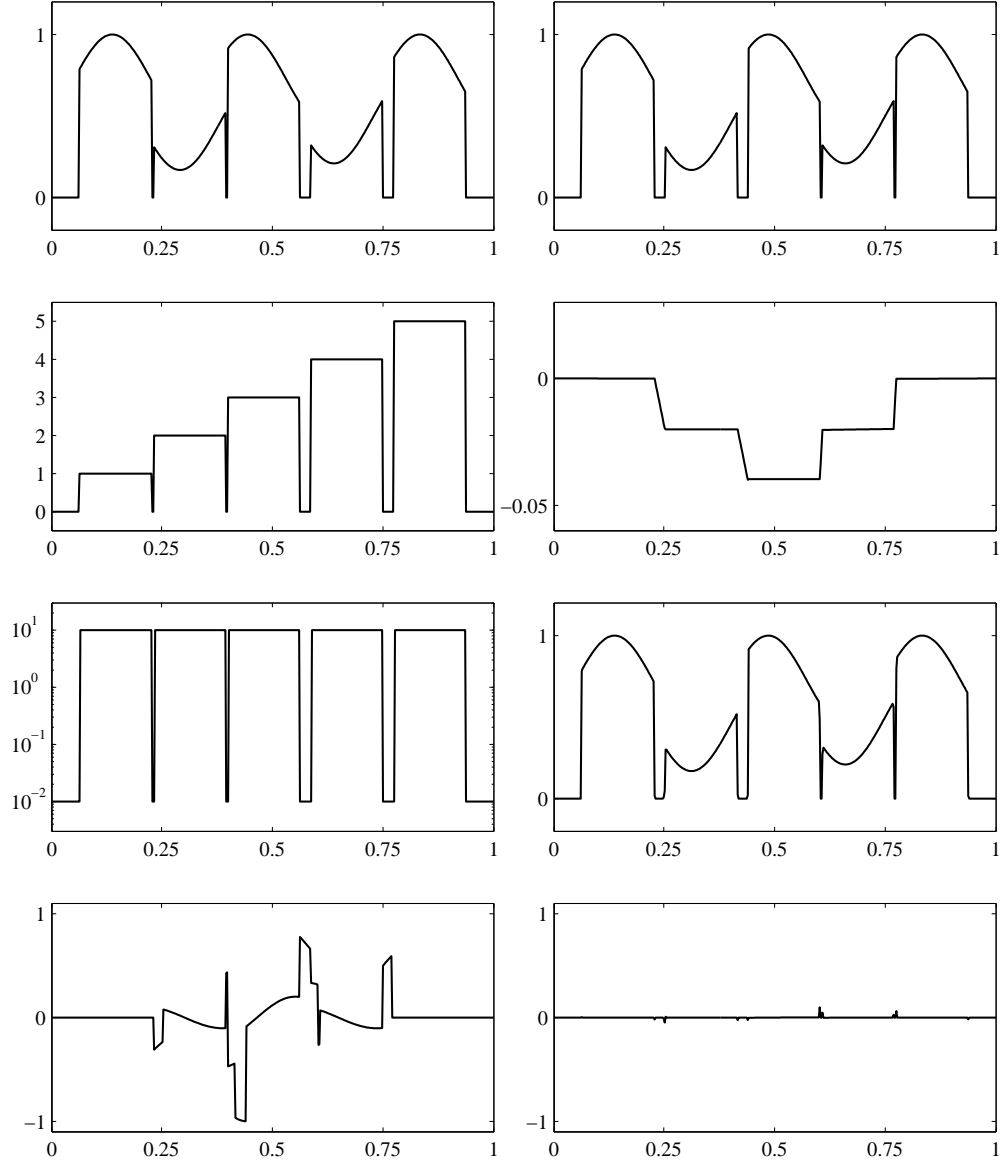


Figure 6.1: Template  $T$  and reference image  $R$  are shown in the upper row. Below, from top to bottom, the left column shows the segmentation of  $T$ , the deduced values for  $\alpha$ , and the subtraction image  $R - T$  whereas in the right column the resulting displacement function  $U$ , the transformed template image  $T_U$ , and the subtraction image  $R - T_U$  are depicted.

We investigate various settings and consider at first a registration scheme based on the variable diffusive regulariser.

### Variable Regulariser

For a spatially variable regularisation, a segmentation of the template image  $T$  is required. Each object of  $T$  (given by an interval with non-zero grey-values) belongs to a single region  $\Omega^z$ ,  $z = 1, \dots, 5$ , of the decomposition  $M(\Omega_T)$  whereas

the rest of the image is treated as a background region  $\Omega^0$ . The decomposition is encoded in the segmented template image by assigning an integer value to each region (cf. Figure 6.1, second row, left). From the segmented template image, we deduce the values of the weighting function  $\alpha$  (shown below). By setting  $\alpha$  to a small value in background regions, we expect a displacement function  $u$  which is constant within each object and exhibits high gradients between them.

An application of the variable diffusive regulariser with  $\alpha(x) = 10$  for  $x \in \Omega^z$ ,  $z = 1, \dots, 5$ ,  $\alpha(x) = 0.01$  for  $x \in \Omega^0$ , and equipped with Dirichlet boundary conditions fulfills our expectations well. As is apparent from the right column in Figure 6.1, the displacement function  $U$  (second row) shows a constant displacement within the objects with abrupt changes between them. In addition, the transformed template image  $T_U$ , depicted below, indicates a registration result that coincides with the reference image. The differences between these two images are negligible as can be seen from the subtraction image  $R - T_U$  in the bottom row.

Note that a similar result may be obtained when applying a constant but very small  $\alpha$ . However, this problem becomes increasingly ill-posed with decreasing  $\alpha$ , and therefore requires a smaller step size.

### Variable Regulariser in the Presence of Noise

To test the proposed method in a more realistic setting, we modify the reference image by adding white noise with a standard deviation of 10% of the previous grey-value scale (Figure 6.2, top right). The template image and  $\alpha$  remain unchanged. The situation of a reference image with a higher noise level corresponds to registration problems with a pre-operatively generated image of high quality and an intra-operatively generated one of lower quality. Since both the segmentation and interpolation of grey-values are done with respect to the template image, the noise neither influences the correct installation of the weighting function nor affects the grey-values of the transformed template image. The ideal displacement field for this setting remains the same as for the original reference image.

Now, the variable diffusive regulariser is applied with both a varying and a constant weighting function. As shown in Figure 6.2, center and bottom right, a constant choice of  $\alpha$  (here  $\alpha \equiv 0.03$ ) fails. In particular, the gap regions are penalized such that a large difference in the grey-values is preferred over a large gradient in the displacement. Consequently, neither the gaps between  $\Omega^3$  and  $\Omega^5$  close to the expected extent nor the gaps between  $\Omega^1$  and  $\Omega^3$  enlarge successfully. In contrast, a variable weighting (the same as for the noiseless setting) is able to cope with the presence of noise in the reference image. It simultaneously supports a noise-independent smooth displacement within the objects and allows for a treatment of high gradients in the gap regions as shown in Figure 6.2, center and bottom left.

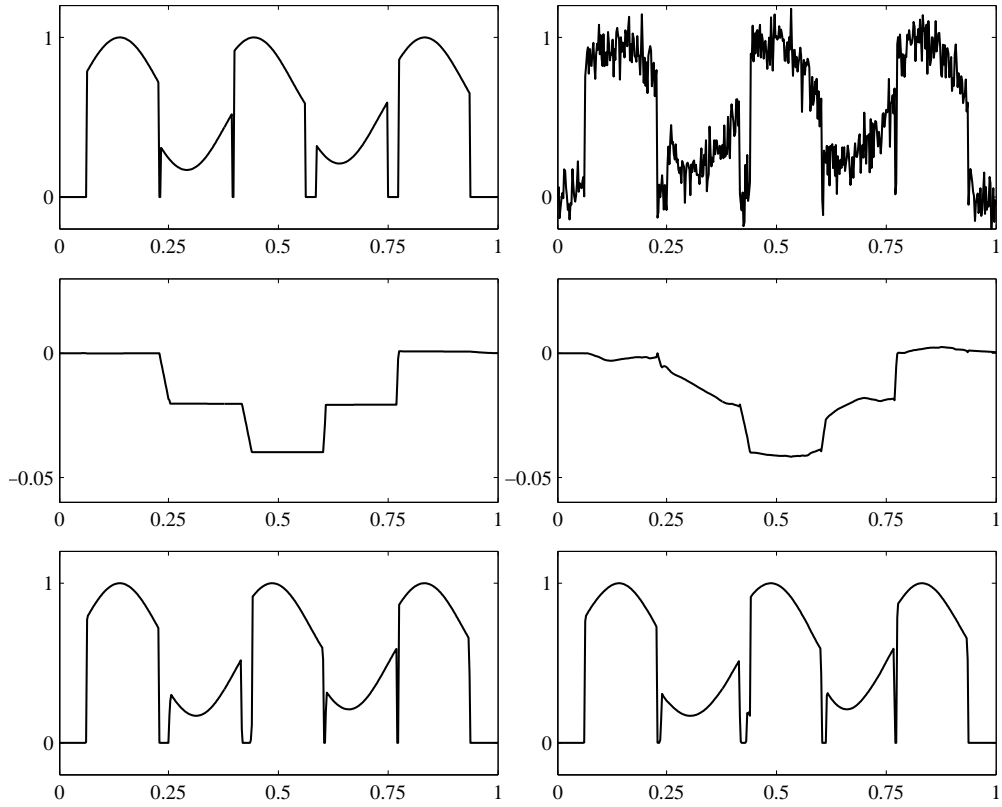


Figure 6.2: Template  $T$  and noised reference image  $R$  are shown in the upper row. Below, the left column depicts the registration result using a variable weighting function, whereas the right columns corresponds to the one using a constant weighting function. In the center row each of the displacement functions is depicted, the bottom row shows the transformed template image.

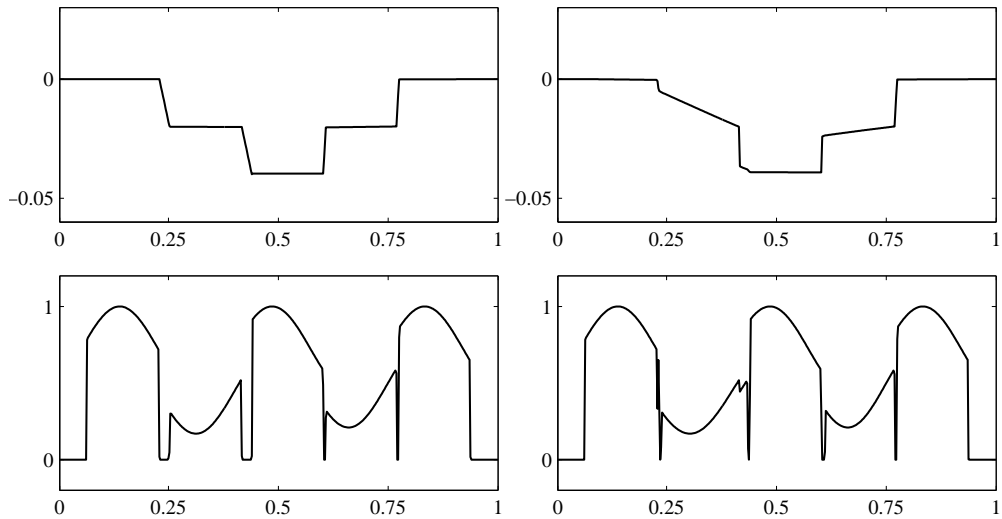


Figure 6.3: Displacement function and transformed template image are depicted using a segmentation of the template image (left) and one of the reference image (right).



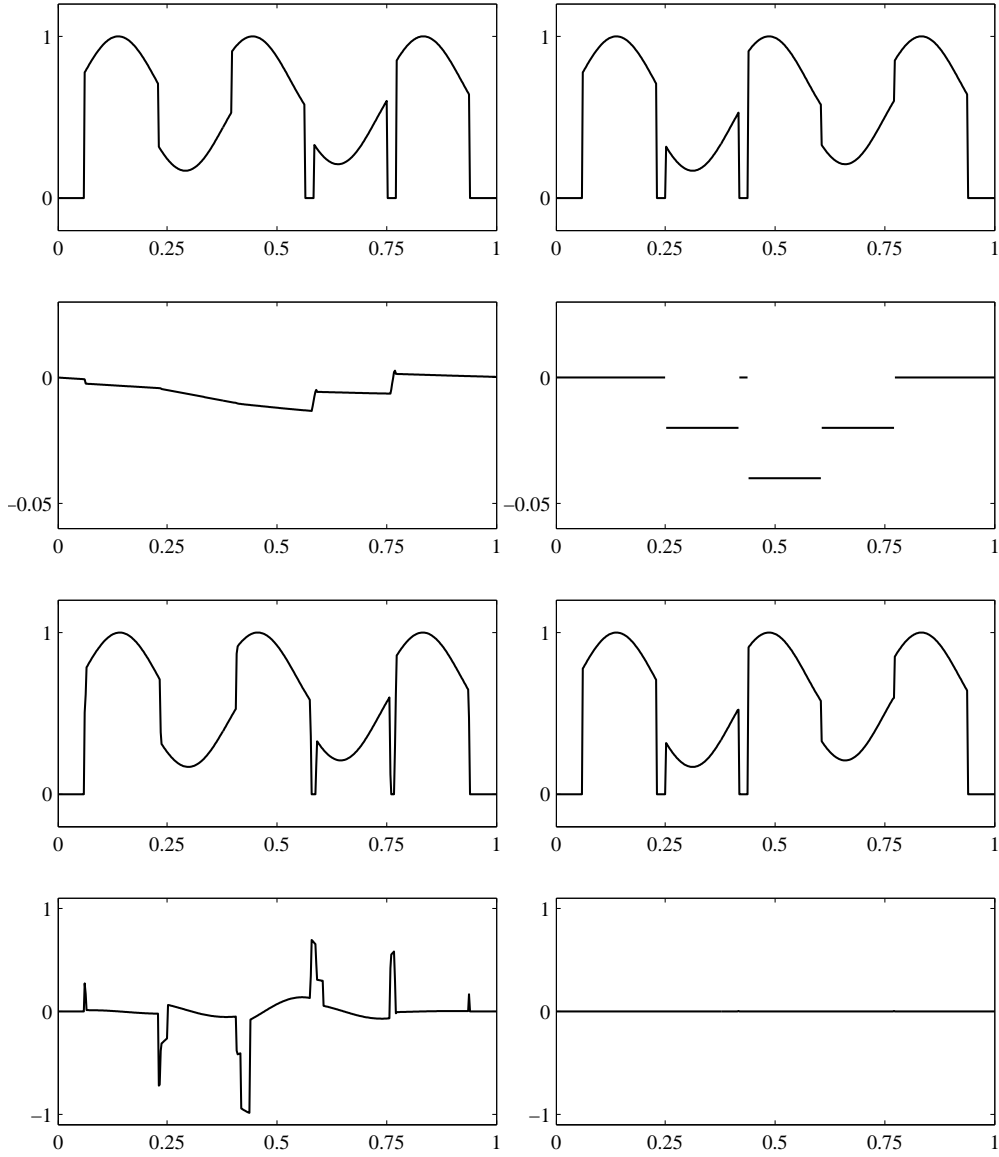


Figure 6.4: Template  $T$  and reference image  $R$ , now with gaps of zero size, are shown in the upper row. Below, the left column refers to the variable diffusive regulariser whereas the right column to the piecewise diffusive regulariser. From top to bottom are shown the resulting displacement function  $U$ , the transformed template image  $T_U$ , and the subtraction image  $R - T_U$ .

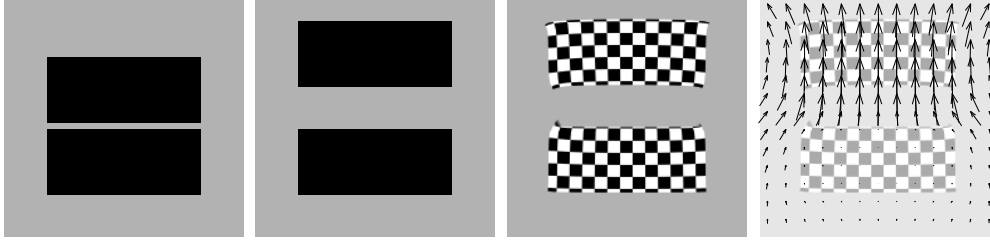


Figure 6.5: Template (left) and reference image (center left) are displayed together with the resulting transformed template image (center right) and a visualization of the displacement field on a coarsened grid (right).

### Variable Regulariser with a Segmentation of the Reference Image

The variable regularisers can be modified in order to employ a segmentation of the reference rather than one of the template image. This modification causes the parameter functions to evolve no longer in time, instead they remain fixed throughout the iterative procedure.

However, as discussed in Section 4.3, a change of the image to be segmented may lead to a failure in registration if large segmented overlap regions exist. For the given registration problem, such regions can be detected in the subtraction image (see Figure 6.1, bottom left) between  $\Omega^2$  and  $\Omega^3$  as well as between  $\Omega^3$  and  $\Omega^4$ .

From Figure 6.3, right, a failure in registration can be observed. For comparison, the result using a segmentation of the template image is depicted on the left.

### Piecewise Variable Regulariser

In a final modification step the gap width in template and reference image is reduced from two voxel spacings to zero. Now, as can be seen from Figure 6.4, top row, three regions in each image are no longer separated from each other by a gap of zero grey-value – the large gap changes are replaced by topological changes.

An application of the variable diffusive regulariser suffers from the unchanged weighting function between  $\Omega^1$  and  $\Omega^2$  as well as  $\Omega^2$  and  $\Omega^3$  and results in a dissatisfying displacement. In contrast, a piecewise variable diffusive regulariser additionally equipped with a segmentation of the reference image leads to a correct displacement (cf. Figure 6.4, right). Note that the use of a virtual gap as defined in (5.30) has been essential for a successful registration.

#### 6.1.2 2D Case

The investigation of the variable regularisers is continued with several two-dimensional problems. We begin with a two-dimensional registration problem of the same type as in the previous section.

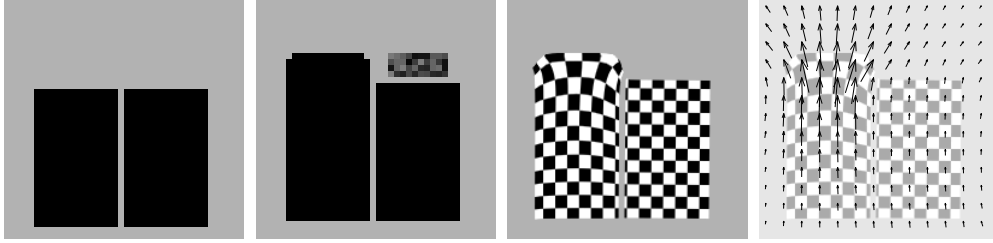


Figure 6.6: Template (left) and reference image (center left) are displayed together with the resulting transformed template image (center right) and a visualization of the displacement field on a coarsened grid (right).

### Spatially Varying Regularisation

Recalling from Figure 4.2 the two-dimensional problem consisting of two objects with a gap of variable size between them, we observed in Section 4.1 that a constant choice of  $\alpha$  does not lead to a satisfactory result – either the gap is enlarged to its expected size but the shape of the objects is changed or the size of the gap remained small while the shape of the objects is preserved.

In contrast, a variable choice of  $\alpha$  achieves the desired result (cf. Figure 6.5). Here we choose  $\alpha(x) = 1/4$  and  $\alpha(x) = 1/64$  inside and outside the objects, respectively,  $\lambda \equiv 2$  and  $\mu \equiv 4$ , and employ a registration scheme based on the SSD measure and the variable elastic regulariser equipped with Neumann boundary conditions. Note that the choice of Neumann conditions is natural. Choosing Dirichlet conditions would damp the displacement near to the image boundary which does not reflect the problem setting.

### Spatially Varying Regularisation and Material Parameters

In this example, we combine a variable choice of  $\alpha$  with a variable choice of the Lamé parameters and choose the registration problem that served as the first example in Chapter 4. Here, two objects were considered, the left one representing a soft-tissue structure, the right one a bone structure. Without any variable parameters we observed a dependence of the movements of the objects on each other and, additionally, a corruption of the right object caused by the noise artefact. Although, by choosing variable material properties the right object could be correctly registered, the cross-dependency remained existent, cf. Figure 4.1.

With a setting of  $\alpha(x) = 1/64$  and  $\alpha(x) = 1/128$  inside and outside the objects, respectively,  $\lambda \equiv 2$  as well as  $\mu(x) = 4000$  and  $\mu(x) = 4$  inside and outside the right object, respectively, a displacement field can be obtained where each object deforms independently of each other: whereas the left one is stretched, the right object is neither affected by the left one nor by the noise artefact.

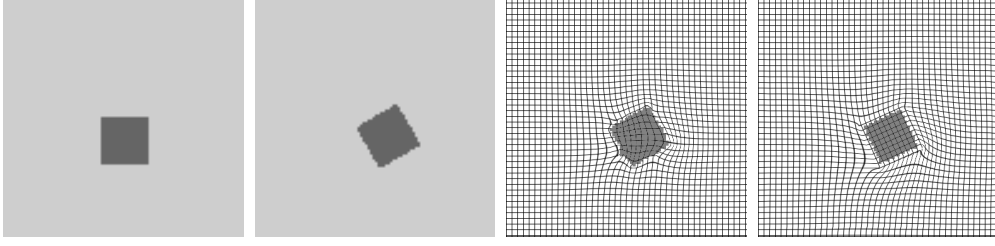


Figure 6.7: Template (left) and reference image (center left) are displayed together with visualized displacement fields for a constant  $\mu$  (center right) and a spatially varying  $\mu$  (right).

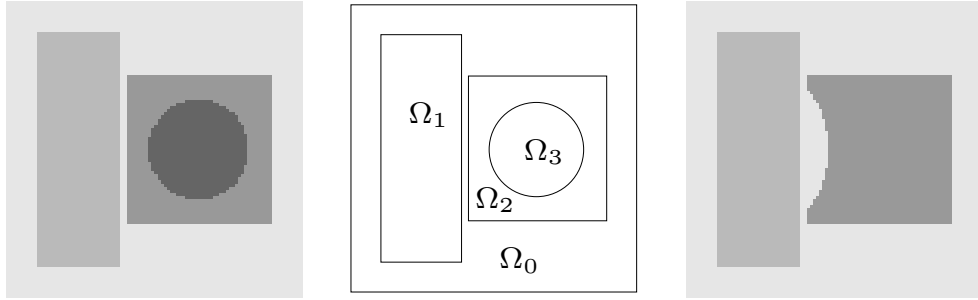


Figure 6.8: From left to right, template, segmented template, and reference image for the elastic phantom are shown.

### Rotation

As an extension to the previous example we investigate the shape-preservation property<sup>1</sup> of the variable elastic regulariser in more detail. To this end, a template image with a square is given. A rotation by  $30^\circ$  yields the reference image, cf. Figure 6.7. While in the first experiment all parameters are chosen constant ( $\alpha \equiv 0.1$ ,  $\lambda \equiv 0.1$ , and  $\mu \equiv 4$ ), in the second experiment  $\mu$  is multiplied by 1000 in the square region. Although, after the same number of iterations, both transformed template images almost match the reference image, the varying parameter case (cf. Figure 6.7, right) is clearly preferred since it results in a more realistic displacement field, e.g. for a muscle-bone interface.

### Elastic Phantom

The last synthetic example considers a two-dimensional elastic phantom. Here, our aim is to define a parameter setting which can be used in medical applications. The template image (Figure 6.8, left) consists of three objects: a rectangular object representing, for instance, bone structure, a square object modelling some soft tissue and in its inside a circle object taking the role of, for instance, a tumor. A decomposition assigns regions  $\Omega^1$ ,  $\Omega^2$ , and  $\Omega^3$  to these objects. The remaining part of the template image is collected in a background region  $\Omega^0$ , cf. Figure 6.8, center. For the transition from the template to the

<sup>1</sup>In fact, we have a penalizing term which does not guarantee for a preservation of shape and, instead, only approximates a preservation of shape.

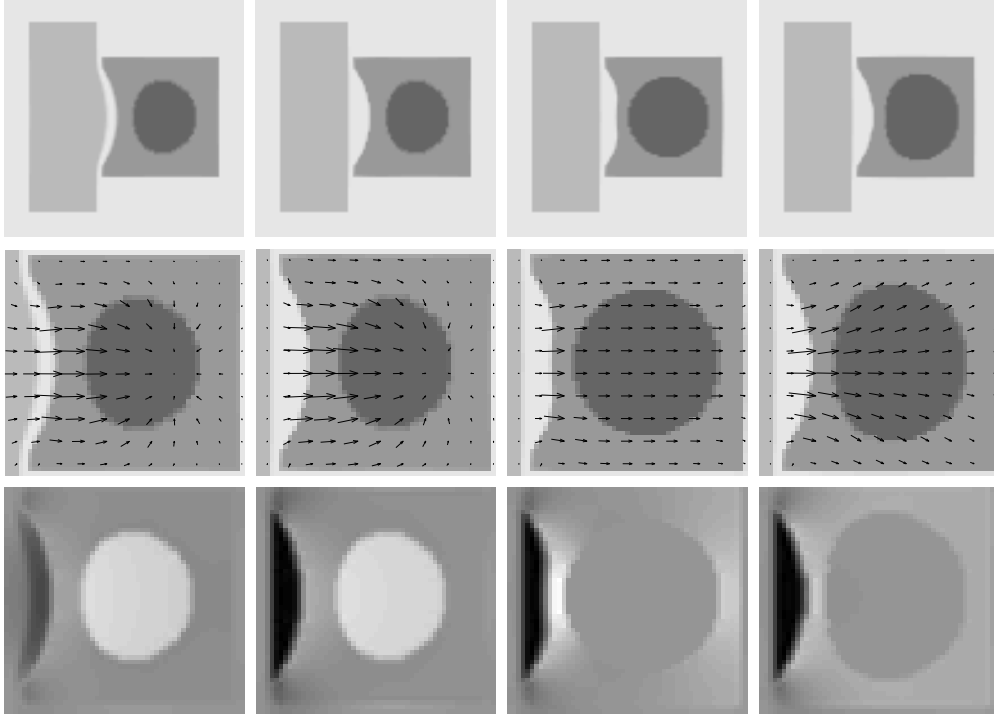


Figure 6.9: The results from four different settings are depicted columnwise with respect to  $T_U$  (top row), the overlaid displacement field (center row; data are thinned out for better recognition), and the volume preservation indicator  $|1 + \nabla u|$  (bottom row), cf. text for further details.

reference image (see Figure 6.8, right), we model a shrinkage of the tissue object without affecting the bone object, which is, as mentioned before, a challenge in standard registration approaches. The second problem regards the behaviour of the circle object. Due to its invisibility in the reference image, a standard registration approach will tend to shrink its size in order to relate it as much as possible to a circle of zero size.

The variable elastic regulariser is employed with four different parameter settings. For the first setting, all parameters are constant ( $\alpha \equiv 0.1$ ,  $\lambda \equiv 0.1$ ,  $\mu \equiv 4$ ), cf. the first column of Figure 6.9. For the remaining settings,  $\alpha$  is reduced locally in  $\Omega^0$  ( $\alpha = 0.015$ ). In addition,  $\mu$  (cf. third column) and  $\lambda$  (cf. fourth column) are multiplied by 1000 for the circle object  $\Omega^3$ .

After the same number of iterations, the resulting deformation fields are compared with respect to the deformed template image (top row in Figure 6.9) and for a zoomed region around the square object with respect to the displacement field (center row) and the quantity  $|1 + \nabla u|$  (bottom row). Here, a volume preserved region (corresponding to  $|1 + \nabla u| = 1$ ) is depicted by medium grey, whereas a contracting (expanding) region appears in light grey (dark grey).

Recalling the first problem, the shrinkage of the tissue object  $\Omega^2$  without affecting the bone object  $\Omega^1$  works properly whenever the weighting of the regulariser is small between  $\Omega^1$  and  $\Omega^2$  (second to fourth column). For the second problem, several observations can be made. With no further material knowledge,

the tumor object  $\Omega^3$  is shrunk (reduction in volume is 30%), indicated by a light grey of the circle object in the bottom row. With a large  $\mu$  or  $\lambda$ , either an approximated shape (and volume) preservation (third column) or an approximated volume preservation only (fourth column) can be seen. For both cases the change in volume is less than 0.3%.

## 6.2 Medical Images

In this section, the application of the proposed method to data sets from a CT and an MR image device is described. The first application originates from an exposure of the knee, the second one shows the abdomen whereas the third application is based on an exposure of the brain. Since real-life images are three-dimensional, slices need to be extracted first in order to employ the proposed algorithm. Then, template and reference image are two-dimensional images and can be treated by the registration scheme. However, such a procedure assumes the content of both template and reference image to be the same, i.e. to each anatomical structure the existence of a corresponding structure in the other image is assumed or, in other words, the displacement in the third spatial component is negligibly small.

### 6.2.1 Kinematic Imaging

As the first real-life example an application concerning the assessment of the kinematic motion of joints has been investigated. Template and reference image show sagittal slices (of  $256 \times 256$  voxels) from an MR exposure of a human knee at different degrees of flection. Whereas the template image  $T$  shows a nearly straightened knee joint, it is depicted with an angle of about  $35^\circ$  in the reference image  $R$ , cf. Figure 6.10, top row.

A series of such images is typically given in kinematic imaging (BYSTROV ET AL., 2005). Firstly, every pair of subsequent images is registered from which a mapping between any two images can be deduced. Secondly, in one image a number of positions is chosen by a physician such that, based on the mappings, the other images can be automatically aligned according to the one selected. For instance, when selecting the template image in Figure 6.10 and choosing three positions in the femur, all images in the series are aligned such that the femur is always located in the same position, independent of movement of the patient.

As part of this thesis, we investigate the first step which is the key part and determine a displacement field for the given image pair. For the transition from  $T$  onto  $R$  we expect a displacement field with the largest deformation in the region corresponding to the knee joint, see the subtraction image  $R - T$  shown bottom right. In contrast, in the regions corresponding to the femur and tibia bones, a rigid transformation is a reasonable assumption.

The registration is performed using the standard method with constant parameters and the proposed method based on a segmentation of the template image. As depicted in Figure 6.10, bottom left, the segmentation shows four regions

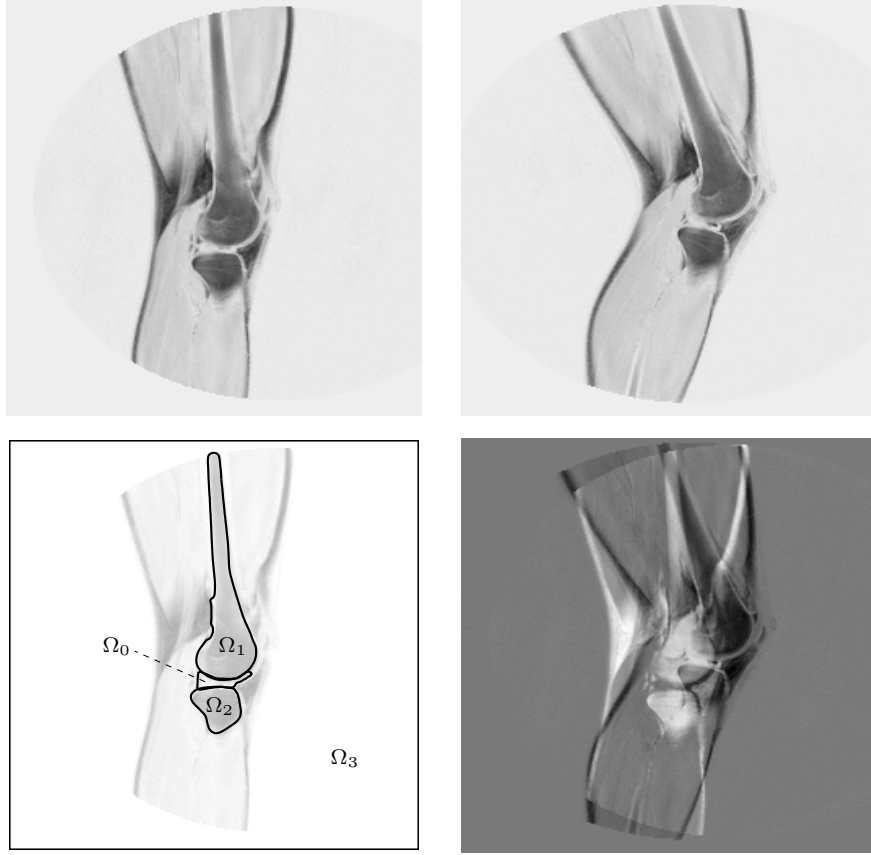


Figure 6.10: Template and reference image for the kinematics application are shown top left and top right, respectively (the grey-values are inverted for better recognition). Below, the segmented template and the subtraction image are depicted.

$\Omega^0, \dots, \Omega^3$  corresponding to articular capsule, femur, tibia, and the remaining part of the image which are obtained by repeated application of the active contour approach, cf. Section 4.2.2.

For both experiments, a registration scheme including the SSD measure and a diffusive regularisation, supplemented by Neumann boundary conditions, is employed. In the first experiment, a constant regularisation weight ( $\alpha \equiv 0.025$ ) is chosen; in the second,  $\alpha$  is increased for the bone structures and decreased for the articular capsule, i.e.  $\alpha(x) = 25$  for  $x \in \Omega^1 \cup \Omega^2$  and  $\alpha(x) = 0.005$  for  $x \in \Omega^0$ . In both experiments, a multi-resolution pyramid with four levels and a coarsest resolution of  $32 \times 32$  voxels is employed to increase robustness and reduce the computational effort of the scheme.

The results are shown in Figure 6.11. The two columns on the left-hand side correspond to the constant setting whereas the two columns on the right depict the results for the varying setting.

A comparison reveals no visible improvement for the deformed template at a first glance (see first and third image in the top row). Moreover, the subtraction images (second and fourth) indicate a better fit for the constant setting than for the variable setting. However, when zooming in the bone area (first and third

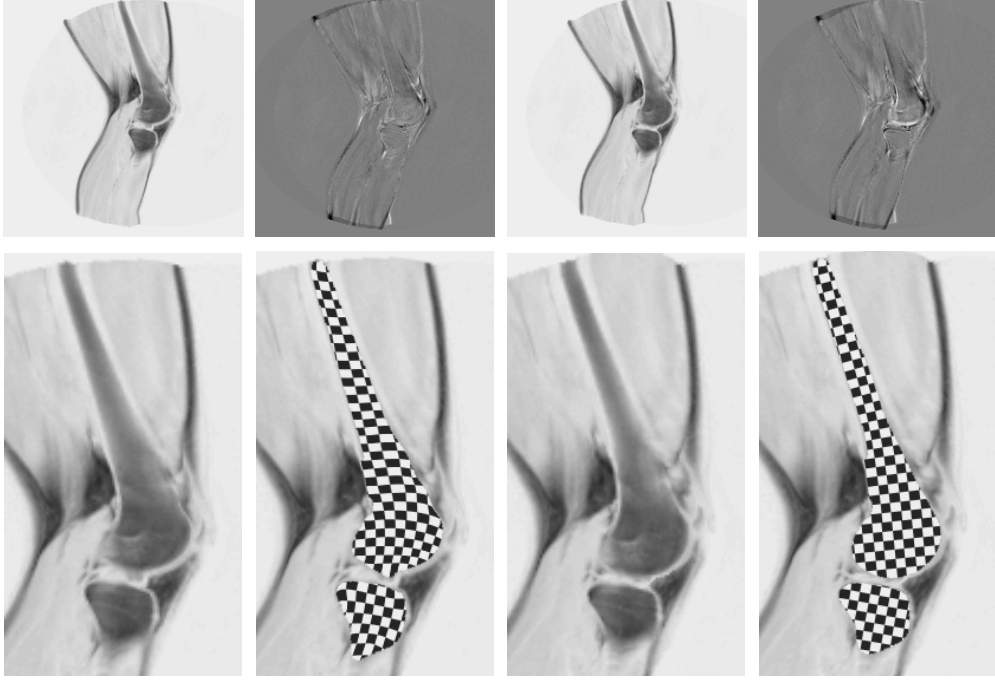


Figure 6.11: Results for the case with constant parameters (first and second column) and for the case with variable parameters (third and fourth column). For each case the top row depicts deformed template and subtraction image, in the bottom row zooms into the deformed template are shown. See text for further details.

image in the bottom row) and filling  $\Omega^1$  and  $\Omega^2$  (retrospectively the registration) with a chequerboard pattern, a non-rigid deformation of both femur and tibia becomes visible (second image in bottom row). Moreover, the shape of the femur near to the articular capsule is deformed. This is caused by a structure included in the reference image but not in the template image leading to a downward movement of the femur. Such a failure of registration does not happen for the second experiment. Here, the bone structures are rigidly displaced and the result is not misled in the region of the articular capsule (bottom right).

### 6.2.2 Radiotherapy Planning

In the second medical example, CT exposures<sup>2</sup> of the abdomen are investigated. They are taken from the same patient but at different times. Such images are typically acquired in the form of follow-up studies to monitor the progress of treatment and to adjust a treatment plan to changes caused by different patient positioning or tumor response during radiation therapy, see, e.g., (PEKAR ET AL., 2004; KAUS ET AL., 2004) for examples or (KEALL, 2004) for further explanation.

Often, images from the abdomen differ not only due to a different patient position but, which is more importantly, due to different colon content as is apparent from the extracted slices (image size is  $256 \times 256$  voxels) in Figure 6.12,

<sup>2</sup>Image courtesy of William Beaumont Hospital, Royal Oak, MI.



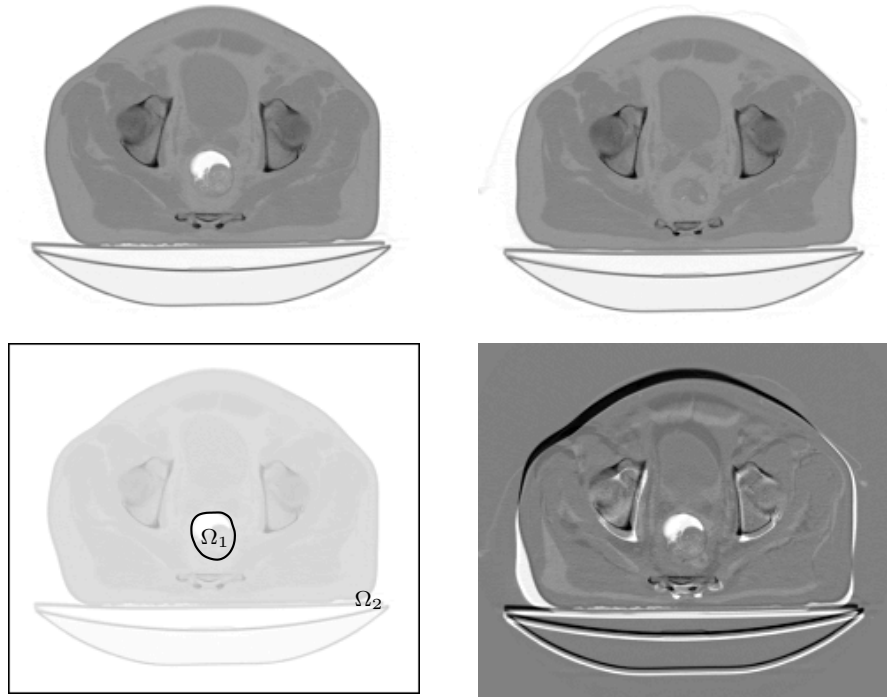


Figure 6.12: Template  $T$  (top left) and reference image  $R$  (top right) together with the subtraction image  $R - T$  (bottom right) and the segmented template (bottom left).

top row (for visualization purpose the grey-values are inverted). Although the colon content is in general not relevant for the planning procedure, it may influence the registration result. In such a situation, a standard registration of the template image  $T$  onto the reference image  $R$  typically shrinks the colon which causes a shrinkage in the surrounding regions as well.

For the registration, we combine the SSD measure with the variable elastic regulariser supplemented by Neumann boundary conditions. In the first experiment, the parameters are set constant ( $\alpha \equiv 0.005$ ,  $\lambda \equiv 0$ , and  $\mu \equiv 4$ ) reflecting the standard approach. For the second experiment, the colon is segmented in the template image first. Figure 6.12, bottom left, depicts the segmentation with  $\Omega^1$  as the colon region and  $\Omega^2$  as the remaining part of the image. The same choice of parameters as in the first experiment is used except from the colon for which  $\mu = 4000$  is set in  $\Omega^1$ . A multi-resolution pyramid with four levels and a coarsest resolution of  $32 \times 32$  voxels is employed for both experiments.

Figure 6.13 depicts the result for the first experiment in the left column. Although the global alignment is satisfactory (cf. the subtraction image in the center row), the colon region as well as the surrounding organs are shrunk as apparent from the displacement field depicted below. The result for the second experiment (cf. the right column in Figure 6.13) differs from the first one in the colon region. Due to the increased value of  $\mu$  in  $\Omega^1$ , this region shows a displacement field which is not affected by the different image content within the set  $\Omega^1$ .

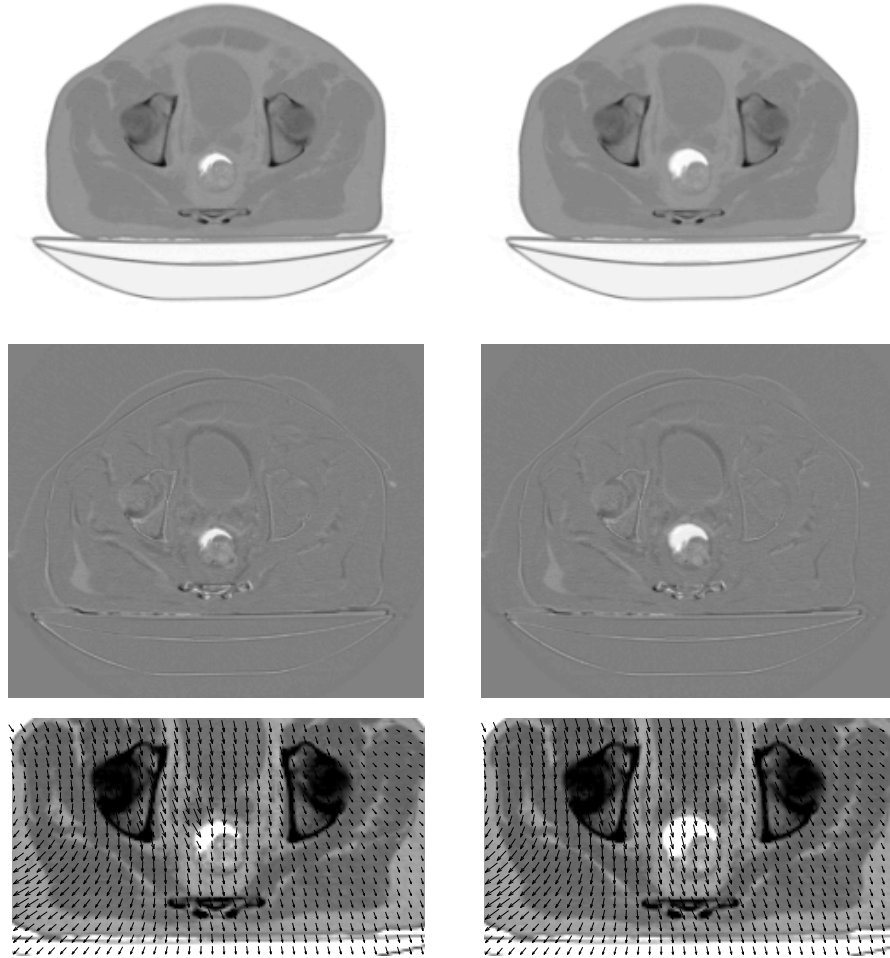


Figure 6.13: Registration results for the standard approach (left) and the proposed approach (right). From top to bottom each column shows the deformed template  $T_U$ , the subtraction image  $R - T_U$ , and the deformation field.

### 6.2.3 Brain Shift

Finally, slices from two MR data sets<sup>3</sup> showing a human head are registered. The template data set has been taken pre-operatively whereas the reference data set shows the head in an intra-operative state, cf. Figure 6.14 for sagittal slices (the grey-values are inverted for better perception). In the reference data set we observe the skin as the darkest structure being partially put aside and the skull being opened. Furthermore, a shrinkage of the brain is visible. This phenomenon, known as brain shift, is caused by a loss in pressure after opening the dura. It leads to a shrinkage of the brain and can reach up to 20 mm at the surface of the brain and up to 6 mm at the inter-hemispheric fissure (GANSER ET AL., 1998). However, the principal direction of displacement does not al-

<sup>3</sup>Image courtesy of Dr. Hastreiter, Department of Neurosurgery, Friedrich Alexander University of Erlangen-Nuremberg.

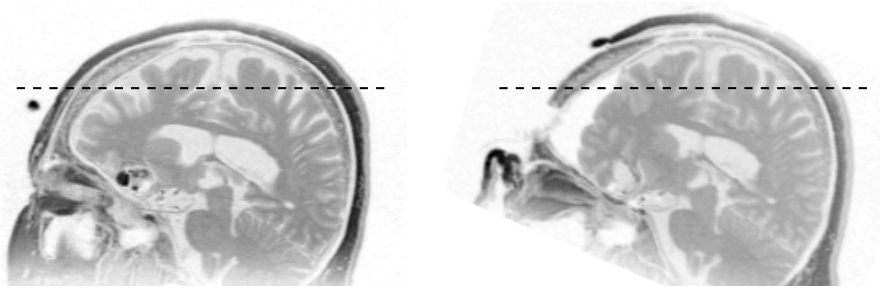


Figure 6.14: Sagittal slices from MR data sets showing a patient in a pre-operative state (left) and in an intra-operative one (right). The dashed lines indicate the positions of the transversal images to be extracted for the registration.

ways correspond with the direction of gravity (HARTKENS ET AL., 2003). As a consequence, a pre-operatively determined position in the template data set of, for instance, a tumor or a lesion cannot be used in the reference data set and a further possibly time-consuming analysis is needed. However, the quality and/or the resolution typically differs between a pre-operatively taken data set and an intra-operatively generated one. Therefore, the detection of a tumor or a lesion may be harder in the reference data set, i.e. in the one of lower quality or resolution. Nevertheless, a registration of the template onto the reference data set provides both a mapping of the detected position into the reference domain and a depiction of the intra-operative state at the same quality than for the pre-operative state.

From the 3D data sets transversal slices of size  $256 \times 256$  are extracted along the dashed lines in Figure 6.14. The extracted slice from the pre-operatively generated data set serves as template image  $T$ , the one from the intra-operatively generated data set as reference image  $R$  (depicted in Figure 6.15, upper row). The challenge arising with the registration task is twofold. Firstly, the skin is partly missing in the reference image. By a standard registration scheme such a non-existent region is usually either shrunk or moved to a position which is incorrect but, due to grey-value correspondences, preferable from the view of the minimiser. The second difficulty concerns the enlarged region in the right hemisphere between skull and brain caused by the shrinkage of the brain. Here, as seen before for synthetic images, a standard registration scheme is usually not able to successfully treat such an opening unless the regularisation parameter is decreased in such an amount that other image regions undergo a change in topology.

Consequently, our purpose for the registration task is twofold. Firstly, a gap arising in the reference image shall be feasible. This will enable the brain to deform in a manner which is not affected by the deformation of the skull area. Secondly, the missing part of the skin in the reference image shall not affect the deformation field. Since there exists no mapping for this part between the template and the reference image, the preferable choice is to leave this part undeformed.

The registration is performed using the standard elastic regulariser with no

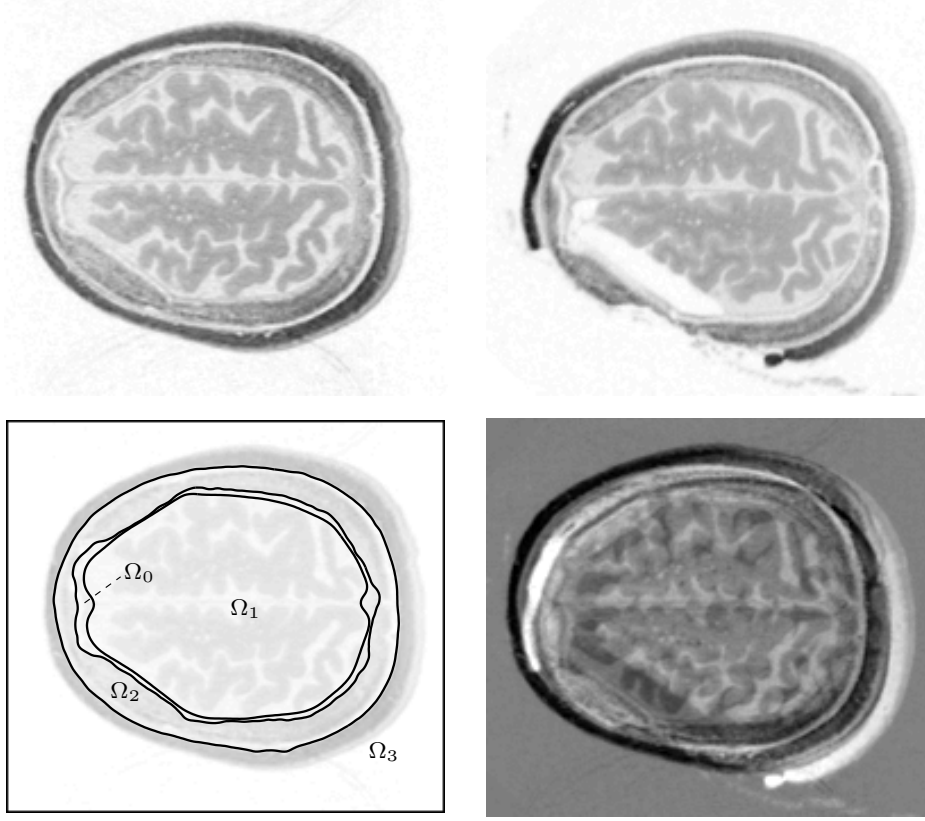


Figure 6.15: Template  $T$  (top left) and reference image  $R$  (top right) together with the subtraction image  $R - T$  (bottom right) and the segmented template (bottom left).

spatially varying parameters and with the variable elastic regulariser based on a segmentation of the template. As before, a multi-resolution pyramid with four levels and a coarsest resolution of  $32 \times 32$  voxels performs well in terms of robustness and computational effort. The number of iterations was 70, 70, 30, 5 from the coarsest to the finest level.

For the standard elastic regulariser, a constant setting of the parameters is chosen. Here, a setting with  $\alpha \equiv 10^{-3}$ ,  $\lambda \equiv 0$ ,  $\mu \equiv 4$  is used to allow for a shrinkage of the brain and the cerebrospinal fluid (CSF) regions. However, a small choice of  $\alpha$  yields a local deformation only and is not applicable for a global alignment as it is required here (see the subtraction image in Figure 6.15, bottom right). Therefore, in a pre-processing step a rigid alignment of the template image in accordance to the reference image or, as done here, a pre-registration (for instance with a regularisation parameter of  $\alpha \equiv 0.1$  and 20 iterations on the coarsest level) is required.

For the variable elastic regulariser, an active contour-based segmentation of the template image (cf. Figure 6.15, bottom left) is given by a decomposition into brain ( $\Omega^1$ ), skull ( $\Omega^2$ ), and skin area (cf. Section 4.2.2). Since the image region outside the skin is not of interest, the determination of an outer contour of the skin is omitted and both the skin and the outer region are collected in the set  $\Omega^3$ . In addition, the region between skull and brain is included in the

Table 6.1: Parameter setting for the registration with a variable elastic regulariser.

	$\Omega^0$	$\Omega^1$	$\Omega^2$	$\Omega^3$
$\alpha$	$10^{-5}$	$10^{-3}$	$10^{-3}$	$10^{-3}$
$\lambda$	0	0	0	0
$\mu$	4	4	400	$4 \cdot 10^4$

set  $\Omega^0$ . Various parameter settings are assigned to each region (summarised in Table 6.1) to facilitate the displacements enforced by the reference image. Firstly,  $\alpha$  is chosen small to allow the CSF regions in the right hemisphere to shrink during transition from the template to the reference image (cf. Table 6.1). For the gap region, the regularisation is further reduced by a factor of 100. Then, for the Lamé parameters, a setting corresponding to a highly compressible material is chosen. In addition,  $\mu$  has been increased in the skull area to model a higher Young's modulus (corresponding to a smaller relative stretch). Finally,  $\mu$  has been largely increased in the skin area to prevent it from a non-rigid deformation (caused by the missing part in the reference image). A pre-processing as for the standard case is not required since the increased value of  $\mu$  in  $\Omega^3$  leads in conjunction with the multi-resolution approach to a correct global translation.

The results are shown in Figure 6.16. The left column displays the result from the first experiment, i.e. using the elastic regulariser, whereas the right column corresponds to the second experiment, i.e. using the variable elastic regulariser. Comparing the deformed images and the subtraction images (first and second row, respectively) an improved registration result is clearly visible.

Although for the first experiment a partial shrinkage of the brain according to the brain shift can be observed, the shape of skull and skin is not preserved. Consequently, a gap in the skull-brain area is not opened to the expected extent and the brain is misaligned near the skull. Moreover, in the region where the skin is missing in the reference image, the skin is mapped onto the skull.

In contrast, for the second experiment the deformed template image indicates a shrinkage of the brain. Due to the shape preservation of the skull a gap between skull and brain is opened. However, in the subtraction image this gap is still visible since it is filled with a grey-value from the template image which is different from one of the gap in the reference image. Moreover, we observe the center line of the brain to be correctly displaced towards the left hemisphere. Finally, the deformation field is not affected by the grey-value difference in the region of the missing skin part. Instead, the skin is rigidly deformed and not mapped onto the skull.

The mapping of the skin area is also visible from the displacement fields (overlaid in the third row, for better visualization every fifth vector is plotted only). While in the first experiment the displacement of the skin causes a similar displacement of the outer brain regions, the brain is not affected in the second experiment.

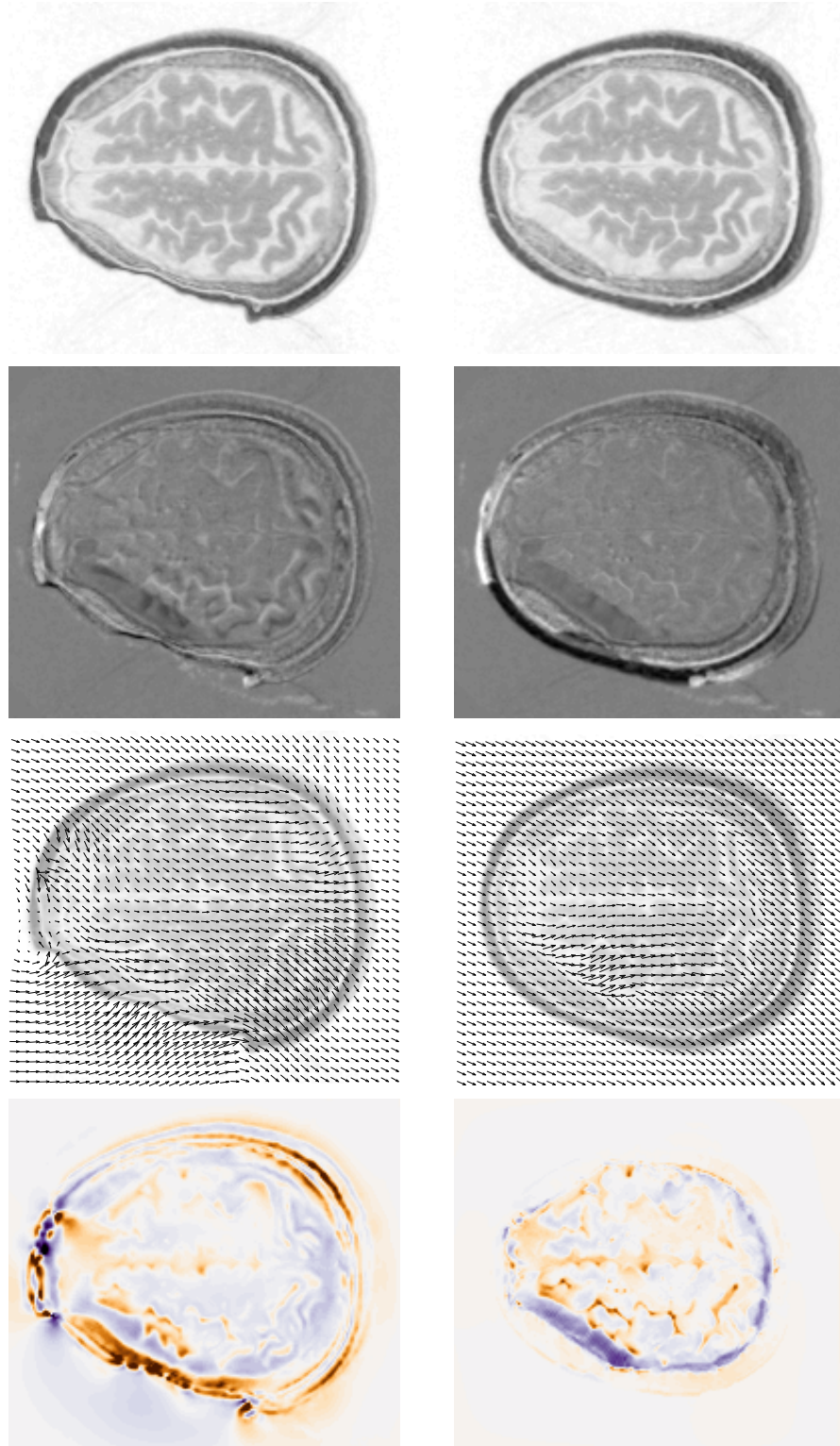


Figure 6.16: Registration results for the standard approach (left) and the proposed approach (right). From top to bottom each column shows the deformed template  $T_U$ , the subtraction image  $R - T_U$ , the deformation field, and a volume preservation map.

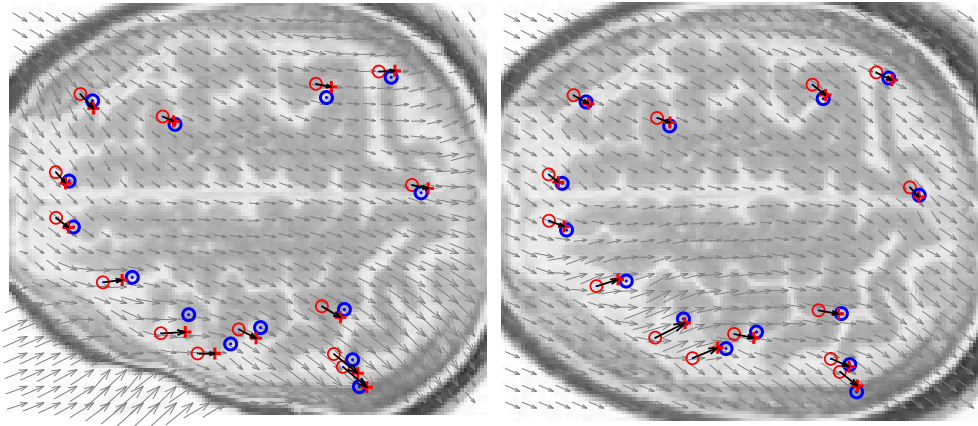


Figure 6.17: Brain-skull area after deformation with the standard method (left) and the proposed method (right). The markers from the template, the reference, and the deformed template image are denoted by red circles, blue circles, and red crosses, respectively.

Moreover, both experiments show an upward movement in the right hemisphere which is damped in the medial regions.

More detailed information is provided by the volume preservation map (bottom row). Here, a blue color indicates an expanded region whereas a red color corresponds to a shrinkage. The major volume changes can be seen for the first experiment. In particular, the skull-skin area is largely deformed with less changes in the brain area. In contrast, the volume of the skull-skin area for the second experiment is nearly preserved. Compared to the first experiment we observe larger changes for the sulci regions, which demonstrates the shrinkage of the brain.

For a more quantitative analysis we manually place markers in the brain-skull area. Note that these markers are for validation purpose only and not used during registration. The markers from the template image are depicted by red circles, the ones from the reference image by blue circles. A red cross denotes the deformed position from the template image.<sup>4</sup> Consequently, a satisfactory registration result is achieved when a red cross aligns with a blue circle, see Figure 6.17.

For fourteen markers the standard and the proposed method yield a median difference of 2.9 mm and 1.3 mm, respectively, compared to the markers in the reference image. The markers with the largest error are those near to the gap region (second to fourth marker when numbering counterclockwise and starting at the front end of the center line of the brain). Here, the median difference is even higher: 4.6 mm for the standard method compared to 2.0 mm for the proposed method.

---

<sup>4</sup>Since a backward approach is used, the resulting deformation field maps the domain of the reference image onto the domain of the template image. For the markers in the deformed template image, the inverse of the resulting displacement field has been approximated using a fixed-point iteration scheme.





---

## 7 Conclusions and Future Work

---

This thesis started by an investigation of a non-parametric registration approach described in the literature. Here, elastic properties can be modelled and are – like the amount of regularisation – uniformly chosen in the entire image domain. Although achieving satisfactory results for a large range of applications, this standard approach shows two major disadvantages when applied to medical images: Firstly, image regions corresponding to different anatomical structures such as bones or soft tissue are treated in the same way. Since the registration scheme has no knowledge of different structures, the resulting transformation does not necessarily reflect the individual elastic properties. Examples include non-realistic deformations of bone areas or unwanted enlargement or shrinkage of tumor regions in follow-up studies. Secondly, an individual treatment of structures may require a reduced amount of regularisation between them, i.e., in a so-called gap region. In particular applications from neurosurgery (e.g. brain shift), orthopaedics or thorax modelling where anatomical structures may move relative to each other (like in joints or like the liver alongside the ribs), exhibit large changes in the gap size and require a spatially varying regularisation.

In this work, a scheme for image registration has been derived which allows for spatial variation of both the amount of regularisation and the elastic properties. The key observation is to replace the related scalars by parameter functions such that dedicated values can be assigned to each region of an image. Numerical schemes are developed to maintain the increased complexity of the registration task.

The proposed scheme starts by computing a segmentation of the template image (unless already given by an atlas). Having obtained a segmentation, a priori knowledge can be used to initialise the parameter functions, that is, to distribute elastic properties to each region and to possibly reduce the regularisation between certain structures. Finally, the registration approach is employed with either the variable diffusive or the variable elastic regulariser.

From several synthetic and medical examples we observed displacement fields being closer to ‘elastic reality’ compared to the standard approach.

However, the proposed scheme may suffer from the parameter functions required to be continuously differentiable. In particular, a gap is allowed to enlarge or

shrink in its size but neither to totally close nor open. As a logical extension, a second approach is considered. Here, the solution space is enlarged and allows for discontinuities in the parameter functions and in the resulting displacement field. Together with the introduction of a virtual gap, both a piecewise variable diffusive and a piecewise variable elastic regulariser are able to cope with a vanishing or emerging structure, i.e., with the occurrence of a topological change. The drawback of this extended scheme lies in the additional requirements: Not only a segmentation of the template is required but also a segmentation of the reference image is needed in such a way that each segmented region of one image corresponds intrinsically to a segmented region of the other image.

This work can be extended in several directions. For future work we suggest to start with a thorough evaluation of the parameter functions – on one hand of the regularisation function  $\alpha$  and on the other hand of the Lamé functions  $\lambda$  and  $\mu$ . This includes a coupling of diffusive and elastic regulariser by choosing the latter in the entire domain and setting  $\lambda = -\mu$  in the regions to be modelled by a diffusive regulariser.

In our believe, the evaluation will result in various parameter settings dependent on the chosen application. Metaphorically speaking, when taking a picture with a reflex camera spontaneously, one will not choose aperture, exposure time, and depth of focus individually but a theme like, e.g., landscape, portrait, night or sport. In the context of image registration, a theme like ‘vessel detection’, ‘breathing compensation’ or ‘brain shift’ will specify a range of parameter settings included in a model. In a brain shift application, for instance, a better adaption of the Lamé functions based on further segmentation into white matter and grey matter regions (which can be achieved by a simple thresholding routine) is likely to result in a more realistic deformation of gyri and sulci regions.

From a mathematical point of view, the derivation of fast numerical schemes as are available for the standard approach is of major importance and, moreover, is essential for clinical use.

In the case of piecewise variable regularisers, a challenging task is to circumvent the additional segmentation of the reference image. In addition, the resulting transformation should be guaranteed to be physically meaningful, i.e. without swapping any regions or resulting in an overlap of non-background regions.

Furthermore, symmetry with respect to the choice of the image to be segmented is a desirable property and, finally, a ‘segistration’ as a combined segmentation and registration promises results being more robust to image artefacts, varying contrast, or segmentation failures compared to a sequential scheme.

---

## Notation

---

$\mathcal{C}^p$	set of $p$ -times continuously differentiable functions
$\mathcal{PC}^p$	set of $p$ -times piecewise continuously differentiable functions
$\mathcal{PC}^{const}$	set of piecewise constant functions
$(\cdot, \cdot)$	Euclidian scalar product
$\mathbf{n}$	outward pointing unit normal vector
$d$	dimension
$\text{id}$	identity operator
$\nabla$	gradient operator
$\nabla_u$	gradient operator w.r.t. a mapping $u : \mathbb{R}^d \rightarrow \mathbb{R}^d$
$\nabla_{\nabla u}$	gradient operator w.r.t. the Jacobian of $u$
$\nabla \cdot$	divergence operator
$\Delta$	Laplace operator
$u_{i,j}$	short notation for partial derivative $\partial u_i / \partial x_j$
$\mathbb{S}, S$	block stencil, stencil
$s^{\kappa_1, \kappa_2}$	stencil entries
$\Omega, \Omega_T, \Omega_R$	image (domain)
$\bar{\Omega}, \partial\Omega$	closure and boundary of domain
$\text{Img}(\Omega)$	set of images defined on $\Omega$
$M(\Omega)$	decomposition of $\Omega$ into regions $\Omega^0, \dots, \Omega^m$
$\text{Img}_{\mathcal{PS}}(M(\Omega))$	set of piecewise smooth images defined on $M(\Omega)$
$T, R, T_u$	images
$\varphi, u$	transformation, displacement

$\mathcal{U}, \mathcal{U}_{\mathcal{PC}}$	spaces of admissible functions
$\mathcal{V}, \mathcal{V}_{\mathcal{PC}}$	spaces of test functions
$\mathcal{J}$	joint functional
$\mathcal{D}_{T,R}^{SSD}, \mathcal{D}_{T,R}^{pSSD}$	similarity measures
$\mathcal{S}^{diff}, \mathcal{S}_{\alpha}^{vardiff}, \mathcal{S}_{\alpha}^{pdiff}$	diffusive regularisers
$\mathcal{S}_{\lambda,\mu}^{elas}, \mathcal{S}_{\alpha,\lambda,\mu}^{varelas}, \mathcal{S}_{\alpha,\lambda,\mu}^{pelas}$	elastic regularisers
$\alpha, \alpha_u$	(transformed) regularisation parameter
$\lambda, \mu, \lambda_u, \mu_u$	(transformed) Lamé parameters
$L, B$	regularising operator, boundary operator
$f, g$	force terms
$\partial_{12}^{\pm}, \partial_1^+, \partial_2^-$	difference quotients
$\partial_1^a$	averaging quotient
$h = (h_1, h_2), k$	spatial and temporal grid spacing
$i, j, l$	spatial and temporal indices
$x_{i,j}, t_l$	discrete points in space and time
$\Omega_h, \Omega_h^{\text{edge}}, \Omega_h^{\text{mid}}$	discretisations of $\Omega$
$\partial\Omega_h, \partial\Omega_h^{\text{edge}}, \partial\Omega_h^{\text{mid}}$	discretisations of $\partial\Omega$
$U$	discrete transformation, $U^{i,j,l} = (U_1^{i,j,l}, U_2^{i,j,l})^{\top}$
$R_h, T_h, T_U$	digital images
$R^{i,j}, T^{i,j}$	discrete image values
$L_h, B_h$	discretised operators
$f_h, g_h$	discretised force terms
$\xi$	grid point mapping
$\mathbf{A}$	matrix
$\mathbf{U}, \mathbf{F}$	rearrangement of $U$ and $f_h U$ in vector form

---

## Bibliography

---

- G. AUBERT & P. KORNPORST, 2002. *Mathematical problems in image processing: partial differential equations and the calculus of variations*. Springer.
- O. AXELSSON & V.A. BARKER, 1984. *Finite element solution of boundary value problems*. Academic Press.
- R. BAJCSY & S. KOVAČIČ, 1989. Multiresolution elastic matching. In *Computer vision, graphics and image processing*, vol. 46, 1–21.
- C. BROIT, 1981. *Optimal registration of deformed images*. PhD thesis, University of Pennsylvania.
- L.G. BROWN, 1992. A survey of image registration techniques. *ACM Computing Surveys*, **24**(4), 325–376.
- D. BYSTROV, V. PEKAR, K. MEETZ, H. SCHULZ & T. NETSCH, 2005. Motion compensation and plane tracking for kinematic MR-Imaging. In *Proc. of CVBIA*, 551–560.
- G.E. CHRISTENSEN, R.D. RABBITT & M.I. MILLER, 1996. Deformable templates using large deformation kinematics. *IEEE Trans Image Proc*, **5**, 1435–1447.
- U. CLARENZ, M. DROSKE, S. HENN, M. RUMPF & K. WITSCH, 2006. Computational methods for nonlinear image registration. to appear.
- U. CLARENZ, M. DROSKE & M. RUMPF, 2002. Towards fast non-rigid registration. In M.Z. Nashed & O. Scherzer (eds.), *Inverse Problems, Image Analysis, and Medical Imaging*, vol. 313 of *Contemporary Mathematics*, 67–84. AMS.
- A. COLLIGNON, F. MAES, D. VANDERMEULEN, P. SUETENS & G. MARCHAL, 1995. Automated multimodality image registration using information theory. In *Proc. of IPMI*, vol. 3, 263–274.

- C. DAVATZIKOS, 1996. Nonlinear registration of brain images using deformable models. In *Proc. of the IEEE Workshop on Math. Methods in Biomedical Image Analysis*, 94–103.
- V. DUAY, P.F. D’HAESE, R. LI & B.M. DAWANT, 2004. Non-rigid registration algorithm with spatially varying stiffness properties. In *Proc. of the IEEE International Symposium on Biomedical Imaging*, 408–411.
- O. ECABERT, T. BUTZ, A. NABAVI & J.P. THIRAN, 2003. Brain shift correction based on a boundary element biomechanical model with different material properties. In R.E. Ellis & T.M. Peters (eds.), *Proc. of MICCAI*, LNCS 2878, 41–49.
- P.J. EDWARDS, D.L.G. HILL, J.A. LITTLE & D.J. HAWKES, 1998. A three-component deformation model for image-guided surgery. *Med Image Anal*, **2**(4), 355–367.
- J. EHRHARDT, H. HANDELS, B. STRATHMANN, T. MALINA, W. PLÖTZ & S.J. PÖPPL, 2003. Atlas-based recognition of anatomical structures and landmarks to support the virtual three-dimensional planning of hip operations. In R.E. Ellis & T.M. Peters (eds.), *Proc. of MICCAI*, LNCS 2878, 17–24.
- L.C. EVANS, 1998. *Partial differential equations*. AMS.
- M. FERRANT, A. NABAVI, B. MACQ, F.A. JOLESZ, R. KIKINIS & S.K. WARFIELD, 2001. Registration of 3D intraoperative MR images of the brain using a finite element biomechanical model. *IEEE Trans Med Imaging*, **20**(12), 1384–1397.
- B. FISCHER & J. MODERSITZKI, 1999. Fast inversion of matrices arising in image processing. *Numerical Algorithms*, **22**, 1–11.
- B. FISCHER & J. MODERSITZKI, 2002. Fast diffusion registration. In M.Z. Nashed & O. Scherzer (eds.), *Inverse Problems, Image Analysis, and Medical Imaging*, vol. 313 of *Contemporary Mathematics*, 117–129. AMS.
- B. FISCHER & J. MODERSITZKI, 2004. A unified approach to fast image registration and a new curvature based registration technique. *Linear Algebra and its Applications*, **380**, 107–124.
- O. FORSTER, 1999. *Analysis 2*. Vieweg.
- K.A. GANSER, H. DICKHAUS, A. STAUBERT, M.M. BON SANTO, C.R. WIRTZ, V.M. TRONNIER & S. KUNZE, 1998. Quantifizierung von Brain-Shift durch Vergleich von prä- und intraoperativ erzeugten MR-Volumendaten. In T. Lehmann, V. Metzler, K. Spitzer & T. Tolxdorff (eds.), *Proceedings of the Workshop Bildverarbeitung für die Medizin 1998 (BVM’98)*.
- G.H. GOLUB & C.F. VAN LOAN, 1996. *Matrix computations*. Johns Hopkins University Press, Baltimore, Maryland, 3rd edn.

- E. HABER & J. MODERSITZKI, 2005. Beyond mutual information: a simple and robust alternative. In H.P. Meinzer, H. Handels, A. Horsch & T. Tolxdorff (eds.), *Proc. of BVM*, 350–354.
- A. HAGEMANN, 2001. *A biomechanical model of the human head with variable material properties for intraoperative image correction*. PhD thesis, Fachbereich Informatik, Universität Hamburg.
- T. HARTKENS, D.L.G. HILL, A.D. CASTELLANO-SMITH, D.J. HAWKES, C.R. MAURER, JR., A.J. MARTIN, W.A. HALL, H. LIU & C.L. TRUWIT, 2003. Measurement and analysis of brain deformation during neurosurgery. *IEEE Trans Med Imaging*, **22**(1), 82–92.
- M.R. KAUS, T. NETSCH, S. KABUS, V. PEKAR, T. MCNUTT & B. FISCHER, 2004. Estimation of organ motion from 4D CT for 4D radiation therapy planning of lung cancer. In C. Barillot, H.D. R. & P. Hellier (eds.), *Proc. of MICCAI*, vol. 3217 of *Lecture Notes in Computer Science*, 1017–1024.
- P. KEALL, 2004. 4-dimensional computed tomography imaging and treatment planning. *Seminars in Radiation Oncology*, **14**(1), 81–90.
- K. KÖNIGSBERGER, 2004. *Analysis 2*. Springer.
- S. LARSSON & V. THOMÉE, 2003. *Partial differential equations with numerical methods*. Springer.
- H. LESTER, S.R. ARRIDGE, K.M. JANSONS, L. LEMIEUX, J.V. HAJNAL & A. OATRIDGE, 1999. Non-linear registration with the variable viscosity fluid algorithm. In A. Kuba & M. Sama (eds.), *Proc. of IPMT'99*, 238–251.
- R.J. LEVEQUE, 1992. *Numerical methods for conservation laws*. Birkhäuser.
- J.B.A. MAINTZ & M.A. VIERGEVER, 1998. A survey of medical image registration. *Med Image Anal*, **2**(1), 1–36.
- L.E. MALVERN, 1969. *Introduction to the mechanics of a continuous medium*. Prentice-Hall.
- C.R. MAURER, JR. & J.M. FITZPATRICK, 1993. *Interactive image-guided neurosurgery*, A review on medical image registration (R.J. Maciunas, ed.), 17–44. American Association of Neurological Surgeons.
- J. MODERSITZKI, 2004. *Numerical methods for image registration*. Oxford University Press.
- H.J. OBERLE, 1998. Variationsrechnung und Optimale Steuerung. Lecture Notes, Universität Hamburg, Fachbereich Mathematik.
- W. PECKAR, 1998. *Application of variational methods to elastic registration of medical images*. PhD thesis, Fachbereich Informatik, Universität Hamburg.

- V. PEKAR, T.R. McNUTT & M.R. KAUS, 2004. Automated model-based organ delineation for radiotherapy planning in prostatic region. *Int. J. Radiation Oncology Biol. Phys.*, **60**(3), 973–980.
- J.P.W. PLUIM & J.M. FITZPATRICK, 2003. Image registration. *IEEE Trans Med Imaging*, **22**(11), 1341–1343.
- J. REXILIUS, H. HANDELS, A. NABAVI, R. KIKINIS & S.K. WARFIELD, 2002. Automatic nonrigid registration for tracking brain shift during neurosurgery. In *Proc. of BVM 2002*, 135–138.
- G.K. ROHDE, A. ALDROUBI & B.M. DAWANT, 2003. The adaptive bases algorithm for intensity-based nonrigid image registration. *IEEE Trans Med Imaging*, **22**(11), 1470–1479.
- O. ŠKRINJAR, A. NABAVI & J. DUNCAN, 2002. Model-driven brain shift compensation. *Med Image Anal*, **6**, 361–373.
- M. STARING, S. KLEIN & J. PLUIM, 2005. Nonrigid registration with adaptive, content-based filtering of the deformation field. In *Proc. of SPIE*, vol. 5747, 212 – 221.
- D. TERZOPOULOS, 2003. *Geometric level set methods in imaging, vision, and graphics*, Deformable models: classic, topology-adaptive and generalized formulations (S. Osher and N. Paragios, eds.), 21–40. Springer.
- J.W. THOMAS, 1995. *Numerical partial differential equations. finite difference methods*. Springer.
- U. TROTTEBERG, C.W. OOSTERLEE & A. SCHÜLLER, 2001. *Multigrid*. Academic Press.
- P.M. VIOLA & W.M. WELLS, 1995. Aligment by maximization of mutual information. In *Proc. of ICCV*, 16–23.
- Y. WANG & L.H. STAIB, 2000. Physical model-based non-rigid registration incorporating statistical shape information. *Med Image Anal*, **4**, 7–20.
- J. WEESE, P. RÖSCH, T. NETSCH, T. BLAFFERT & M. QUIST, 1999. Gray-value based registration of CT and MR images by maximization of local correlation. In *Proc. of MICCAI*, 656–663.
- C. XU, 1999. *Deformable models with application to human cerebral cortex reconstruction from magnetic resonance images*. PhD thesis, Johns Hopkins University, Baltimore.
- C. XU & J.L. PRINCE, 1998. Snakes, shapes, and gradient vector flow. *IEEE Trans Image Proc*, **7**(3), 359–369.



---

# Index

---

- active contours, 68
- assembling, 29
- averaging quotient, 23
  
- background, 67
- backward Lagrangian, 11, 47
- boundary conditions
  - Dirichlet, 17
  - discretised, 24, 25
  - essential, 41
  - natural, 41
  - Neumann, 17
- boundary value problem, 17
  - initial, 18, 46, 74
  - variational formulation, 36, 40
- brain shift, 116
  
- common boundary, 67
- consistency, 22
  
- decomposition, 67
- deformation, 11
- difference quotient, 22
- discretisation
  - edge-point, 20, 24
  - mid-point, 20, 24
- displacement, 11
  - affine linear, 13
  - B-spline, 14
  - non-parametric, 15
  - polynomial, 14
  - rigid, 13
- distance measure, 11
- domain, 9
  
- elastic phantom, 110
- Euler-Lagrange equation, 40, 93
  - diffusive regulariser, 44
  - elastic regulariser, 45
  - joint formulation, 46, 74, 97
  - piecewise diffusive regulariser, 96
  - piecewise elastic regulariser, 97
  - piecewise SSD measure, 96
  - SSD measure, 43
  - variable diffusive regulariser, 70
  - variable elastic regulariser, 72
  
- finite difference method, 19
- first variation, 35
- fixed-point iteration, 17, 54
- forward Lagrangian, 11, 47
  
- Gâteaux derivative, 37
- grid point mapping, 30
  
- image, 10
  - digital, 10
  - piecewise smooth, 92
  
- kinematic motion, 112
  
- Lamé parameters, 44, 56
- LOA, 22
  
- minimisation problem, 35, 92
- minmod slope, 84
- multi-resolution, 52, 84
  
- natural interface condition, 90, 93
- Navier-Lamé equations, 45

- piecewise constant, 92
- piecewise differentiable, 92
- Poisson's ratio, 45
- radiotherapy planning, 114
- reference image, 11
- registration problem, 11, 16
- regularisation, 43
  - variable, 69
- regularisation parameter, 16, 53
- regulariser
  - diffusive, 44
  - elastic, 44
  - piecewise diffusive, 96
  - piecewise elastic, 96
  - variable diffusive, 70
  - variable elastic, 72
- segmentation, 67, 68
- similarity measure, 11, 42
  - piecewise SSD, 95
  - SSD, 42
- stencil, 27
  - boundary, 29
  - symmetric, 28, 32
  - transposed, 28
- stopping criteria, 51
- template image, 11
- time-marching, 18, 54
- topological change, 91
- transformation, 11
- variable stencil, 75
  - symmetric, 76, 81
  - transposed, 76
- virtual gap, 100
- weighting function, 64
- Young's modulus, 45

---

# Erklärung

---

Ich versichere, daß ich die Dissertation ohne fremde Hilfe angefertigt und keine anderen als die angegebenen Hilfsmittel verwendet habe.

Lübeck, den 4. Oktober 2006



---

# Lebenslauf

---

## Persönliche Daten

Vor- und Zuname	Sven Kabus
Geburtsdatum	29.Mai 1978
Geburtsort	Schleswig
Familienstand	ledig
Staatsangehörigkeit	deutsch

## Ausbildung

05.1997	Abitur am Fördegymnasium Flensburg
08.1997 – 08.1998	Zivildienst in der Kindergarten Adelby GmbH, Flensburg
10.1998 – 09.2000	Grundstudium der <i>Technomathematik</i> an der Christian-Albrechts-Universität zu Kiel mit Nebenfächern Informatik und Elektrotechnik
09.2000 – 09.2001	Masterstudium in <i>Computational Mathematics with Modelling</i> an der Brunel University, London, mit Abschluss „Master of Science“
10.2001 – 06.2003	Hauptstudium der <i>Technomathematik</i> an der Christian-Albrechts-Universität zu Kiel mit Abschluss „Diplom-Mathematiker“

## Weiterer Werdegang

07.2003 – 06.2006	Wissenschaftlicher Angestellter am Institut für Mathematik der Universität zu Lübeck
seit 07.2006	Wissenschaftlicher Mitarbeiter bei den Philips Technologie GmbH Forschungslaboratorien, Hamburg